Smart Monitoring & Early Warning System of Sinkhole with Fibre Optic Sensors and InSAR

Report to the
Water Research Commission

by

M Ferentinou[1], M Grobler[1], A Malinowska[2], P Farina[3] and J Yumba[1]

[1] University of Johannesburg
[2] AGH University of Science and Technology, Poland
[3]GeoApp

WRC Report No. 2937/1/22
ISBN 978-0-6392-0517-5

January 2023

WATER
RESEARCH
COMMISSION

Obtainable from
Water Research Commission
Bloukrans Building
4 Daventry Road
Lynnwood Manor
PRETORIA
South Africa

orders@wrc.org.za or download from www.wrc.org.za

Executive Summary

Sinkholes are alarming and dangerous events, they have a worldwide occurrence, and are imposing a potential risk to infrastructure, urban communities and the widely developed built environment. However, although they represent a natural risk that may hit catastrophically without clearly detectible precursors, they are often overlooked by the public and local authorities. Therefore, sinkhole monitoring and associated early warnings constitute an important research topic, with high associated, impact.

In this project we developed a combined two scale approach for the monitoring of sinkhole development. Satellite Synthetic aperture Interferometry earth observation methods, were used to monitor and assess susceptible to sinkhole hazard urban areas in Centurion. The PSInSAR analysis was carried out using ascending and descending SAR images from Sentinel-1 between May 2015 and May2017. The PSInSAR study for the temporal interval preceding sinkhole occurrence on the 17th of May 2017 showed subsiding and stable zones. Most of Centurion region seems to be relatively stable with an average displacement velocity of -1,6 mm/year. In the North of the study area, the mean annual subsidence reached -12 mm/year.

This study also included experimental work aimed at investigating the feasibility of fibre Bragg sensors as an early warning system for sinkhole detection. To this end, small-scale plane strain, instrumented 1-g models were built to provide further insight into the formation of a sinkhole. For the models Cullinan silica sand and WAD material were used, and an embedded leaking pipe. In these models, the sinkhole was simulated by an inflated balloon. The experiments included tests with a higher flow rate of leaking water within the sinkhole models, one with silica sand and the other with layers of wad material mixed with silica sand with a lower leaking flow rate, in silica sand wad material. FBGs were positioned horizontally and vertically in the models.

According to the findings of this study, the fibre Bragg grating sensors are sensitive to ground movement and can identify strain signatures indicating a change in strain before visual identification of collapse. FBG sensors were proved to be highly useful in determining the strain distribution in different soil profiles for monitoring the collapse process a failure mechanism. This could serve as an early warning signal for sinkhole disasters since the optical fibre sensing can provide a viable option for developing an early warning system. Efficient integration of an IoT-enabled FBG smart sensing system could detect precursor movement of soil mass due to leaking pipes and support risk management.

This page was intentionally left blank

TABLE OF CONTENTS

LIST OF FIGURES

LIST OF TABLES

CHAPTER 1: EARLY DETECTION OF SINKHOLE AND SUBSIDENCE OCCURRENCE, CAN IT BE ACHIEVED? A COMPREHENSIVE REVIEW OF RECENT APPLIED PHOTOGRAMMETRIC TECHNOLOGIES

1.1 Introduction

Sinkholes and subsidence are considered a dangerous natural or man-made hazard, resulting often in fatalities, property loss, affecting transportation and other infrastructure networks, in regions underlain by soluble bedrock. During the last decades an increase in sinkhole related damage is reported in a global scale, which is either attributed to human activities that initiate mobilizing agents, or to the development on sinkhole prone terrain.

Consequently, when these worldwide events, are associated with urban environments they pose at risk affected communities and infrastructure (Zhou et al., 2008; Gutiérrez et al., 2008, 2018; Galvo et al., 2009; Parise et al., 2015). Some recent examples in the literature come from Italy (Del Prete et al., 2010; Parise and Lollino, 2011; Intrieri et al., 2015), USA, Florida (Brinkmann et al., 2007), Turkey (Dogan and Yilmaz (2011), China (Gao et al., 2013); USA, Virginia, Vacarri et al. (2013), Saudi Arabia (Youssef et al., 2016), Dead Sea (Baer et al., 2018), South Africa (Theron et al., 2017; Constantinou and van Rooy, 2018; Dippenaar et al., 2019).

Often, these events, appear instantaneously with little or no warning and may hit catastrophically without clearly detectible precursors. A significant cost is associated primarily with the remediation, mitigation, and closure of the exposed cavity, and secondary with the repair of the affected major (i.e. urban networks), or (damage to property, etc.). Damage from sinkholes can be distinguished to direct and indirect losses. Direct losses are related with fatalities and damage to property and infrastructure (i.e. fracture of service lines and damage to roads and pipelines, differential settlement in buildings support foundations). Whereas indirect losses, are more extensive and may affect entire communities or businesses even at the periphery of the immediate region. Indirect or hidden losses might be disruption to business, transportation and communication networks, the costs related to assistance, temporary storage and accommodation for those dislocated by the occurrence of the event), and non-easily tangible losses (harder to quantify in monetary values. These comprise deviations on everyday commuting to work, mental disorders, and eventually the cost of moving population from an area at risk) (Intriery et al., 2015).

In the United States for the period 2000 to 2015 the average cost of sinkhole associated damages is estimated to be at least US $300 million y^{-1} and the actual total is probably much higher, Waery (2015). On another case, in the Spanish cities of Oviedo and Calatayud that are situated on cavernous gypsum, the direct economic losses caused by single collapse events that affected buildings in 1998 and 2003 were estimated to be 18 and 4.8 million euros, respectively (Gutiérrez et al., 2008). In Allentown (Pennsylvania, USA), the direct economic losses were more than US $8 million (Dougherty, P., 2005). A community of approximately 30,000 households was being relocated to safer ground in a dolomite area west of Johannesburg at a cost exceeding US $600 million (Buttrick et al., 2011).

The literature devoted to sinkhole monitoring is very limited, yet recently is attracting growing interest and there is a developing need to understand mechanisms of incipient collapse and monitor rate of ground displacement to assist towards an effective sinkhole risk management. Reliable spatial and temporal sinkhole hazard mapping, supported with monitoring programs in place could efficiently support sinkhole risk management, through the adoption of "sinkhole protocols", zoning of land, design of remedial measures, and assess the performance of adopted design solutions.

Remote sensing earth observation methods have proven to be valuable tools during the last two decades predominantly in long-term sinkhole hazard assessment. Satellite, air-born and ground-based earth observation methods have primarily facilitated the wide detection of continuous displacement on the earth's crust. Monitoring of precursory deformation that acts as a warning prior to sinkhole onset to the surface as subsidence is essential for local authorities, to set alarms, and prioritize evacuation areas. If early reliable detection of sinkhole occurrence is widely implemented, local authorities will be able to support communities proactively, and save towards very high remediation costs.

In the current paper, a comprehensive review of the recent literature on sinkhole and subsidence detection and deformation measurement, is presented to explore feasibility of early detection of sinkhole and ground subsidence based on photogrammetric methods. The current review on sinkhole monitoring is based on a total 30 scientific papers published in peer reviewed international journals from 2013 to 2020 which were identified by a systematic search of Scopus using a set of keywords and criteria. These studies report on recently developed remote sensing techniques and applications into monitoring of sinkhole induced deformation. The review builds upon previous work by Theron and Engelbrecht (2018) and Gutiérrez et al. (2019). Theron and Engelbrecht (2018), in a review paper on the role of observation with focus on SAR Interferometry, provide a review of earth observation techniques, discuss the advantages and disadvantages, of the methods, and conclude that by highlighting the potential role of radar interferometry on early detection. Gutiérrez et al., 2019 present review of sinkhole monitoring methods and discusses some practical considerations about their capabilities and limitations.

The manuscript is organized as follows. In section 2 background information on sinkhole mechanism formation is presented. In section 3, the focus is on the description and analysis of the literature database is. In section 4 a critical discussion is developed on the advantages and limitations of the existing remote sensing photogrammetric methods applied in sinkhole and subsidence detection. In section 5 the challenges of related sinkhole identification are presented followed by a proposal of the application of complementary methods to enhance monitoring and progress to real time monitoring. Finally, section 6 is the conclusion and summary of the lessons learnt and provides general recommendations.

1.2 Background

1.2.1 Definitions and general concepts

The term sinkhole derives from the process of its evolution, many times it is also synonymously used to the term doline *dolina* (meaning negative landform) (Waltham et al., 2005). There are two settlement problems in the dolomitic subsoils: (i) a gradual subsidence, defined as a caving subsidence, which gives rise to enclosed depressions in the ground surface; and (b) a catastrophic subsidence, defined as a sinkhole, which occurs suddenly, the hole having very steep sides and being of limited lateral extent (Jennings et al., 1965; Fairbridge, 1968; Waltman et al., 2005). It is of notice that since 1965 Jennings and co-authors refer to attempts to develop warning devices and develop forms of surface measurement which will unveil the potential conditions before ground collapse actually takes place.

The process of sinkhole formation is continuous dissolution of sub terrain soluble rocks, progressively leading to the development of cavities. When the soil above these cavities reach critical conditions (soil material exceeds shear strength), soil collapses, as a result of reduction of soil vertical stress. Main causes of underground cavities are the ingress of water, the lowering of groundwater table, or extensive pumping leading to dewatering (Intrieri et al., 2015; Dippenaar et al., 2019).

In most sinkhole sites, gradual land subsidence continues for weeks to years after the collapse event. Thus, quantitative evaluation of the subsidence rates and their spatial and temporal extents provide important information about the subsurface sinkhole-forming processes and enable assessing the degree of activity in specific sites and distinguishing between active and inactive areas (Anvi et al., 2016).

1.2.2 Mechanism of sinkhole formation

The classification of sinkholes has evolved from various previous classifications is presented by (Waltman et al., 2005) and later by Gutiérrez et al. (2008a, 2014) and illustrated in Fig 1. Sinkholes are classified into six basic types, as a result of the relevant formation process, namely "solution sinkhole, collapse sinkhole, caprock sinkhole, dropout sinkhole, suffusion sinkhole, buried sinkhole".

Sinkholes are classified in the literature into three main types according to the processes involved in their formation (Gutiérrez et al., 2008a, 2014): collapse sinkholes which involve brittle gravitational deformation of cover and bedrock material, suffusion sinkholes in which cover deposits migrate downward through dissolution conduits accompanied with ductile settling, and sagging sinkholes where ductile sediments bend downward due to differential lowering of the soluble bedrock. In practice, many sinkholes form by a combination of these three processes.

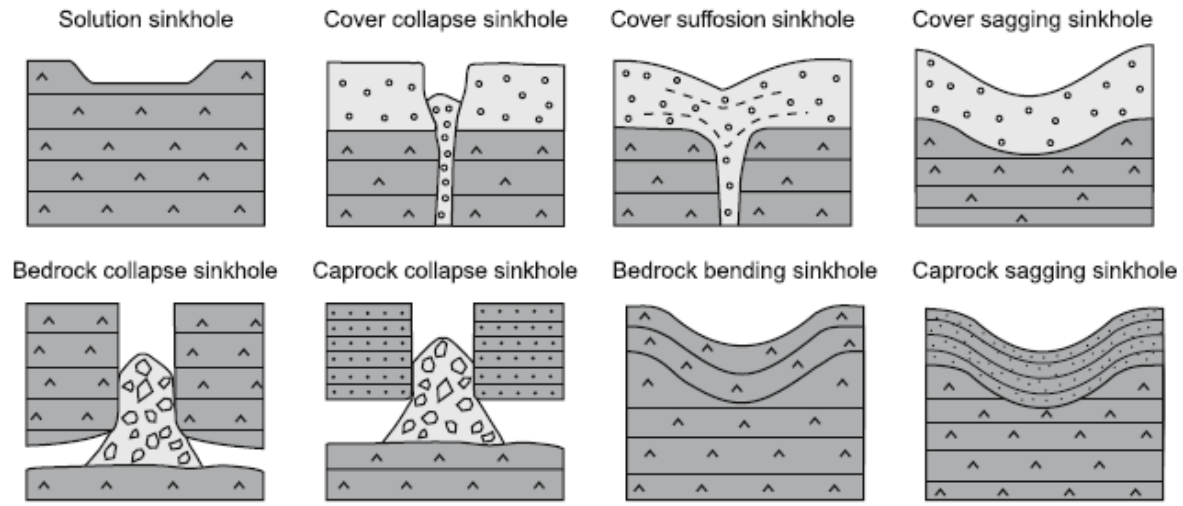

Figure 1-1: Classification of sinkholes, adopted (I need to redo them) Waltman et al., 2004, Gutiérrez et al. (2008a, 2014)

Jennings (1965) based on experience from South African dolomites, states that "a sinkhole occurs by the ground collapse of an arch or dome which spans an air-filled void. The collapse of the roof takes place by an onion-skin peeling of the intrados. The material falls to the floor of the void and in this way the void moves upwards towards the ground surface. The collapse of the final arch or dome manifests itself as a sinkhole". Jennings et al. (1965) distinguish five necessary conditions to be satisfied for a sinkhole to form: (1) The presence of rigid material to host the soil arching cover over the dome. The rigid material will serve as the necessary abutments for the roof of the void. The span should not be too large so the arch can

form; (2) Arching mechanism must develop within the residuum material; (3) A void must develop below the arch in the residuum; (4) A reservoir must exist below the arch to receive the soil which is removed from the vault, and a transportation agent to transport the soil; and (5) When a void of adequate size is formed in the residuum, some disturbing agency must be activated to cause the roof to collapse. The cavity will move progressively upwards towards the surface. Jennings et al. (1965), mention that the triggering factor is usually the infiltration of water which leads into loss of strength of the arching soils.

Predisposing factors

Intrieri et al. (2015) rank among sinkhole predisposing factors, as the most dominant factor the presence of soluble rocks subject to karstic processes (lithology), followed by the preexistence man made underground cavities, of low geomechanical properties of the bedrock, and (acidic) groundwater circulation promoting the dissolution of evaporate and carbonate rocks.

Triggering

The triggering is attributed to the ingress of water into the ground which in return contributes to increase the load of the soil material deposited in the vadose zone. This as a result may reduce the geomechanical strength of the soils and promote internal erosion and dissolution processes, Gutiérrez et al. (2009).

Methods

The methods and technologies usually adopted in sinkhole deformation monitoring have been extensively tested and applied in other fields of geohazard monitoring such as landslides (Intrieri et al., 2015). However, in the case of cavity propagation, there are serious inherent difficulties, as opposed to landslide hazard. One of them is the sudden manifestation of the phenomenon itself without any previous warning (Gutiérrez, F. et al. (2008b), especially in the type of sinkhole caprock collapse. Intrieri et al. (2015) indicate that measurable plastic deformation may occur days before the failure; in the order of a few millimetres to a few centimetres. Baer et al. (2018), and Jacobsz (2016), Labuschagne et al. (2019), Ferentinou (2020), based on observations, and results from numerical simulations, and physical model experiments indicate that while surface subsidence accelerates during the precursory period, the width of the subsiding area remains intact, which is probably indicating that upward propagation and breakthrough of the cavity is not necessarily occurring during the precursory period.

Gutiérrez et al., 2019, refer to (e.g. Kemmerly, 1982; Magdalene and Alexander Jr., 1995) who concur that sinkholes are the best predictors of future subsidence events. They suggest that a (mother doline) creates favourable conditions for the generation of new sinkholes (daughter dolines) in its vicinity. As a result, sinkholes tend to cluster and obviously this is an important guideline to the creation of reliable sinkhole inventory. Though, other authors suggest that the occurrence of new sinkholes is more likely to be a random process, not necessarily dependent on the distribution of pre-existing sinkholes (McConnell and Horn, 1972; Hyatt et al., 1999). These observations should be taken into consideration when sinkhole inventories are developed through automated or semi-automated reconnaissance methods.

1.3 Design and development of the literature database

To develop the literature database, peer-reviewed articles in the Scopus online platform were identified using key words and Boolean search criteria applied to the title and keywords

of the publications. The keywords used included the terms: “Sinkhole”, “subsidence”, “remote sensing”, “early warning”, “monitoring”, “interferometry”.

We considered articles published between 2013 and 2021, where the citation ranges between three to sixty-two citations. The papers were also examined to identify whether there was relevance for the literature database. It was examined whether the content included remote sensing earth observation methods for sinkhole and subsidence detection. This was done through the title, abstract and the entire document. The selection of the type of information that is presented in the current synthesis was based on the reading of all the 30 articles.

The identified information was read in order to populate data in relation to article information, study area, geological conditions, sinkhole geometry, sinkhole type and sinkhole mechanism and dimensions, mobilizing agent, earth observation method, monitoring methods, complementary data used to interpret the subsidence data.

1.3.1 Earth observation method – Long term monitoring

1.3.1.1 Airborne based methods

LiDAR (Light Detection and Ranging) is a remote sensing technology that uses lasers to measure earth surface elevation with very high density and accuracy (NOAA, 2012). LiDAR technology was applied successfully for sinkhole recognition (Nof et al., 2013; Rahimi and Alexander, 2013; Zhu et al., 2014; Razabi et al., 2018). Nonetheless, Zhu and Pierskalla (2016) mention that, extracting sinkhole depressions from LiDAR data can be challenging because of the numerous of features that can be digitized or extracted. Paylor et al. (2003) in Kentucky, digitised more than 100,000 sinkholes based on 1:24,000 scale topographic maps, while Zhu et al. (2014) extracted three times more sinkholes from LiDAR than those identified from the topographic maps from the study area. The same authors indicate that processing LiDAR to identify sinkholes often derives several depression features that are not sinkholes (false positives), they found that almost 85% of the extracted depression features from LiDAR were not sinkholes.

When Lidar data are combined with InSAR data and ground truth verification it can reveal changes in topography depressions, Atziori et al. (2015).

Jones and Blom (2014), collected and processed data from 2009 to 2012, from Uninhabited Aerial Vehicle Synthetic Aperture Radar (UAVSAR). Hensley et al. (2009), to study the Bayou Corne sinkhole formation, in Louisiana (USA). In this case imaging the area from opposite directions but at the same incidence angle, allowed to separate the horizontal and vertical components of the surface displacement, obtaining a two-dimensional image of displacement in the radar imaging plane. According to the same authors, one of the advantages of UAVSAR is the L band system (23.8 cm wavelength), which is allowing the images maintain radar coherence for a much longer time than would be possible with X band (3.1 cm wavelength) and C band (5.6 cm wavelength) SAR from commercial satellite SARs. They also raise a concern, that precursory surface deformation for the Bayou Corne sinkhole was primarily horizontal displacement with relative absence of vertical deformation. This was an unusual result and differed from previous InSAR observations of sinkhole development as was reported by (Paine et al., 2012; Nof et al., 2013). The measurement of precursory surface deformation reported, was 260 mm, derived with interferometric synthetic aperture radar (InSAR), this was evident over a month before surface collapse. The sinkhole formed in the area with the largest gradient in surface strain but did not cover the full extent of the precursory deformation detected with radar.

1.3.1.2 Satellite synthetic aperture radar interferometry

Synthetic aperture radar (SAR) is a remote sensing technology using a microwave imaging system, which is offering high ground resolution owing to the combination of the echoes of rapid radar pulses emitted by the satellite. Data can be acquired under all weather conditions, less time consuming in relation to traditional on site surveying. Interferometric SAR (InSAR), allows accurate measurements of the radiation travel path because it is coherent. Measurements of travel path variations as a function of the satellite position and time of acquisition allow generation of digital elevation models and measurement of centimetric surface deformations of the terrain. Spaceborne SAR is a side looking system collecting data at a specific angle from nadir, namely incidence angle. InSAR operates by relating the coherent phase difference between radar echoes collected from the same point on the ground at two different observation times to the path-length difference between the aircraft and the ground, enabling highly accurate measurement of surface displacement in the line-of-sight direction (Rosen et al., 2000). Only the cumulative displacement that occurred during the time interval between the imaging is measured, InSAR cannot detect movement perpendicular to the imaging plane.

Interferometric synthetic aperture radar (InSAR) and its derivatives have proved to be the most valuable and widely used method in sinkhole mapping and long-term deformation monitoring (Gutiérrez et al., 2014, Vaccari et al., 2018). However, according to (Vaccari et al., 2018), challenges associated with these big datasets are primarily the development of analysis tools that can synthesize them into products meaningful to the geotechnical community. Secondly, that the continuous integration of both data and products with existing monitoring datasets, within existing monitoring workflows, is not always feasible.

The intensity of the acquired interferogram might vary, due to both topographical profile variations and possible ground deformation within the imaged area. Further methods and algorithms were developed to remove topographic and atmospheric effects from the derived interferogram. The use of Differential InSAR (DInSAR) takes into account the Digital Elevation Model (DEM) of the imaged area to remove the topographic effects. As a result, the deformation along the line-of sight (LOS) of the satellite is quantified. An advanced DInSAR technique named permanent/persistent scattered InSAR (PSInSAR) was introduced by (Ferretti et al., 2011), to resolve atmospheric interference problems.

Several works have focused on the application of such DInSAR techniques to the detection and monitoring of land subsidence induced by groundwater extraction in many regions of the world (Calo et al., 2016, Dehghani et al., 2013).

Since such early applications, relevant algorithmic advances have been achieved and several DInSAR approaches fully exploiting large SAR datasets to generate time-series of deformations have been developed. These techniques can be grouped in two main categories: the Persistent Scatterers (PS) (Ferreti et al., 2011) and the Small Baseline (SB) (Berrandino, 2002; Mora et al., 2003). In particular, the PS techniques focus on point-like targets that are not significantly affected by decorrelation noise (Zebker, 1992), and are suitable to monitor deformations affecting point-wise structures. Conversely, the SB methods rely on selecting SAR data pairs with short temporal (i.e. time interval between two acquisitions) and perpendicular (i.e. the distance between two satellite passes) baselines in order to reduce the noise, and allow the investigation of displacements over distributed scatterers (DS) on the ground.

The PSInSAR technique is capable of measuring displacements with millimetre precision on radar targets within the imaged areas retrieved within SAR images. Persistent scatterers (PS) targets can be artificial surfaces on (buildings, metallic structures, lamp posts, crash barriers, transmission towers, fences, road lines) or natural targets (rock outcrops)

characterized by a stable phase signal (Ferreti et al., 2001; Bianchini et al., 2019). This technique turns out to be particularly suitable in urban/peri-urban areas which include many potential coherent PS. In contrast in rural areas the density of PS can be extremely low.

Vaccari et al. (2018) state that for those locations (permanent/persistent scatterer – PS) that have a large displacement signal-to- measurement noise ratio (SNR) across several SAR images, PSInSAR can deliver deformation measurements with an accuracy of less than 1 cm. Signal to noise ratio contours can indicate significant displacement areas.

The introduction of an improved version of PSInSAR, SqueeSAR(10) usually refer to as the second generation of PSInSAR, with an additional layer of statistical analysis is used to identify non-urban regions providing a consistent and traceable response to the radar pulses over time, providing a high quality result, Ferretti et al. (2011). The SqueeSAR technique is an evolution of PSInSAR. The SqueeSAR technique overcomes some limits of PSInSAR by extracting information not only from point-wise objects (i.e. PS), but also from Distributed Scatterers (DS). The latter ones are homogeneous areas detected over a group of pixels in the SAR image and characterized by moderate coherence. DS correspond to pasture, shrubs and bare soils that do not have the same high signal-to-noise ratios as PS, but they are still discernible from the background noise in SAR images elaboration. As a result, SqueeSAR algorithm, patented in 2011, jointly processes PS and DS, and make the density of radar targets higher - especially in rural and non-urban areas.

Applications

Bianchini et al., 2019 derived inventories of ground subsidence using (PSI) data of ENVISAT and SENTINEL-1 satellites for the Grosseto plain (Tuscany Region, Italy) from two inventories referred to distinct temporal intervals (2003-2009 and 2014-2019). The maximum subsidence rate observed is 16 mm/yr in 2003-2009 and 25 mm/yr in 2014-2019, occurring over floodplain deposits.

Calo et al., 2017, exploited data from the European Space Agency (ESA) archives, collected by the ENVISAT-ASAR satellite of 35-day revisit period. Two data sets of ascending and descending orbits were exploited used the SB-AS-DInSAR technique by selecting SAR data pairs and generated interferograms. In the ENVISAT case the ground resolution of the DInSAR deformation rate map turns to be about 80 m^2 x 80 m^2 which is particularly suitable to investigate land subsidence occurring at regional level. From the inspection of the achieved time series significant vertical displacement was reached, up to 10 cm, with an average deformation rate of 0.15 cm/y for a period of 8 years.

Chang and Hanssen (2014) used radar interferometric time series to detect migration of cavity in an urban environment, under the city of Heerlen, in the Netherlands. Time series analysis between 1992 and 2011 revealed localized vertical deformation rates, of ~3 mm/yr for a period of 18 years, which was followed by a deformation increase of up to ~15 mm/year. However, no detectable subsidence preceded sinkhole collapse.

Refice et al. (2016) used ascending and descending SAR data, and processed through PSI techniques, showed displacement velocities on the Lesina Marina area, in Southern Italy and observed PS objects undergoing displacement, along the LOS. These results were in agreement with high accuracy leveling, and overall geological interpretation. According to the authors this confirms the importance of the integration between in situ, geologic and geophysical, data and methods. Refice et al., 2016, suggest though that when the cover material is depicting compaction characteristics, then, micro precursory intermittent deformations, could occur which cannot be detected by remote sensing.

Osmanoglu et al. (2016), compared four algorithms (PSI, SBAS and SqueeSAR, StaMPS), developed for time series analysis of InSAR data using an example set of results for

measuring subsidence rates in Mexico City. The high subsidence rate of Mexico City provides a strong interferometric signal they found that subsidence is highly linear through time.

Theron et al., 2017 used conventional DInSAR techniques and a time-series of data revealed the presence of a deformation basin of 8300 m^2 in extent with a total observed subsidence of 100 m in diameter and 66.7 mm in depth. The deformation was continuing for a period of 2 months. The subsidence rate was non-linear over time and the subsidence activity was detected on three successive interferograms over a 55-day period and was later verified through field surveys. Four months after the detection of subsidence event, a high-pressure water supply pipeline burst downwards.

Othman et al., 2018, adopted an integrated approach combining field, and Interferometric Synthetic Aperture Radar (InSAR), hydrogeology, geodesy, and spatial analysis to further study the nature, of deformational features (sinkholes, fissures, differential settling) reported over fossil aquifers in arid lands, in northern Arabia due to excessive water extraction. InSAR-based high subsidence rates (- 4 to - 15 mm/year) were largely found within the imaged area, yet no precursory indicators were identified.

Baer et al. (2018) detected sinkhole precursory subsidence by high-resolution InSAR in the cemented alluvial fans and mudflats, in the Dead Sea. They performed numerical simulation using viscoelastic damage rheology numerical modeling to estimate sinkhole precursory times for different sedimentary environments and found that uniform width of the subsidence areas and the accelerated subsidence rate throughout the precursory period suggest that while cavity-related damage propagates upward, the actual cavity remains at a constant depth.

Martel et al. (2018) used a multidisciplinary approach to study the karst aquifer system in the city of Quebec. They used a multidisciplinary approach, combining Electric resistivity tomography (ERT), ground penetrating radar (GPR), InSAR and tracer test. The produced maps indicated stable points with sparsely distributed points (movement of 2-3 mm/y). The authors mention that unstable points do not necessarily correspond to ground vertical movement if they are isolated and studied each individual cluster. They indicated that a major limitation of the PSInSAR method lies in distinguishing terrain movement from target instability.

Vaccari et al., 2018 used SqueeSAR datasets acquired by Cosmo-SkyMed (CSK) spanning over 4 years Aug 2011 to Nov 2014, for approximately every 16 days. The results gave an average displacement rate of ± 45 $mm*y^{-1}$. Geologists from Virginia department of transportation indicated that 78% of these detections presented strong evidence of subsidence.

Ng et al. (2018), characterized the surface deformation in Guangzhou and Foshany, in China through time series between 2011 and 2017, using COSMO-SkyMed (CSK). They found that significant surface displacement rates occurred in the study area varying from -35 mm/year (subsidence) to 10 mm/year (uplift). The results indicated that linear trends of displacement in most areas, which were characterised as stable. An event occurred later on in February 2018, which was not detected, and the authors argued that this event was related to heavy loading of the road and necessarily underground excavation.

Nof et al., 2019 present the results of over six years of systematic high temporal and spatial resolution interferometric synthetic aperture radar (InSAR) observations, were fused with Light Detection and Ranging (LiDAR) measurements. The combined data enabled to detect to minute precursory subsidence before the catastrophic collapse of the sinkholes and to sinkhole susceptibility maps.

Kim and Lu (2017), and later Kim et al. (2019), studied sinkhole collapses associated with intense hydrocarbon drilling and production activities in the Hendrick oilfield, Wink, Texas. Time-series InSAR measurements using high-resolution (~25 cm) staring spotlight TerraSAR-X revealed spatiotemporal details about the status of the existing sinkholes and neighboring regions. They conclude by raising the question: “will the rapid ground subsidence

turn into another collapse sinkhole?" They note that it is difficult to predict the future of unstable surface. The subsiding area already underwent more than a10-year subsidence of tens of centimetre per year without collapse.

1.3.2 Ground based methods

Intrieri et al. (2015) used ground base interferometry GB-InSAR on Elba Island (central Italy), to investigate on the acquisition of high resolution and high precision displacement maps. Nine sinkholes were monitored for a period of seven years. Based on the observations GB-InSAR only measures the component of the movement parallel to its LOS (line of sight), they also report that a sinkhole of 1.5-m-wide occurred and was not detected by the instrument, which indicates the limits of the method. Yet deformation prior to two events was recorded with a very short time between the detection of precursors and the collapse.

One of the problem earth scientists face when using SAR interferometry is the limit of spaceborne techniques. Sinkholes usually develop in very small time, over limited areas, which is why can't always be detected, especially precursor signs or terrain movements. Small precursory episodic deformation not detectable by remote sensing.

Ferretti et al., 2011 stressed that a proper joint process of permanent scatterer and distributed scatterer can significantly improve the density and quality of InSAR measurement points, over non-urban areas.

In arid climates most interferograms give a complete spatial coverage, which renders easy to detect incoherent space due to soil collapse (Atzori et al., 2015)

Fillin et al., 2014 and Gutiérrez et al., 2019 document that terrestrial laser scanning has extreme potential into detecting precursor phenomena, preceding sinkhole formation

1.3.3 Subsurface based methods

In recent years with the revolution of sensing and communication techniques, there are many possibilities to instrument structures, receive rich information to monitor, assess, and plan of existing infrastructure networks. During the last decade, fiber-optic sensing has become a widely accepted, mature technology, widely used in a range of applications. Collection and monitoring of more information is part of the big data trend, which is becoming increasingly important.

Regular assessment can identify sinkhole formation susceptible areas. The remote sense observation even when integrated with other monitoring methods, provides little or no information on subsurface process, that are precursor to incipient collapse. There is a growing interest from asset owners in more pervasive approaches that would allow more widespread monitoring of the ground hosting infrastructure (Smerthurst et al., 2017).

Installation of fiber optic sensor is proposed in urban environments to monitor strain and temperature variations along existing water service networks. There is a need to invest to the implementation of early warning systems integrated smart, monitoring, could effectively monitor ground deformation, detect precursor phenomena, and support sinkhole hazard, risk mitigation, and enhance urban planning development.

Soga and Schooling (2016), remark that infrastructure monitoring is not new, yet recently sensor and communication research have been undergoing a revolution. There are currently possibilities to use these emerging technologies to distributed fibre optic sensors and wireless sensor networks to address particular need and look after the existing infrastructure, this obviously applies to sinkhole and subsidence phenomena.

Fibers could be buried longitudinally, and thus cover long distances, yet there are limitation related to the high cost, of the interrogator equipment. Although optical fiber sensors

are widespread in structural health monitoring, their use in geotechnical engineering is limited. The performance of Time Domain Reflectometry (TDR) and Brillouin Optical Time Domain Reflectometry (BOTDR) for sinkhole monitoring has been barely explored. Three papers explore the potential capability of (BOTDR) to detect precursory subsidence preceding the occurrence of collapse sinkholes (Lanticq et al., 2009, O'Connor and Trainum, 2015, Jiang et al., 2015). These novel techniques may provide subsidence measurements along long lines (e.g. communication infrastructure) but may be adversely affected by temperature changes, vibrations, and processes non-related to sinkhole activity.

Lanticq et al., 2008, performed sinkhole detection using both B-OTDR and OFDR techniques with two different optical fibers of the same sensing cable embedded in the soil. The main limitation of such a warning system is that it cannot distinguish a large and distant cavity from a smaller and closer one, unless a network of sensing cables is deployed. Yet further field test, are required to validate the results.

O'Connor and Trainum (2015), presented an alternative approach to monitor ground deformation of US 18 in cerro Gordo County, Iowa, by removing the existing pavement, installing coaxial cables, in excavated trenches, replacing the pavement with double reinforced, and subsequent monitoring the cables using Time Domain Reflectometry (TDR). The cables were interrogated several times a day and data were transmitted via cellular modem to Iowa DOT facilities. Although activity has been detected in each of the eight coaxial cables, there was no definitive correlation between TDR activity locations, sinkhole locations, or geophysical anomaly locations.

Jiang et al., 2016, used an experimental study of monitoring the process of sinkhole collapse using BOTDR. In a series of tests of an experimental model, sinkholes are induced by pumping simulated karst water. Real time strains of optical fibers buried in sediments and soil damages were measured. Results of the experimental study demonstrate that positions of peak strain in optical fibers correspond well to areas of maximum disturbance and soil void formation. Changes of optical fiber strains in different soil layers are good indicators of vertical disturbance in soil. This technology could potentially become a useful tool to monitor and predict sinkhole collapse and subsidence, especially along linear infrastructure such as roads, highways and railways. In practice, optical fibers need to be buried as deep as possible or more carefully to avoid sliding movement of optical fibers.

Labuschagne et al. (2019) and Ferentinou (2020) studied sinkhole formation in fine dry silica sand in a small-scale physical models which included a balloon full of water, to simulate the formation of the sinkhole. Fibre optic cables with brag gratings sensors (FBGs) were laid in the soils at various levels above the balloon. The model included a Perspex window which allowed photographs of the soil movement to be taken. It was evident that the strain sensors closest to the surface experienced the smallest strains, and greatest strains, coincided with the greatest soil disturbance. None of the sensors failed or were damaged during the test, showing that this instrumentation is suitable for use in physical model studies. The incorporation of fibre optic cables into earthworks could provide an opportunity for significantly improved information on the location mechanism and magnitude of ground movement in real time. This method could potentially allow for sensing along longer distances every few metres, for surface or near surface settlement as a result of a formation of underground voids. This technology could serve as a long-term monitoring solution.

1.4 Precursor phenomena detection and times

In general, measurable deformation have been observed before major displacement occurs, although the main limitation lies in the opportunity to observe such deformation, especially when they occur in the underground environments.

The literature documenting detection of precursor phenomena through the use of satellite remote sensing is very limited (Hensley, 2009; Nof et al., 2013; Jones and Blom, 2014) and more recently Atzori et al., 2015; Anvi et al. (2016) and Baer et al., 2018. Many researchers (Intrieri et al., 2015, Baer et al., 2018, Gutiérrez et al., 2019), mention, that there is a need for identification of precursory deformation prior to the catastrophic main sinkhole events. Baer et al. (2018), are indicating that the temporal relationships between subsidence and sinkhole collapse and particularly the factors controlling the duration of the precursory subsidence are still poorly understood.

Nof et al., 2013, where the first to report on sinkhole precursors using COSMOSkyMed satellite images fused with a high-resolution (0.5 m/pixel) DEM obtained from LiDAR measurements. Millimetre-scale subsidence was recorded, and signs of small-scale precursory deformation was measured over a period of a few months before the collapse of three sinkholes in the Dead Sea karstic environment.

Three more papers were published reporting precursory subsidence for the Dead Sea environment. Precursor subsidence was recorded for a period of a 2-5 months before the date of the sinkhole event. Expression of subsidence on the surface and associated migration of the center sinkhole clusters, was also identified through the InSAR processing. Two-year timeseries (12 and 6 interferometric images per patch selected) were used. The rate of subsidence was 3 mm/month and accelerated to 2 cm/month prior to three consecutive events that occurred within a month. In this case X-band radar images of the Italian Space Agency (ASI) COSMO-SkyMed with full resolution of about 2.5 m were processed. Filtering was required for atmospheric corrections, and the topographic effect was removed using a down sampled Lidar image relevant to the resolution of the InSAR pixel size of 2.5 (Atzori et al., 2015).

Anvi et al. (2016), report on minor displacement detected in association with flash flood events. During the preflood time interval, a significant increase in the rates and spatial extents of land displacements was evident in several areas along the major streambeds. In the time intervals after the flood event, reaching about 2 cm in each 16 day interval (i.e. >1 mm/d). High rates appear in lineaments and areas that were also noted for their high-subsidence rates during the long-term 2011-2015 period. Baer et al., 2018 demonstrate that precursory subsidence has been detected before the collapse of most sinkholes along the Dead Sea. They do however acknowledge, that the limitations of the InSaR method, allowing for imaging on 16-day intervals. The method would be adequate only for phenomena where precursory subsidence is evident over a larger period of time than 16 days. Nevertheless, based on the experience, studying the sinkholes in the Dead Sea region. Sinkhole precursory times as detected through InSAR X-band radar images of the Italian Space Agency (ASI) COSMO-SkyMed, ranged from 32 ± 16 days, 92 ± 8 days, are 88 ± 8 days, 66 ± 8 days In this case the results of the InSAR observations were compared to the viscoelastic model predictions, and revealed that there is linear correlation between the depth of the salt layer and the precursory time. The study reports on exponential correlations between the diameter of the sinkhole and the precursory time, and the composition of the material and the precursory time. The simulation time is measured from the onset of deformation above the subsurface cavity to collapse, while InSAR measurements of precursory subsidence starts at the first detectable surface deformation. Thus, in areas with low percentage of cemented gravel, warnings may be missed as sinkholes may form before any subsidence could be detected. However, as the majority of sinkholes, and particularly the deeper and abruptly forming (more dangerous) ones follow subsidence periods of weeks to years, they are highly appropriate for early warning.

1.5 Conclusions

As part of the process of sinkhole risk management, hazard evaluation, and susceptibility mapping sinkhole inventories or catalogues need to be compiled as reliably as possible. Satellite and airborne imaging technologies offered geoscientists the opportunity to collect valuable data, which serve as input to sinkhole hazard assessment models in a short period of time and under a cost-effective way.

Because of the broad spatial coverage, and the high update frequencies offered by satellite-based remote sensing data, the user can receive almost real-time overview of the overall imaged area. Consequently, one can claim that there is better guidance to the relevant stakeholders in decision making about existing infrastructure assessment, monitoring, and further planning.

Remote sensing methods both satellite, and airborne imaging have been widely used to support sinkhole susceptibility assessment. The use of these methods either supports the compilation of extensive sinkhole catalogues, Gillespie et al. (2007), Baer et al. (2018), or focuses on to the detection of indicators as precursor phenomena. Lacasse and Nadim (2008), Intrieri et al. (2013), mention that although extracting subsidence deformation in previously identified sinkhole-prone areas gives valuable information for proactive urban planning, that could also produce many false alarms, as not every subsidence deformation leads to a sinkhole; Another challenge is that instrumental noise could be incorrectly identified as deformation.

Satellite Synthetic Aperture Radar Interferometry (InSAR) techniques are able to complement the field studies, and explore the evolution of sinkhole formation, with millimetre precision, in wide scales (Chang and Hanssen, 2014; Theron et al., 2017, Baer et al., 2018). As confirmed from the recent literature, Satellite Synthetic Aperture Radar Interferometry (InSAR) techniques have been very successfully used during the last decade, and can support the widely used field geomorphological mapping, surveying and geophysical methods and sense the evolution of sinkhole formation, with millimetre precision, in wider areas.

InSAR bridges the gap between periodic and continuous monitoring. This is a mature widely adopted technology to monitor critical infrastructure. Can also be used for operational monitoring.

Obtaining information on the spatial and temporal evolution of land subsidence plays an important role on hazard assessment and may significantly contribute to risk prevention and mitigation. However, the continuous monitoring of surface deformations at regional/basin scale is a resource-intensive task to be accomplished by using traditional ground-based techniques. The use of satellite-based information in Earth's surface studies represents an important breakthrough, fulfilling the requirements of high spatial and temporal coverage.

Complementary application of various types of monitoring systems will help in the gathering of multi-field information prior to a sinkhole formation. It will offer a novel monitoring method for sinkhole development analysis as well as early warning.

The main problem for risk assessment is the lack of a priori knowledge on the location of a potentially hazardous cavity. The ability to detect ground deformation indicative of prior to failure allows for proactive remediation, increasing public safety and minimising infrastructural damage (Vaccari et al., 2013). Monitoring needs to be continuous, reliable, and reported in near real time, with clear criteria, to suit the level of expertise needed to make judgement (Stahli, 2014). Could we have an alarm system?

InSAR analysis can be used to screen large areas for anomalous vertical movement and guide more intensive field investigations to areas where significant change is occurring. Satellite based InSAR, owing to frequent ongoing acquisition of data, provides a ready method for monitoring future movement in sinkhole-prone areas. However, based on the literature discussed previously for smaller areas, or sinkhole susceptible regions, spatial resolution may

be insufficient. In addition, the data acquired are usually limited to surface or near surface information. The temporal resolution is generally restrained, by the flight schedules and orbits.

A novel extension of various methods currently being used for the monitoring of natural and anthropogenic geohazards associated with phenomena of sinkhole formation and cover-collapse. Specifically, the focus is proposed to be on the critical problems associated with the formation and monitoring of sinkholes by exploiting two different technologies and their pertinent practical implementation aspects in a combined two-scale approach: (a) by using satellite radar interferometry (InSAR) to resolve temporal and spatial relationships between gradual subsidence and sinkhole collapse in wider areas, and (b) dealing with the field implementation of fiber optics-based monitoring systems to provide for an early warning tool for likely impending failure. The effective combination of these two technologies would, lead on building new knowledge of the ways in which such a combined approach can be embedded into ongoing practice for future monitoring efforts in similar geohazards-prone areas.

According to Smerthurst et al., 2017, "there is considerable potential for the changing demands and expectations of infrastructure systems and new monitoring techniques to completely change the way of monitoring in the future. It would be possible to monitor greater lengths, with the intention of providing warning, and as a result the reducing incidence of unexpected failures. Rather that the fairly reactive monitoring approaches, commonly seen today".

1.6 References

1. Atzori, S., G. Baer, A. Antonioli, and S. Salvi (2015), InSAR-based modeling and analysis of sinkholes along the Dead Sea coastline, Geophys. Res. Lett.,42, 8383-8390, doi:10.1002/2015GL066053.
2. Avni, Y., Nadav Lensky, Elad Dente, Maayan Shviro1, Reuma Arav, Ittai Gavrieli, Yoseph Yechieli, Meir Abelson, Hallel Lutzky, Sagi Filin, Itai Haviv and Gidon Baer (2016), Self-accelerated development of salt karst during flash floods along the Dead Sea Coast, Israel, J. Geophys. Res. Earth Surf.,121, 17-38, doi:10.1002/2015JF003738.
3. Baer, G., Magen, Y., Nof, R. N., Raz, E., Lyakhovsky, V., & Shalev, E. (2018). InSAR measurements and viscoelastic modeling of sinkhole precursory subsidence: Implications for sinkhole formation, early warning, and sediment properties. Journal of Geophysical Research: Earth Surface, 123, 678-693.
4. Berardino, P.; Fornaro, G.; Lanari, R.; Sansosti, E. A new algorithm for surface deformation monitoring based on small baseline differential SAR interferograms. IEEE Trans. Geosci. Remote Sens. 2002, 40, 2375-2383.
5. Bianchini, S., Solari, L, Del Soldato, M, Raspini, F, Montalti, R, Ciampalini, A., Casagli, N., Ground Subsidence Susceptibility (GSS) Mapping in Grosseto Plain (Tuscany, Italy) Based on Satellite InSAR Data Using Frequency Ratio and Fuzzy Logic, Remote Sens. 2019, 11, 2015; doi:10.3390/rs11172015
6. Brinkmann, R., Wilson, K., Elko, N., D Seale, L., Florea, L., Vacher, H. (2007). Sinkhole distribution based on pre-development mapping in urbanized Pinellas County, Florida, USA. Geography/Geology Faculty Publications. 279. 10.1144/SP279.2.
7. Buttrick, D.B., Trollip, N.Y.G., Watermeyer, R.B., Pieterse, N., Gerber, A.A., 2011. A performance-based approach to dolomite risk management. Environment Earth Sciences 64, 1127-1138.

8. Caló F., Notti D., Galve J.P., Abdikan S., Görüm T., Pepe A., Şanli F.B., DInSAR-based detection of land subsidence and correlation with groundwater depletion in Konya plain, Turkey, Remote Sens. 2017, 9, 83; doi:10.3390/rs9010083
9. Calvo, A.B, Gutiérrez, F., Martínez-Fernández, A, Carbonel, D., Karampaglidis, T., Desir, G., Sevil, J, Guerrero, J., Fabregat, I., García-Arnay, A. (2018), 4D Monitoring of Active Sinkholes with a Terrestrial Laser Scanner (TLS): A Case Study in the Evaporite Karst of the Ebro Valley, NE Spain, Remote Sens, 10(4), 571
10. Chang, L., Hanssen, R. (2014) Detection of cavity migration and sinkhole risk using radar interferometric time series, Remote Sensing of Environment 147, 56-64
11. Chaussard, E.; Milillo, P.; Burgmann, R.; Perissin, D.; Fielding, E.J.; Baker, B. Remote sensing of ground deformation for monitoring groundwater management practices: Application to the Santa Clara Valley during the 2012-2015 California drought. J. Geophys. Res. B Solid Earth 2017.
12. Constantinou, S., van Rooy, LJ (2018), Sinkhole and subsidence size distribution across dolomitic land in Gauteng, Journal of the South African, Institution of Civil Engineering, ISSN 1021-2019, Vol 60 No 2, June 2018, Pages 2-8, Paper 1373
13. Del Prete, S., Di Crescenzo, G., Santangelo, N. and Santo, A. (2010), Collapse sinkholes in Campania (southern Italy): predisposing factors, genetic hypothesis and susceptibility, Zeitschrift für Geomorphologie Vol. 54, Suppl. 2, 259-284.
14. Dehghani, M.; Javad Valadan Zoej, M.; Hooper, A.; Hanssen, R.F.; Entezam, I.; Saatchi, S. Hybrid conventional and Persistent Scatterer SAR interferometry for land subsidence monitoring in the Tehran Basin, Iran. ISPRS J.
15. Photogramm. Remote Sens. 2013, 79, 157-170. [CrossRef]
16. Dippenaar, M., van Rooy, L., Diamond, L. (2019), Engineering, hydrogeological and vadose zone hydrological aspects of Proterozoic dolomites (South Africa), Journal of African Earth Science, 150, 219, 511-521.
17. Dogan, U., Yilmaz, M., 2011. Natural and induced sinkholes of the Obruk Plateau and Karapinar-Hotamis Plain, Turkey. J. Asian Earth Sci. 40, 496-508.
18. Dou, J., Li, X., Yunus, A.P. Paudel, U., Chang, K.T., Zhu, Z., Pourghasemi, H.R., (2015) Automatic detection of sinkhole collapses at finer resolutions using a multi-component remote sensing approach, Nat Hazards (2015) 78:1021-1044, DOI 10.1007/s11069-015-1756-0
19. Drumn, E; Aktürk, O; Akgün, A, Tutluoğlu, T, Stability Charts for the Collapse of Residual Soil in Karst (2009), J. Geotech. Geoenviron. Eng., 2009, 135(7): 925-931
20. Dougherty, P., 2005. Sinkhole destruction of corporate plaza, Pennsylvania. In: Waltham, T., Bell, F.G., Culshaw, M.G. (Eds.), Sinkholes and Subsidences. Praxis Publishing Ltd., Chichester, pp. 304e308.
21. Fairbridge, R.W., 1968. The Encyclopaedia of Geomorphology. In: Reinhold (Ed.) (New York, 1295 pp.).
22. Ferretti, A.; Prati, C.; Rocca, F. Permanent scatterers inSAR interferometry. IEEE Trans. Geosci. Remote Sens, 2001, 39, 8-20.
23. Ferretti, A., A. Fumagalli, F. Novali, C. Prati, F. Rocca, and A. Rucci. (2011) A New Algorithm for Processing Interferometric Data-stacks: SqueeSAR. IEEE Transactions on Geoscience and Remote Sensing, Vol. 49, No. 9, 2011, pp.3460-3470.
24. Filin, S., Baruch, A., 2010. Detection of sinkhole hazards using airborne laser scanning data. Photogram. Eng. Remote Sens. 76 (5), 577-587.

25. Filin, S.; Avni, Y.; Baruch, A.; Morik, S.; Arav, R.; Marco, S. Characterization of land degradation along the receding Dead Sea coastal zone using airborne laser scanning. Geomorphology 2014, 206, 403-420.
26. Galve, J.P.; Gutiérrez, F.; Remondo, J.; Bonachea, J.; Lucha, P.; Cendrero, A. Evaluating and comparing methods of sinkhole susceptibility mapping in the Ebro Valley evaporite karst (NE Spain). Geomorphology 2009, 111, 160-172.
27. Gutiérrez, F., Calaforra, J.M., Cardona, F. et al. (2008) Geological and environmental implications of the evaporite karst in Spain. Environ Geol 53, 951-965 (2008). https://doi.org/10.1007/s00254-007-0721-y
28. Gutiérrez, F., Parise, M., De Waele, J., Jourde, H. (2014). A review on natural and human-induced geohazards and impacts in karst. Earth Science Reviews, 138, 61-88. https://doi.org/10.106/j.earscirev.2014.08.002
29. Gutiérrez, F., Calvo, A.B., Carbonela, D., Desira, G., Sevila, G., Guerrero, J., Fernández E., Karamplaglidis, T., Arnay, A., G, Fabregat, I. (2019), Review on sinkhole monitoring and performance of remediation measures by high-precision leveling and terrestrial laser scanner in the salt karst of the Ebro Valley, Spain, Engineering Geology 248, 283-308
30. Hensley, S., Zebker, H., Jones, C., Michel, T., Muellerschoen, R., and Chapman, B., 2009, First deformation results using the NASA/JPL UAVSAR instrument, in Proc. of the Second Asian-Pacific Conference on Synthetic Aperture Radar: Piscataway, New Jersey, IEEE, p. 1051-1055.
31. Hyatt, J.A., Wilkes, H.P., Jacobs, P.M., 1999. Spatial relationships between new and old sinkholes in covered karst, Albany, Georgia, USA. In: Beck, B.F., Herring, J.G. (Eds.), Hydrogeology and Engineering Geology of Sinkholes and Karst. Balkema, Rotterdam, pp. 37-44.
32. Intrieri, E., Gigli, G., Nocentini, M., Lombardi, L., Mugnai, F., Fidolini, F., Casagli, N. (2015), Sinkhole monitoring and early warning: An experimental and successful GB-InSAR application. Geomorphology 2015, 241, 304-314.
33. Jacobsz, S.W., 2016, Trapdoor experiments studying cavity propagation, in Proceedings of the first Southern African Geotechnical Conference, Sun City, South Africa, 2016.
34. Jennings, J. E., Brink, A.B.A., Louw, A. & Gowan, G.D.1965. Sinkholes and subsidence in the Transvaal dolomites of South Africa: 51-54. Proc 6th International Conference on Soil Mechanics. Montreal, Canada: 51-54
35. Jones, C., Blom, R. (2014) Bayou Corne, Louisiana, sinkhole: Precursory deformation measured by radar interferometry GEOLOGY, February 2014; v. 42; no. 2; p. 111-114 doi:10.1130/G34972.1
36. Kemmerly, P.R., 1982. Spatial analysis of a karst depression population; clues to genesis. Geol. Soc. Ameri. Bull. 93, 1078-1086.
37. Kim, J., Lu, Z. (2017) Temporal Deformation of wink sinkholes in west Texas Observed by spaceborne SAR imagery, IGARSS, 2017
38. Kim, J., Lu, Z., Kaufmann, J., Evolution of sinkholes over Wink, Texas, observed by high-resolution optical and SAR imagery (2019), Remote Sensing of Environment 222 119-132

39. Lacasse, S., Nadim, F., 2008. Landslide risk assessment and mitigation strategy. In: Sassa, K., Canuti, P. (Eds.), Landslides – Disaster Risk Reduction. Springer, Verlag Berlin, Heidelberg, pp. 31-61.
40. Labuschagne, J., Ferentinou, M., Grobler, M., Jacobsz, SW, Smart monitoring of sinkhole formation using optic fibre technology (3rd ICITG).
41. Linker A., Klar, A. (2017), Detection of Sinkhole Formation by Strain Profile Measurements Using BOTDR: Simulation Study, Journal of Eng. Mech., 1143 (3), 1.
42. Magdalene, S., Alexander Jr., E.C., 1995. Sinkhole distribution in Winona County, Minnesota revisited. In: Beck, B.F., Person, F.M. (Eds.), Karst Geohazards. Balkema, Rotterdam, pp. 43-51.
43. Malimowska et al. (2018), Engineering Geology
44. Martel, R., Castellazzi, P., Gloaguen, E., Trépanier, Luc., Garfias, J. (2018) ERT, GPR, InSAR, and tracer tests to characterize karst aquifer systems under urban areas: The case of Quebec City, Geomorphology, Volume 310, pp. 45-56, ISSN 0169-555X, https://doi.org/10.1016/j.geomorph.2018.03.003.
45. McConnell, H., Horn, J.M., 1972. Probabilities of surface Karst. In: Chorley, R.J. (Ed.), Spatial Analysis in Geomorphology. Harper and Row, New York, pp. 111-133.
46. Mora, O.; Mallorqui, J.J.; Broquetas, A. Linear and nonlinear terrain deformation maps from a reduced set of
47. interferometric SAR images. IEEE Trans. Geosci. Remote Sens. 2003, 41, 2243-2253. [CrossRef]
48. Ng A., Wang, H., Dai, Y., Pagli , C., Chen, W., Ge, L., Du, Z., Zhang, K., InSAR Reveals Land Deformation at Guangzhou and Foshan, China between 2011 and 2017 with COSMO-SkyMed Data, Remote Sens. 2018, 10, 813; doi:10.3390/rs10060813.
49. Nof, R.N.; Baer, G.; Ziv, A.; Raz, E.; Atzori, S.; Salvi, S. Sinkhole precursors along the Dead Sea, Israel, revealed by SAR interferometry. Geology 2013, 41, 1019-1022.
50. Nof., R., Abelson, M., Raz, E., Magen, Y., Atzori, S., Salvi, S., Baer, G. (2019) SAR Interferometry for Sinkhole Early Warning and Susceptibility Assessment along the Dead Sea, Israel, Remote Sens. 2019, 11, 89; doi:10.3390/rs11010089
51. Osmanoglu, B., Sunar, F., Wdowinski, S., Cabral-Cano, E. (2016) Time series analysis of InSAR data: Methods and trends ISPRS Journal of Photogrammetry and Remote Sensing 115 (2016) 90-102
52. Othman, A, Sultan, M., Becker, R., Alsefr, S., Alharbi, T., Gebremichael, E., Alharbi, H., Abdelmohsen, K. (2018), Use of Geophysical and Remote Sensing Data for Assessment of Aquifer Depletion and Related Land Deformation, Surv Geophys (2018) 39:543-566
53. Paine, J., Buckley, S, Collins, E., Wilson, C. (2012) Assessing Collapse Risk in Evaporite Sinkhole-prone Areas Using Microgravimetry and Radar Interferometry, Journal of Environmental and Engineering Geophysics JEEG, June 2012, Volume 17, Issue 2, pp. 75-87.
54. Parise M, Lollino P. 2011. A preliminary analysis of failure mechanisms in karst and man-made underground caves in Southern Italy. Geomorphology 134 (1-2): 132-143
55. Parise, M.; Closson, D.; Gutiérrez, F.; Stevanovic, Z. (2015) Anticipating and managing engineering problems in the complex karst environment. Environ. Earth Sci., 74, 7823-7835.

56. Rahimi, M., Alexander, E.C., Jr., 2013. Locating sinkholes in LiDAR coverage of a glacio-fluvial karst, Winona County, MN. In: Conference Proceedings – 13th Multidisciplinary Conference on Sinkholes and the Engineering and Environmental Impacts of Karst, University of South Florida. pp. 469-480.
57. Rajabi, A.; Kim; Y., Kim; S.H., Kim YS., Kim, BJ., Nam, BH., A Preliminary Study on Use of LiDAR Data to Characterize Sinkholes in Central Florida, IFCEE 2018 GSP 295.
58. Refice, A., Pasquariello, G., Bovenga, F, Festa, V, Acquafredda, P, Spilotro, P. (2016) Investigating uplift in Lesina Marina (Southern Italy) with the aid of persistent scatterer SAR interferometry and in situ measurements.
59. Youssef, A., El-Shater, M. H. El-Khashab, B. El-, Haddad1, Coupling of field investigations and remote sensing data for karst hazards in Egypt: case study around the Sohag City, Arab J Geosci (2017) 10: 235.
60. Soga K, Schooling J. 2016, Infrastructure sensing. Interface Focus 6: 20160023. http://dx.doi.org/10.1098/rsfs.2016.0023
61. Sowers, G. F. 1996. Building on sinkholes: Design and construction of foundations in karst terrain, ASCE, New York.
62. Smethurst, J.A, A. Smith, S. Uhlemann, C. Wooff, J. Chambers, P. Hughes, S. Lenart, H. Saroglou, S. M. Springman, H. Löfroth and D. Hughes, Current and future role of instrumentation and monitoring in the performance of transport infrastructure slopes, Quarterly Journal of Engineering Geology and Hydrogeology, 50, 271-286, 27 July 2017, https://doi.org/10.1144/qjegh2016-080
63. Stahli, M., Sattele, M. et al., 2014, Monitoring and prediction in Early warning systems (EWS), for rapid mass movements. Natural Hazards and Earth system Sciences (NHESS), 2, 7149-7179.
64. Theron, A.; Engelbrecht, J.; Kemp, J.; Kleynhans, W.; Turnbull, T. (2017) Detection of Sinkhole Precursors through SAR Interferometry: Radar and Geological Considerations. IEEE Geosci. Remote Sens. Lett. 2017, 14, 871-875.
65. Theron, A.; Engelbrecht, J (2018), The Role of Earth Observation, with a Focus on SAR Interferometry, for Sinkhole Hazard Assessment, Remote Sens. 2018, 10, 1506; doi:10.3390/rs10101506.
66. Tomás, R., Romero, R., Mulas, J. et al. (2014) Radar interferometry techniques for the study of ground subsidence phenomena: a review of practical issues through cases in Spain Environ Earth Sci (2014) 71: 163. https://0-doi-org.ujlink.uj.ac.za/10.1007/s12665-013-2422-z
67. The Guardian, https://www.theguardian.com/world/sinkholes?page=6., 28/03/2019.
68. Vaccari, A.; Stuecheli, M.; Bruckno, B.; Hoppe, E.; Acton, S.T. Detection of geophysical features in InSAR point cloud data sets using spatiotemporal models. Int. J. Remote Sens. 2013, 34, 8215-8234.
69. Zebker, H.A.; Villasenor, J. Decorrelation in interferometric radar echoes. IEEE Trans. Geosci. Remote Sens.1992, 30, 950-959.
70. Zhou, W.; Beck, B.F. (2008), Management and mitigation of sinkholes on karst lands: An overview of practical applications. Environ. Geol., 55, 837-851.
71. Zhu, J.; Pierskalla, W.P., Jr. (2016). Applying a weighted random forests method to extract karst sinkholes from, LiDAR data. J. Hydrol. 2016, 533, 343-352.
72. Zhu, J., Taylor, T.P., Currens, J.C., Crawford, M.M. (2014). Improved karst sinkhole mapping in Kentucky using LiDAR techniques: a pilot study in Floyds Fork Watershed. J. Cave Karst Stud. 76 (3), 207-216. http://dx.doi.org/10.4311/2013ES0135.

73. Waltham, T., Bell, F. G., Culshaw, M. G. (2005). Sinkholes and subsidence: Karst and cavernous rocks in engineering and construction (p. 379), Chichester, UK: Springer Praxis.
74. Weary, D. (2015), The cost of karst subsidence and sinkhole collapse in the United States compared with other Natural Hazards. 14TH SINKHOLE CONFERENCE NCKRI SYMPOSIUM 5

CHAPTER 2: PSINSAR APPLICATION IN CENTURION

2.1 Introduction

Sinkholes are considered a dangerous natural and man-made hazard, affecting transportation and infrastructure networks, responsible for property loss and fatalities, in regions underlain by soluble bedrock. In South Africa, large parts of the urban fabric between Pretoria and Johannesburg are situated on Proterozoic dolomites of the Malmani Subgroup (Chuniespoort Group, Transvaal Supergroup) formed in the Transvaal Basin. During the previous decades, in the Far West Rand, sinkholes occurrence was induced by extensive dewatering of dolomite groundwater compartments due to mining and resulted into the loss of life of 38 people (De Bruyn and Bell, 2001). A community of approximately 30 000 households was relocated to safer ground in a dolomite area west of Johannesburg, at a cost exceeding US $600 million (Buttrick et al., 2011). The rhythm of development of these densely populated areas is on the rise, as these megacities serve as the economical core of the country, increasing the risks posed by surface subsidence and sinkholes. Tshwane municipality also sources more than 40 million litres of drinking water per day (5-8% of requirements) from the dolomite aquifers (Dippenaar et al., 2019. Nof et al. (2019), propose that sinkhole potential maps are mandatory for the planning and licensing of new infrastructure. The necessity for effective monitoring and installation of early warning systems is required to reduce the risk for people, infrastructure, and property. In the current study we present on the findings of the application of PSInSAR in the Centurion area South Africa and underline the potential of the PSInSAR method for the monitoring and assessing susceptible to sinkhole hazard urban areas.

2.2 Mechanism of sinkhole formation

A sinkhole is defined as a feature whose surface expression may occur suddenly and manifests as a hole in the ground that is typically circular in plain view. In international literature the term sinkhole is often synonymous with doline (SANS, 1936, 2012). A subsidence is defined as a shallow enclosed depression that occurs slowly over time and may typically be circular, oval or linear in plan (SANS, 1936, 2012). The process of sinkhole formation is continuous dissolution of sub terrain soluble rocks, progressively leading to the development of cavities. When the soil above these cavities reach critical conditions (soil material exceeds shear strength), soil collapses, as a result of reduction of soil vertical stress. Main causes of underground cavities are the ingress of water, the lowering of groundwater table, or extensive pumping leading to dewatering (Intrieri et al., 2015; Dippenaar et al., 2019). An idealized profile in karst is illustrated in Sowers (1996). One can recognize the succession of the layers from the surface downwards to the dome and the soluble bedrock. Intrieri et al. (2015) rank among sinkhole predisposing factors, as the most dominant factor the lithology, i.e. the presence of soluble rocks subject to karstic processes, followed by the pre-existence man made underground cavities, of low geomechanical properties of the bedrock, and (acidic) groundwater circulation promoting the dissolution of evaporate and carbonate rocks.

The triggering is attributed to the input of water into the ground which in return contributes to increase the load of the soil material deposited in the vadose zone. This as a result may reduce the geomechanical strength of the soils and promote internal erosion and dissolution processes, Gutiérrez et al. (2009).

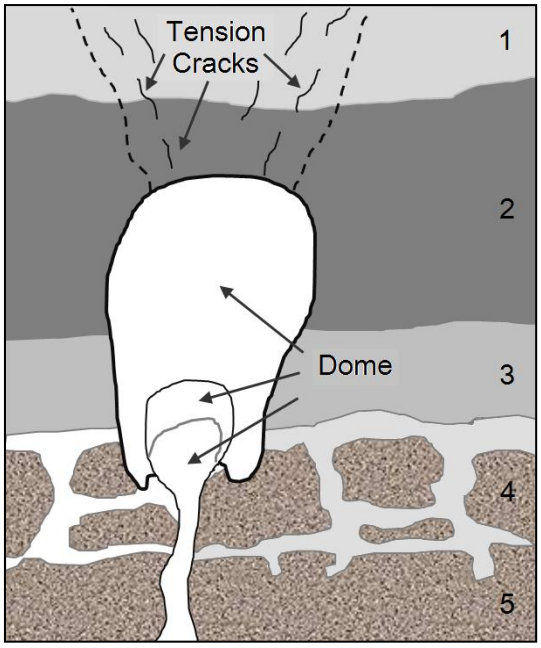

2.3 Remote sensing and sinkhole hazard

As part of the process of sinkhole risk management, hazard evaluation, and susceptibility mapping sinkhole inventories or catalogues need to be compiled as reliably as possible. Satellite and airborne imaging technologies offered geoscientists the opportunity to collect valuable data, which serve as input to sinkhole hazard assessment models in a short period of time and under a cost-effective way. Remote sensing methods both satellite, and airborne imaging have been widely used to support sinkhole susceptibility assessment. The use of these methods either supports the compilation of extensive sinkhole catalogues or focuses on to the detection of indicators as precursor phenomena. Interferometric synthetic aperture radar (InSAR) and its derivatives have proved to be the most valuable and widely used method in sinkhole mapping and long-term deformation monitoring (Gutiérrez et al., 2014, Vaccari et al., 2018). According to (Vaccari et al., 2018), challenges associated with these big datasets are primarily the development of analysis tools that can synthesize them into products meaningful to the geotechnical community.

InSAR according to Rosen et al. (2000), operates by relating the coherent phase difference between radar echoes collected from the same point on the ground at two different observation times to the path-length difference between the aircraft and the ground, enabling highly accurate measurement of surface displacement in the line-of-sight direction. Only the cumulative displacement that occurred during the time interval between the imaging is measured, InSAR cannot detect movement perpendicular to the imaging plane, but along the line of sight (LOS).

Further methods and algorithms were developed to remove topographic and atmospheric effects from the derived interferogram. The use of Differential InSAR (DInSAR) takes into account the digital elevation model (DEM) of the imaged area to remove the topographic effects. As a result, the deformation along LOS of the satellite is quantified. An advanced DInSAR technique named permanent/persistent scattered InSAR (PSInSAR) was introduced (Ferreti et al., 2011), to resolve atmospheric interference problems. Vaccari et al. (2018) state that for those locations (permanent/persistent scatterer – PS) that have a large signal-to-noise ratio across several SAR images, PSInSAR can deliver deformation measurements with an accuracy of less than 1 cm. PS method gives better results, when features

such as rocky outcrops, lamp posts, crash barriers, transmission towers, fences, buildings exist in the imaged area. Thus, in rural areas, the density of PS can be extremely low. The introduction of an improved version of PSInSAR, SqueeSAR (10) usually refers to as the second generation of PSInSar, with an additional layer of statistical analysis is used to identify regions providing a consistent and traceable response to the radar pulses over time.

However, the literature documenting detection of precursor phenomena through remote sensing is very limited. Many researchers (Intrieri et al., 2015; Baer et al., 2018; Guttiérrez et al., 2018; Malinowska et al., 2019), mention, that there is a need for an identification of precursory deformation prior to the catastrophic main sinkhole events. Baer et al. (2018), suggest that the temporal relationships between subsidence and sinkhole collapse and particularly the factors controlling the duration of the precursory subsidence are still poorly understood.

2.4 PSInSAR application in Centurion.

Persistent Scatterers (PS) as previously discussed, is a multi-interferometric technique which enables to generate displacement time-series for chosen radar targets. The general assumption of PS model is a linear temporal velocity of ground movement (Ferreti et al., 2011). Based on this assumption the reliability of ground motion observation allows to be described through standard deviation. The accuracy of PS method ranges from 0.1-1 mm/year in the LOS direction (Colesanti et al., 2003). One of the challenges when applying this method is that PS with high standard deviation values could present process artefacts due to low signal-to noise ratio or non-linear motion. Thus, the analysis of spatial correlation among PS with high standard deviation could lead to identification of zones with non-linear displacement velocities.

On the 17th of May 2017 a massive sinkhole occurred in the densely built-up area on the corner of Gerhard Street and Jean Avenue, in Centurion. In Fig.2 the spatial distribution of 1100 events that occurred during the last four decades in the area south of Pretoria (Oosthuizen and Richardson, 2011). The occurrence of this event was a motivation to extend the research on sinkhole prone areas identification for the Centurion region. The analysis was aimed at investigating the possible evidence of subtle movement related to the known sinkholes in the area.

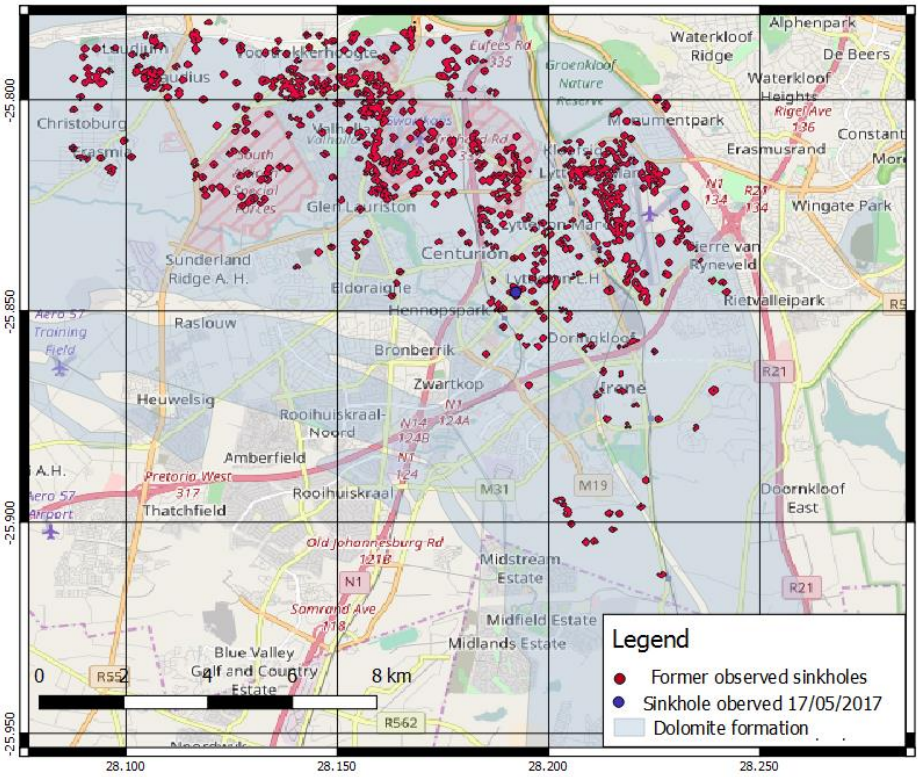

Figure 2-2: Distribution of sinkholes occurrences in the region of Centurion, CBD area since the early 1970s until mid-2012 (Oosthuizen and Richardson, 2011)

Ground movements were established based on Sentinel-1A images acquired from the European Space Agency (ESA). The images were acquired every 12 days from ascending and descending orbits. The interferometric wide swath mode cover was of 250 km. The medium resolution was at a range of 5 m to 20 m and azimuth direction (ESA, 2013). The vertical displacements were analysed for the period between May 2015 to May 2017. For this study 12 and 24 scenes have been acquired respectively from Sentinel-1satellite. The perpendicular baseline is given with respect to the master image acquired at 2007/04/18. The interferograms were generated using the software SNAP and SNAPHU (ESA, 2017).

2.5 Results

For the processed data, we observe a good number of PS objects generally uniformly distributed over the study area. The density of the PS was high mostly due to fact that study area was intensely built up. The total number of the processed points was 15370 (Fig. 3). PS displacement are measured along the satellite LOS, i.e. the sensor looking direction. The year displacement velocities, for the sensing period appear spatially homogeneous, decreasing with negative values (subsidence) to the N (Fig. 4).

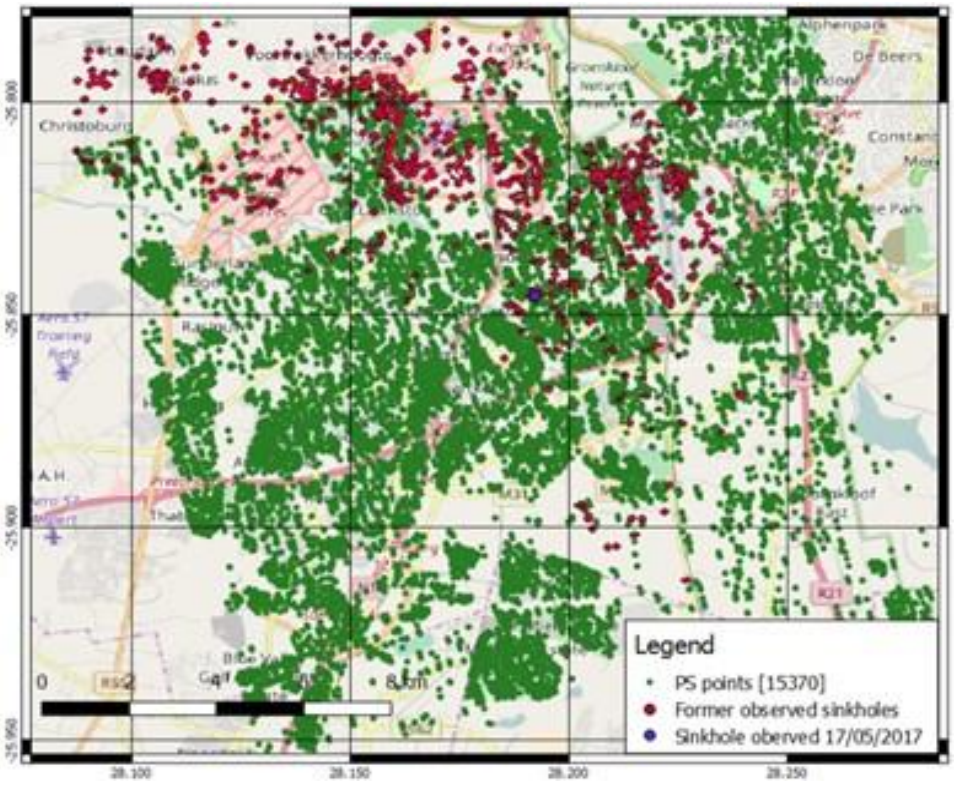

Figure 2-3: Coverage of the study area with PS point's overlaid on former observed sinkhole events

The range of the vertical displacement is of -5 to -12 mm/year. The PS to the centre and S of study area were subsiding up to -3 mm/year. The observed increase of subsidence close to the SW outskirts attributed to noise and processing artefacts.

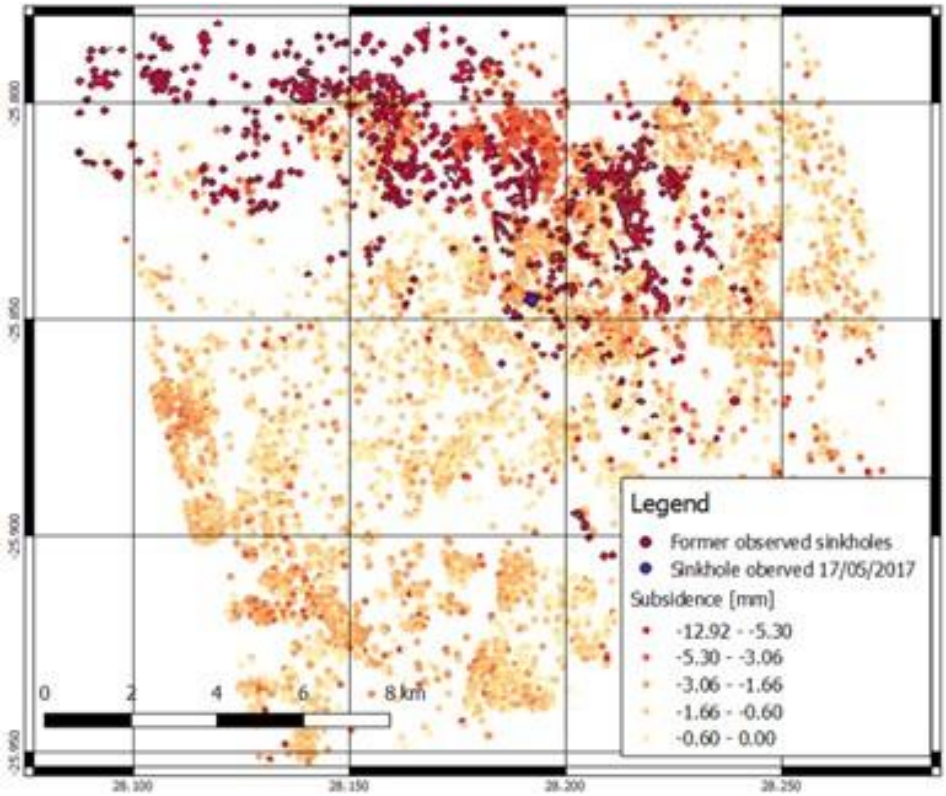

Figure 2-4: Yearly subsidence for the period May 2015 to May 2017

2.6 Discussion and Conclusions

The maximum subsidence velocity of -12 mm/year was observed to the N part of Centurion, which agrees to the high spatial density distribution of former sinkholes. The N of study area belongs to a high extend to the South Africa Spatial Forces. However, in the vicinity of sinkhole which occurred on corner of Jean and Gerhardt street (blue circle on Fig 5), no significant linear subsidence was observed. Theron (2017) and Intrieri et al. (2015) concur that in the case of sinkholes, deformation in the order of a few mm to cm are expected to occur days, months or even years before the failure. In general, measurable deformation has been observed before major displacement occurs, although the main limitation lies in the opportunity to observe such deformation. Latest observation of ground movement before sinkhole development revealed accelerating character of ground movements (Malinowska et al., 2017). PS technique assumes that observed ground displacement has a linear character. When the process becomes non-linear the values of the observed standard deviation is higher. The analysis of the spatial distribution of standard deviation led to the identification of a zone with standard deviation higher than -7 mm/year (Fig. 5), in the vicinity of the recent sinkhole event.

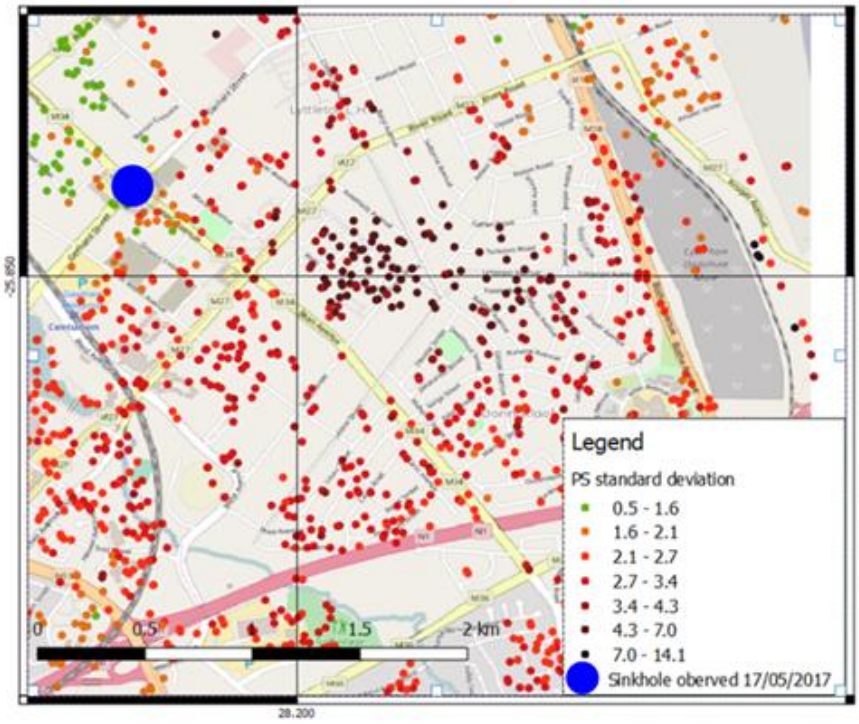

Figure 2-5: Standard deviation of PS points in the vicinity of the corner Jean and Gerhardt Street

Consistency of PS points distribution with high standard deviation was very high.

The PSInSAR analysis was carried out using ascending and descending SAR images from Sentinel-1 between May 2015 and May2017.The PSInSAR study for the temporal interval preceding sinkhole occurrence on the 17th of May 2017 shows subsiding and stable zones. Most of Centurion region seems to be relatively stable with an average displacement velocity of -1.6 mm/year. In the N of study area, the mean annual subsidence reached -12 mm/year.

The displacement in that area is linear and the standard deviation does not exceed -2.0 mm/year. Observed ground movement in the vicinity of sinkhole which occurred on the 17th of May 2017 is inferred that did not have linear character. Due to the known widespread presence of several sinkholes in the Centurion area, it is tempting to associate these localized,

isolated displacement time series with the precursory movements associated with the nearby, possibly undetected sinkhole.

Comparison between levelling mean velocities and PS mean vertical velocities is planned for comparison and validation of PSInSar measured displacement. Further measurements are planned in the N of the study area.

As demonstrated in the present study, SAR interferometry may represent an essential tool to detect displacement associated with sinkhole presence. Such studies can be used to influence the engineering design choices for the risk mitigation in urbanized areas characterized by the presence of soluble rocks.

2.7 References

Baer, G., Magen, Y., Nof, R. N., Raz, E., Lyakhovsky, V., Shalev, E. InSAR measurements and viscoelastic modelling of sinkhole precursory subsidence: Implications for sinkhole formation, early warning, and sediment properties. J of Geo. R. E. Sur., 123, 678-693, 2018.

Buttrick, D.B., Trollip, N.Y.G., Watermeyer, R.B., Pieterse, N.D., Gerber, A.G., 2011. A performance-based approach to dolomite risk management. Environ. Earth Sci. 1127-1138, 2011

Chang, L., Hanssen, R.F. Detection of cavity migration and sinkhole risk using radar interferometric time series, Rem. Sen. Env. 147(5), 56-64, doi: 10.1016/j.rse.2014.03.002, 2014

Colesanti, C.; Ferretti, A.; Prati, C.; Rocca, F. Monitoring landslides and tectonic motions with the Permanent Scatterers Technique. Engineering Geology 68, 3-14, 2003.

De Bruyn, I.A., Bell, F.G., 2001. The occurrence of sinkholes and subsidence depressions in the Far West Rand and Gauteng Province, South Africa and their engineering implications. Environ. Eng. Geosci. VII (3), 281e295.

Dippenaar, M., van Rooy, L., Diamond, R., Engineering, hydrogeological and vadose zone hydrological aspects of Proterozoic dolomites (South Africa), J. of African Earth Sciences 150, 511-521, 2019.

European Space Agency. Sentinel-1 User Handbook, September 2013: ESA User Guide; GMES-S1OP-EOPG-TN-13-0001; European Space Agency: Paris, France, 2013; p. 80.

Ferretti, A., A. Fumagalli, F. Novali, C. Prati, F. Rocca, and A. Rucci. A New Algorithm for Processing Interferometric Data-stacks: SqueeSAR. IEEE Transactions on Geoscience and Remote Sensing, Vol. 49, No. 9, 3460-3470, 2011.

Gutiérrez, F., Galve, J., Lucha, P., Bonachea, J., Jorda, Luis, Jordá, Rafael. Investigation of a large collapse sinkhole affecting a multi-storey building by means of geophysics and the trenching technique (Zaragoza city, NE Spain). Environmental Geology. 58. 1107-1122. 10.1007/s00254-008-1590-8, 2009.

Gutiérrez, F., Parise, M., De Waele, J., & Jourde, H. A review on natural and human-induced geohazards and impacts in karst. Earth Science Reviews, 138, 61-88. https://doi.org/10.1016/j.earscirev.2014.08.002, 2014

Intrieri, E., Gigli, G., Nocentini, M., Lombardi, L., Mugnai, F., Fidolini, F., Casagli, N. (2015), Sinkhole monitoring and early warning: An experimental and successful GB-InSAR application, Geomorphology, 241, 304-314, 2015

Malinowska, A., Witkowski, W., Hejmanowski, R., Chang, L., Hanssen, R., F., Van Leijen, F.J. Early detection of sinkholes applying persistent scattered interferometry (PSI). XVIII Mining workshop, 2017. Malinowska, A., Witkowski, W., Hejmanowski, R., Chang, L., Hanssen, R., F., Van Leijen, F.J. Sinkhole occurrence monitoring over shallow abandoned coal mines with satellite-based persistent scatterer interferometry. Engineering Geology, https://doi.org/10.1016/j.enggeo.2019.105336 (in press)

Nof, R., Abelson, M, Raz, E., Magen, Y., Atzori, S., Salvi, S., Baer, G., SAR Interferometry for Sinkhole Early Warning and Susceptibility Assessment along the Dead Sea, Israel, Remote Sens. 11, 89; doi:10.3390/rs11010089, 2019.

Oosthuizen, A.C., Richardson, S. Sinkholes and subsidence in South Africa. Council for Geoscience, 2011.

South African National Standard SANS 1936-1/2/3/4, 2012. Development of Dolomite Land. Edition 1 (ISBN 978-0-626-27840-3).

Rosen, PA; Hensley, S; Joughin, IR; Li, FK; Madsen, SR; Rodriguez, E; Goldstein, RM, Synthetic aperture Radar interferometry. Proc. IEEE., 88, 333-382, 2000.

Sowers, G. F. 1996. Building on sinkholes: Design and construction of foundations in karst terrain, ASCE, NY.

Theron, A.; Engelbrecht, J.; Kemp, J.; Kleynhans, W.; Turnbull, T. Detection of Sinkhole Precursors through SAR Interferometry: Radar and Geological Considerations. IEEE Geosci. Remote Sens. Lett. 14, 871-875, 2017

Vaccari, A.; Stuecheli, M.; Bruckno, B.; Hoppe, E.; Acton, S.T. Detection of geophysical features in InSAR point cloud data sets using spatiotemporal models. Int. J. Remote Sens. 34, 8215-8234, 2013

CHAPTER 3: SINKHOLE DEVELOPMENT STUDIES, THROUGH INSTRUMENTED SMALL SCALE PHYSICAL MODELS

3.1 Introduction

Over the last few decades, there has been an increase in sinkhole monitoring as well as researching the development of sinkholes. Although there has been progress, there is still an open area for research as there is a need for better sinkhole monitoring methods and an early-warning system development to reduce the risks associated with sinkhole development in areas underlain by dolomite.

Sinkholes suddenly manifest as holes in the ground with little to no warning and are usually circular. In South Africa sinkholes are caused by the weathering of dolomite due to poor surface-water drainage, the ingress of water from water-bearing services, and groundwater level drawdown. This problem has been occurring in numerous South-African provinces that are underlain by soluble carbonate rock such as dolomite. Sinkhole hazards have been a problem in Mpumalanga, Limpopo, North West, and various Cape Provinces, but none of these provinces has experienced as many sinkhole hazards as the Gauteng province which is approximately 25% underlain by soluble dolomite rock (Oosthuizen & Richardson, 2011).

Over the years, more problems on the Malmani Subgroup have been experienced due to the increase in residential and industrial development on sinkhole-prone areas (Wagener, 1985). According, to Schöning (1990) chert-rich formations are more susceptible to sinkhole formation (i.e. the Monte Christo and Eccles Formations). Furthermore, it was suggested that sinkhole events occurred more frequently on the Eccles Formation due to development taking place in the region and the Eccles formation being subjected to long wet periods due to leaking services and poor stormwater management (Schöning, 1996).

Sinkhole events have broadly manifested in areas such as the Far West Rand, Pretoria, and Centurion. These events resulted into casualties and fatalities, as well as property lost. The cost of repair of numerous structures and roads as was reported by Buttrick et al., 2001, was more than R1 billion.

In South Africa, sinkholes are usually investigated through direct methods such as coring, percussive drilling, and penetration testing. When the drilling method is applied, penetration rates are recorded per metre advance and samples are collected. The method of dynamic cone penetration testing, with a standard SPT hammer is used to determine the thickness of transported material in fault zones where no chert gravel is encountered. Furthermore, sinkholes are mapped through geophysical methods such as gravity surveys, seismic refraction, resistivity, electromagnetic and magnetometer surveys.

Sinkhole monitoring is crucial to predict and prevent sinkhole formation or to prevent further development on dolomitic land to reduced associated risk. Current sinkhole monitoring methods either need to be updated and supplemented by state-of-the-art technologies.

In recent years with the revolution of sensing and communication techniques, there are many possibilities to instrument structures, receive rich information to monitor, assess, and plan of existing infrastructure networks. During the last decade, fiber-optic sensing has become a widely accepted, mature technology, widely used in a range of applications. Collection and monitoring of more information is part of the big data trend, which is becoming increasingly important. Regular assessment can identify sinkhole formation susceptible areas. There is a growing interest from asset owners in more pervasive approaches that would allow more widespread monitoring of the ground hosting infrastructure (Smerthurst et al., 2017).

Installation of fiber optic sensor is proposed in urban environments to monitor strain and temperature variations along existing water service networks. There is a need to invest to

the implementation of early warning systems integrated smart, monitoring, could effectively monitor ground deformation, detect precursor phenomena, and support sinkhole hazard, risk mitigation, and enhance urban planning development.

Soga and Schooling (2016) remark that infrastructure monitoring is not new, yet recently sensor and communication research have been undergoing a revolution. There are currently possibilities to use these emerging technologies to distributed fibre optic sensors and wireless sensor networks to address need and look after the existing infrastructure, this obviously applies to sinkhole and subsidence phenomena.

3.2 Sinkhole formation mechanism

Jennings and Brink describe the mechanisms of sinkhole formation in detail they argue that sinkholes can form due to concentrated ingress of water or dewatering. Later in Oosthuizen and Richardson two scenarios represented in Figure 3-1 consider either ingress of water or lowering of water table level and the relevant behaviour of the wad. Wad or manganiferous earth, is an insoluble and slightly compressible material which is developed during the weathering of the dolomite and is encountered in small quantities in any cave into restricted zones within dolomite (Brink 1965).

Jennings was the first to describe the mechanism of sinkhole formation in detail, based on the multiple arch hypothesis. Jennings related the theory on simplified physical experiments with dry and moist sand, simulating sinkhole development conducted by Dr. Knight at the University of the Witwatersrand. The necessary conditions according to Jennings et al. (1965) are:

1. Abutments must be present to support the lateral pressure of the arched roof. The arched roof and its material must be of sufficient strength to support the loads acting upon it, otherwise, it will fail before it forms. Pinnacles must be present so that the arch roof can form. The span of the sinkhole must also be adequate to keep the forces acting on the arch in equilibrium for longer so that a larger cavity can be formed.
2. The arch must develop in the chemical residue called the residuum so that the vertical forces caused by the self-weight of the overlaying soil can be transferred to the arch (which counteracts the forces) and then transferred to the unyielding adjoining rocks (which counteracts the forces). Complete arching occurs when the vertical stresses along the inner curve of the arch are zero (Jennings et al., 1965). When the vertical stresses along the inner curve of the arch are not zero, then arching is still commencing.
3. A small or large void must develop below the arch in the chemical residue (residuum) (Jennings et al., 1965).
4. A reservoir filled with water must be present below the arch. This reservoir must be able to receive any material that falls from the roof of the arch so that the void can expand to a sufficient size. The soil from the roof must be transported using flowing water otherwise the cavity will not form. If the water does not flow the cavity be filled with overlaying soil as it falls from the top of the roof until no cavity is present.
5. A trigger that causes a disturbance and in turn causes the roof of the arch to collapse must be present once the cavity has expanded within the residuum to a sufficient size. The disturbance is usually in the form of water that infiltrates the arch causing it to lose its strength and then collapse or removing the interlocking material that gives the arch its strength and then causes it to collapse. The cavity will then propagate towards the surface. These conditions are dependent on each other, and if one

of these conditions do not occur then a sinkhole will not form according to Jennings et al., 1965. Later Brink opposed the described mechanism of sinkhole formation not supporting the multiple arch theory. He founded his opinion on extensive field evidence. He supported that lab experiments conducted while demonstrating very well the progressive "onion peel" collapse of successive arches, do not accurately simulate natural conditions. For example, sometimes in small sinkholes pinnacles are near the surface, the last arch is frequently trapped within the shallow ferricrete layer and does not break through to the surface. Finally, sinkholes are circular in plan, which is not following the pattern that multiple arches would produce interlinking circles in plan.

Brink expanded on the role of vertical tension fractures towards cavity development. Chert rich soil and chert slabs are permeable and are underlain by dolomite. He suggests that dolomite weathering takes place which forms interconnected cavities or chambers (due to the enlargement of flow paths as discussed in section 2.2) that are filled with water because the groundwater table is directly above the cavities or chambers. Vertical tension fractures reside in the residue soil above the cavities. They are widened into grooves (that can be clogged with overlaid residual chert soil) by a solution process caused by the surface water that percolates through the soil to reach the groundwater table (Brink 1979). The surface water (rain) percolates through the chert without eroding it. Vertical tension fractures can also be found at the bottom of the cavities or chambers which are widened into grooves by solution through phreatic waters.

Brink (1979), further argues that chert slabs settle in between the pinnacles and abutments. These pinnacles and abutments cannot be dissolved. The groundwater table lowers due to excessive groundwater pumping or droughts to a position below the horizontal cavities or champers. A source (like leaking pipes or excessive rainwater seepage) causes excessive water to be present which flows along the pinnacles to the slots. This causes the clogged slots to erode from the vicinity of the cavity upwards towards the ground surface by a process which is called headward piping which forms an arch in the residual soil that is attached to pinnacles (Brink 1979). The pinnacles support the overlaid soils self-weight through arching thrusts (Brink 1979). The arch then expands and propagates to the ground surface by erosion which is caused by surface water infiltration. The eroded soil from the arch falls into the cavity. The arch close to the surface which has a significant strength due to pebbled markers or cohesion provided by vegetation remains stable until a trigger causes the arch to fail (Brink 1979).

Brink concludes that in some cases the arch above the cavity fails even before a final arch close to the ground surface can form. This happens because the base of the arch receives moisture from the percolating water, and this decreases its shear strength and causes it to fail under the soils self-weight (Brink 1979). The small bottleneck sinkhole is then completely formed but can expand due to the formation of tension cracks that form around the collapsed arch which causes the soil around it to collapse further, resulting in a large circular sinkhole (Brink 1979).

3.3 Sinkhole formation scenarios

Sinkhole formation due to ingress of water:

1. There are cavities present in the bedrock and the overlaying soils (Oosthuizen & Richardson, 2011). These cavities are in counterpoise (Oosthuizen & Richardson, 2011).

2. Constant ingress of water causes erosion of the ground surface of the soil and this causes the overlaying soil to travel downwards into the cavities (Oosthuizen & Richardson, 2011).
3. The strength and mass of the soil at the surface decreases as the overlaying soil fall into the cavity (Oosthuizen & Richardson, 2011). This process will continue upwards in the form of an arch until the soil that is left in the arch ultimately fails and falls into the cavity as the underlying soil did (Oosthuizen & Richardson, 2011). The arch's strength is usually decreased by a trigger until it fails (Oosthuizen & Richardson, 2011).
4. A sinkhole will, therefore, be formed usually with a small diameter at the surface and the larger diameter at the bedrock (Oosthuizen & Richardson, 2011).

Sinkhole formation due to the lowering of the groundwater table:

1. There are cavities present in the bedrock. Overlaying soils are filled with groundwater and are in counterpoise (Oosthuizen & Richardson, 2011). The water in the cavities gives buoyant support and decreases the rate of erosion of the ground surface (Oosthuizen & Richardson, 2011).
2. The groundwater table lowers filling the cavities with air (Oosthuizen & Richardson, 2011). This causes a force imbalance because buoyancy force no longer exists to supporting the overlaying soil.
3. Constant ingress of water causes erosion of the ground surface of the soil and this causes the overlaying soil to travel downwards towards the cavities (Oosthuizen & Richardson, 2011).
4. The soil at the surface strength and mass decreases as the overlaying soil falls into the cavity (Oosthuizen & Richardson, 2011). This process will continue upwards in the form of an arch until the soil that is left in the arch ultimately fails and falls into the cavity as the underlying soil did (Oosthuizen & Richardson, 2011). The arch's strength is usually decreased by a trigger until it fails (Oosthuizen & Richardson, 2011).
5. The sinkhole will therefore be formed usually with a small diameter at the surface and the larger diameter at the bedrock (Oosthuizen & Richardson, 2011).

The fluctuation of the groundwater table influences the rate of sinkhole formation and induces triggers which cause sinkhole collapse (Lei, Jiang & Yu, 2002). If the groundwater table does not fluctuate then drainage of the dissolution soil cannot take place. Drainage will then not be a trigger mechanism that instigates sinkhole collapse. When the groundwater table descends the sinkhole will form rapidly (Lei, Jiang & Yu, 2002). This also causes negative pressure in the cavity which will increase the seepage deformation rate of the overlaying soil (Lei, Jiang & Yu, 2002). Consolidation takes place in the soils being drained as the water table lowers (Brink 1979). This consolidation increases the consolidated soils shear strength and gives the soil a greater resistance to erosion (Brink 1979). These factors will then, in turn, result in a resistance against sinkhole formation.

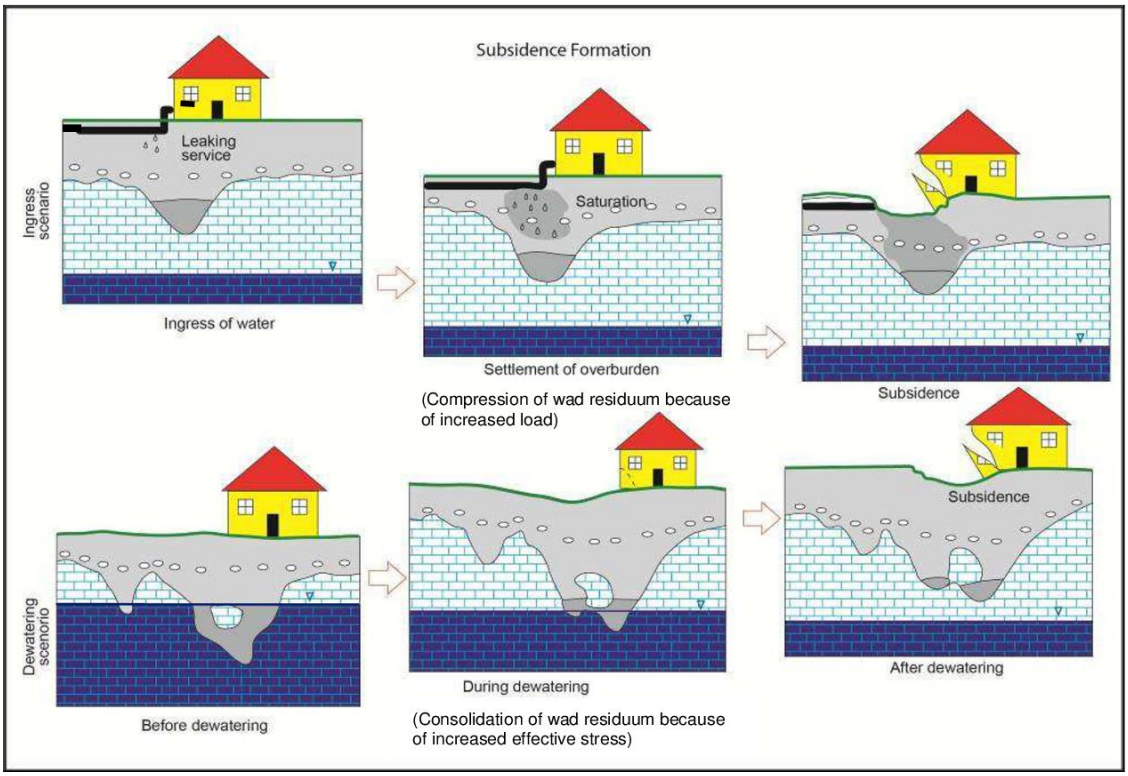

Figure 3-1: Two sinkhole formation scenarios (Oosthuizen & Richardson, 2011)

3.4 Type of sinkholes

There are two main genetic groups of sinkholes, according to Gutiérrez et al. (2008). The first group of sinkholes are called solution sinkholes and they are formed when soil dissolves to a liquid, due to specific conditions being met within the soil causing it to dissolve (Gutiérrez et al., 2008). Soil is made up of different molecules and the soil dissolves when the bonds that hold the molecules together breaks. The liquid evaporates when it is exposed to the surface or the liquid gets drained away during the rise and fall of the water table (Gutiérrez et al., 2008). The overlaying soil has no support and the soil begins to lower under its own weight and gravitational movements causing the cavity to be filled with the overlaying soil (Gutiérrez et al., 2008). Gravitational movements that the overlaying soil experiences includes internal erosion and deformation (Gutiérrez et al., 2008). These group of sinkholes are shallow, but they can have a large diameter (Gutiérrez et al., 2008).

The second group of sinkholes are called caprock collapse sinkholes or bedrock collapse sinkholes and they are formed when soil dissolves to a liquid, because specific conditions are met within the soil causing it to dissolve (Gutiérrez et al., 2008). The liquid evaporates when it is exposed to the surface or the liquid gets drained away during the rise and fall of the water table and that exposes a cavity in the ground that was previously filled with soil/liquid (Gutiérrez et al., 2008). The overlaying soil has no support and collapses into the cavity, but no bending of the soil occurs before the roof of the sinkhole collapses (Gutiérrez et al., 2008). The roof of the sinkhole ultimately fails. These sinkholes form deep underneath the earth's surface, can reach deep depths in the earth's crust and may even reach into the earth's upper mantel with their breccia pipes and have relatively small diameters (Gutiérrez et al., 2008). Sinkholes that are formed due to interstratal dissolution of the bedrock that is composed of an evaporitic rock and causes the roof of the sinkhole to bend gradually under its own weight

and gravity (when the liquid in the cavity is gone), are called bedrock bending or caprock bending sinkholes. These sinkholes are also part of group two and stretch deep into the earth's upper mantel in a vertical direction, but do not span over great areas and have small diameters (Gutiérrez et al., 2008).

Furthermore, sinkholes can be classified into six main types namely solution, collapse, caprock, dropout, suffusion and buried as shown in Figure 3-2.

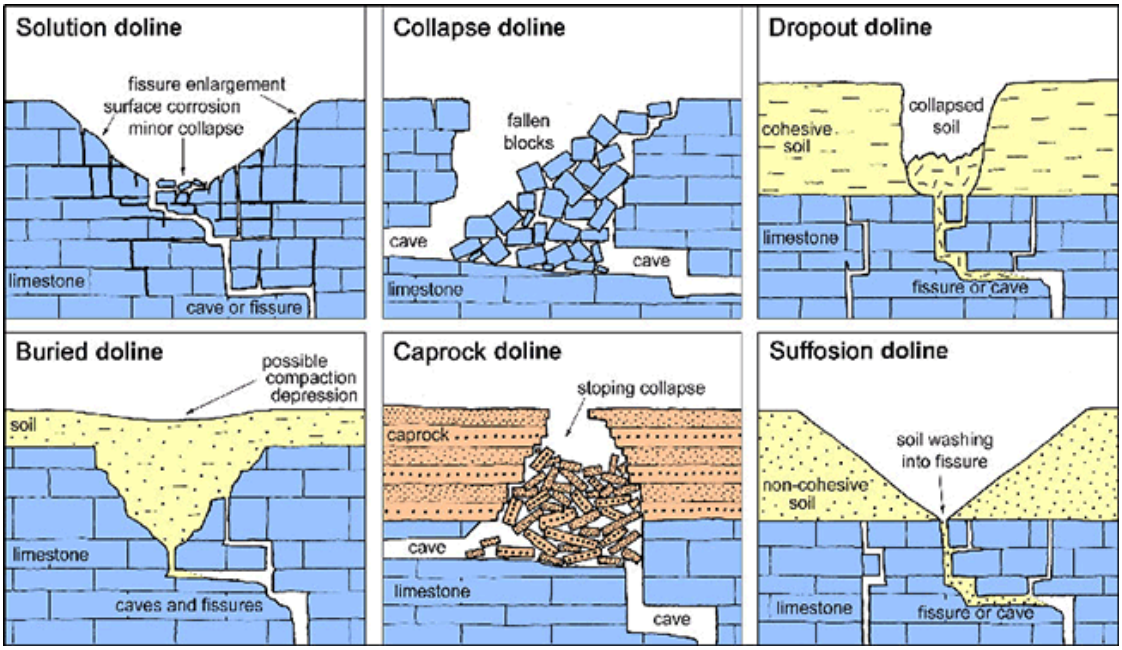

Figure 3-2: Different types of sinkholes (Waltham, Bell & Culshaw, 2005)

Solution sinkholes are formed by the dissolution of soluble rocks which causes the lowering of the ground surface (Waltham, Bell & Culshaw, 2005). Soluble rock types in which these sinkholes form are dolomite, limestone, gypsum and salt (Waltham, Bell & Culshaw, 2005). The formation speed of these sinkholes is slow and can be up to 20 000 years long (Waltham, Bell & Culshaw, 2005). These landforms are regarded as stable due to their slow formation speed, are enormous with diameters up to 1000 metres and can reach depths of up to 100 metres deep (Waltham, Bell & Culshaw, 2005). These sinkholes have a fissure that contains water that transports the solution of the soil from the sinkhole (Waltham, Bell & Culshaw, 2005).

Collapse sinkholes are formed when the rock roof fails and falls into the underlying cavity (Waltham, Bell & Culshaw, 2005). Rock types in which these sinkholes form are dolomite, limestone, gypsum and basalt (Waltham, Bell & Culshaw, 2005). The formation speed of these sinkholes is slow, but the failure event happens at a rapid pace (Waltham, Bell & Culshaw, 2005). These sinkholes are very rare, can have a diameter up to 300 metres and can reach depths of up to 100 metres deep (Waltham, Bell & Culshaw, 2005). An unstable roof spans the cave of these sinkholes.

Caprock sinkholes are formed when an insoluble rock roof fails and collapses into a cave that was formed from the dissolution of soluble rocks such as dolomite, limestone and gypsum (Waltham, Bell & Culshaw, 2005). The formation speed of these sinkholes is slow and can be as long as 10 000 years (Waltham, Bell & Culshaw, 2005). These sinkholes are rare, can have a diameter up to 300 metres and can reach depths of up to 100 metres deep (Waltham, Bell & Culshaw, 2005).

Dropout sinkholes are formed when overlaying soil falls into a void that was formed over a bedrock fissure (Waltham, Bell & Culshaw, 2005). These sinkholes form in areas where cohesive soil overlies limestone, dolomite or gypsum (Waltham, Bell & Culshaw, 2005). The formation speed of the voids is very slow, but the dropout of these sinkholes occur rapidly after a trigger causes the arch of these sinkholes to collapse. These sinkholes can have a diameter up to 50 metres and can reach depths of up to 10 metres deep (Waltham, Bell & Culshaw, 2005).

Suffusion sinkholes form when soil is washed into fissures in a bedrock (Waltham, Bell & Culshaw, 2005). These sinkholes form in areas where non-cohesive soil overlies limestone, dolomite or gypsum with a slow formation speed. It takes years for the overlaying soil to fall into the fissure (Waltham, Bell & Culshaw, 2005). These sinkholes are very destructive, can have a diameter up to 50 metres and can reach depths of up to 10 metres deep (Waltham, Bell & Culshaw, 2005).

Buried sinkholes form when an existing sinkhole is filled with soil due to changes in the environment (Waltham, Bell & Culshaw, 2005). These sinkholes can be recognized by a depression in the surface, are stable geological landforms with a slow formation speed up to 10 000 years long, a diameter up to 300 metres and can reach depths of up to 100 metres deep (Waltham, Bell & Culshaw, 2005).

It is important to identify a sinkhole before the roof or the soil above the sinkhole fails so that structural damage and injuries can be kept to a minimum. There are various methods for identifying a possible sinkhole. Some of these methods are seismic, geo-electrics, and geo-radar (Thornbush, 2017). In this experiment the strain which results from ground displacement caused by sinkhole collapse is measured. These measurements will help identify the sinkhole mechanisms as well as the strain distribution within the soil as the sinkhole forms. Technology is available that can be used for large or microscopical strain measurements (Iten, 2011).

3.5 Introduction to fibre optic sensing and sinkhole monitoring

Various methods have been used to monitor sinkhole formation in the past. Margiotta et al. (2016) made use of Electrical Resistivity Tomography (ERT), Ground Penetrating Radar (GPR), and Seismic Reflection (SR). These methods have been proven to be useful and could detect the location of unknown sinkholes. Although ERT, GPR, and SR have successfully been used by many researchers to detect sinkholes it has been found that these methods are only useful to map shallow subsurface cavities (Carbonel et al., 2014).

Other methods of monitoring already-formed sinkholes include the use of Geographic Positioning Systems (GPS), laser scanners, as well as total stations (Oldow et al., 2008; Kent & Dunaway, 2013). Nanoseismicity has also been proven to be very useful as an early warning system when it was used to forecast sinkhole collapse in the Dead Sea coast years in advance (Abelson et al., 2018). It must be noted that InSAR has successfully been used to monitor sinkholes and it was found feasible to be used as an early warning system (Intrieri et al., 2015). Optic fibre technology has also been used to monitor the health of structures and landslides, but there is limited literature on its use to monitor sinkholes and act as an early-warning system.

Optic fibre sensors (OFS) have been developed to have numerous applications in the engineering and non-engineering environment. These OFS have proven to be very useful in measuring strain in various soil profiles which could act as an early warning sign for slope failure since the OFS together with effective systems of timely data transfer are very accurate.

OFS can easily monitor the health of embankments, tunnels, dams, mines, boreholes, and the seafloor and its importance to monitor structural health have been emphasised by Soga & Schooling (2016). Combining the OFS with small-scale physical models it has been proven by many researchers (Kapogianni et al., 2016; Picarelli et al., 2015; Zhu et al., 2014) that can

successfully be used to detect and possibly monitor ground movement. This property of the OFS could, however, also be exploited to monitor sinkhole formation.

Ultimately, the OFS will aid in measuring sinkhole formation in sinkhole-prone areas and may provide information that can be used by urban planners as well as for prevention. The technology, however, may produce false alarms (Intrieri et al., 2015) as not every subsidence leads to a sinkhole and there might also be instrumental noise.

3.6 Optic fibre sensors

Optic fibre sensors have been proven to be able to evaluate the safety of man-made structures such as bridges, dams, high-rise buildings, and regions prone to bedrock collapse, which is the case in dolomitic areas (Shinoda et al., 2006). Health monitoring systems using Fibre Bragg Gratings (FBG's) makes it possible to detect strains and temperatures.

The optic fibre sensor technology enables long-term monitoring of deforming areas and hopefully, in time, it will be possible to use this technology to predict the propagation of ground deformation in critical areas such as roads in the Tshwane or other susceptible areas such as Tembisa, Vosloorus, Laudium, Thokoza, and Centurion, and therefore prevent injury and damage to infrastructure. This methodology could be a useful tool, for town-planners decision maker, to use the data obtained and inform an early warning system.

Fibers could be buried longitudinally, and thus cover long distances, yet there is limitation related to the high cost, of the interrogator equipment. Although optical fiber sensors are widespread in structural health monitoring, their use in geotechnical engineering is limited. The performance of Time Domain Reflectometry (TDR) and Brillouin Optical Time Domain Reflectometry (BOTDR) for sinkhole monitoring has been barely explored (Lanticq et al., 2009; O'Connor and Trainum, 2015; Jiang et al., 2015). These novel techniques may provide subsidence measurements along long lines (e.g. communication infrastructure) but may be adversely affected by temperature changes, vibrations, and processes non-related to sinkhole activity.

Lanticq et al., 2008 performed sinkhole detection using both B-OTDR and OFDR techniques with two different optical fibers of the same sensing cable embedded in the soil. The main limitation of such a warning system is that it cannot distinguish a large and distant cavity from a smaller and closer one, unless a network of sensing cables is deployed. Yet further field test, are required to validate the results.

O'Connor and Trainum (2015) presented an alternative approach to monitor ground deformation of US 18 in Gordo County, Iowa, by removing the existing pavement, installing coaxial cables, in excavated trenches, replacing the pavement with double reinforced, and subsequent monitoring the cables using Time Domain Reflectometry (TDR). The cables were interrogated several times a day and data were transmitted via cellular modem to Iowa DOT facilities. Although activity has been detected in each of the eight coaxial cables, there was no definitive correlation between TDR activity locations, sinkhole locations, or geophysical anomaly locations.

Jiang et al. (2016) used an experimental study of monitoring the process of sinkhole collapse using BOTDR. In a series of tests of an experimental model, sinkholes are induced by pumping simulated karst water. Real time strains of optical fibers buried in sediments and soil damages were measured. Results of the experimental study demonstrate that positions of peak strain in optical fibers correspond well to areas of maximum disturbance and soil void formation. Changes of optical fiber strains in different soil layers are good indicators of vertical disturbance in soil. This technology could potentially become a useful tool to monitor and predict sinkhole collapse and subsidence, especially along linear infrastructure such as roads,

highways and railways. In practice, optical fibers need to be buried as deep as possible or more carefully to avoid sliding movement of optical fibers.

The main objective of this study is to detect and monitor strains in reduced scale sinkhole induce models using optic fibre sensor technology. The mechanism of sinkhole formation was, therefore, investigated through several normal gravity tests in a controlled laboratory to supplement current knowledge of real-life strains experienced in dolomitic terrains.

These experiments also explore the possibility of optic fibre sensor technology (FBGs) being used as an early-warning system. Furthermore, this study promotes the integrated science of geotechnical engineering and photonics.

The adopted methods aim to experimentally investigate sinkhole formation through scaled model development using laws of similitude to obtain the magnitude of the strains one can expect to see as sinkholes of sizes form. Thus, numerous reduced scale tests were carried out in a laboratory environment to quantify the strain experienced in various locations within a soil profile where a sinkhole or void would form. The strain was measured through FBGs and an optical interrogator under normal gravity.

Data were captured by an HBM Braggmeter FS22SI. The interrogator captured wavelength data every second from the start of the sinkhole event and would save data until the end of the test in one-minute text files. The data from the text files were then be analyzed using Microsoft Excel.

A scale of 1:30 was chosen to simulate a medium-sized sinkhole classified according to South African National Standard (SANS), 2012. A balloon was filled with 440 ml of water for each 1-g test to ensure that the “void” or balloon would be the same size in each test. The sinkhole widths and depths in the model were measured using a digital Vernier caliper for each test.

3.7 Principles of Optical sensing

In fiber optic technology, fiber (cables) transmits, continuously modulated analogue streams of light, or a series of digital pulses from one point to another along the optic fiber. A side view of typical single-mode optic fiber is shown in Figure 3-3. Cladding material with higher refraction index keeps the propagating light pulse inside the glass core. The buffer coating and the jacket are used to resist external or internal interferences and for the protection of the glass core (Iten, 2011).

The pulses are generated to specific characteristics by an optical spectrum analyser. Once a pulse has propagated through optic fiber, it is a fed into an interrogator or optical spectrum analyser (Othonos, 2000). The pulse is then analysed by the device, to determine any attenuation or change in wavelength (which may have resulted from scattering during the pulse’s propagation). The popularity of fiber optic sensing techniques has risen due to several advantages it has over conventional sensing techniques. These are immunity to electromagnetic interference, immunity to power fluctuation along the optical path, insensitivity to corrosion and fatigue, high precision and durability, and reduced size and cable requirement.

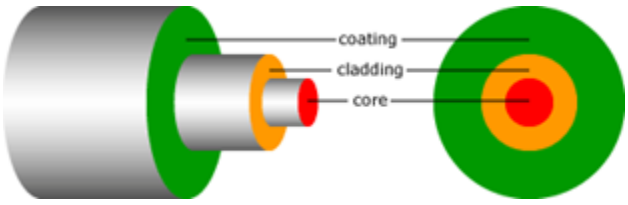

Figure 3-3: Optic fibre structure

The light travelling within the fibre optic medium is emitted at a specific frequency by a laser. As strain is formed movement within the observed structure, the fibre optic medium will move and bend in the direction of the movement. This causes bends within the fibre optic medium which cause a phase shift of the light travelling through the medium where some of the light will undergo backscattering (Linker & Klar, 2017) as some of the light shoots back (called backscattering) in the direction of the light source. The backscattering of the light allows for the detection of the location where movement is experienced and from that the strain can be determined. The FBG sensors attached to the fibre optic medium enables one to obtain the strain data which is interpreted by a Yokogawa AQ6317C optical spectrum analyser (OSA).

There are various optical fibres which include multimode optical fibres and single-mode optical fibres. Multimode optical fibres can propagate light within the optical fibre core at various angles since it has a big core and therefore is more often used for shorter distance transmissions. Singlemode optical fibres have a much smaller core and therefore light can only travel through the core once which leads to the single-mode fibre having a lower attenuation and can be used over longer distances (Udd & Spillman Jr., 2011).

OFS have various applications within the engineering industry and have successfully been used to monitor pipeline response due to tunnelling (Vorster et al., 2006), monitoring seismic activity (Teisseyre et al., 2006), monitoring a landslide location in Japan (Higuchi et al., 2007), to estimate sinkhole-induced ground movements (Buchoud et al., 2016), and to investigate structures using fibre optic sensors (Arzu et al., 2015; Kapogianni et al., 2016a; Huang et al., 2018).

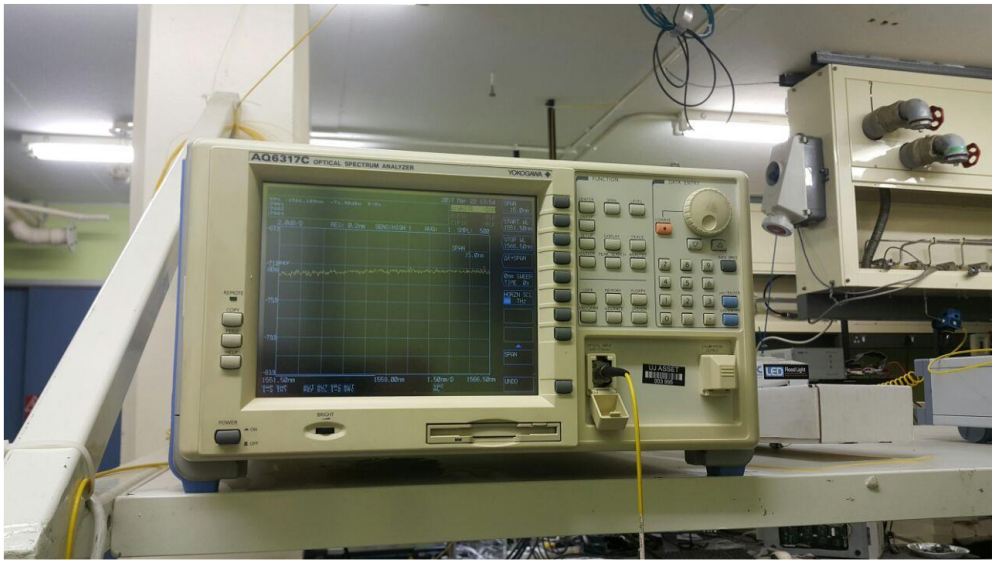

Figure 3-4: An AQ6371C Optical Spectrum Analyser used to analyse FBGs

Although the use of optic fibre sensors is not new technology, its use within the geotechnical community is a relatively new concept which competes well with current monitoring techniques since the optical fibre sensors are small, can survive chemically aggressive environments, is immune to electromagnetic interference, and many different sensors can be multiplexed into one optical fibre (Chtcherbakov, 1997). Optical fibre sensing techniques are therefore ideal to be used in instability prone areas since current measurement techniques such as strain gauges and the vibrating wire sensors have the disadvantages of being vulnerable to electromagnetic interference, poor stability, and poor durability (Wang et al., 2008)

Optic fibre sensor monitoring systems can act as real-time early-warning systems as well as long-term monitoring systems and can accurately predict strain differences at various locations along an optic fibre cable (Picarelli et al., 2015). Thus, the basic location of strain changes within geotechnical structures can be continuously monitored and the resultant strain measurements can be used to predict failure or identify localized failure zones.

According to Jewett & Serway (2010) total internal reflection occurs when light is directed from a medium having a given index of refraction towards one having a lower index of refraction. Considering Figure 3-5a, light travels through medium 1 towards medium 2. Medium 1 has an index of refraction of n1 and medium 2 has an index of refraction of n2. Medium 1 has a greater index of refraction than medium 2 thus n1 > n2 and therefore the reflected light is bent away from the normal. The angle at which the light transmits from medium 1 to medium 2 is termed the angle of incidence, θ_i. At a particular angle, the light ray will not travel from medium 1 to medium 2, but rather the light ray will remain within medium 1 (depicted in Figure 3-5b) – this angle is termed the critical angle, θ_c. In that case, all light rays will be reflected into medium 1 for angles bigger than θ_c (depicted in Figure 3-5c).

Snell's law of refraction is described by the equation.

$n1\sin\theta_1 = n2\sin\theta_2$ (1)

and it can be used to find the critical angle. Therefore, $\theta_1 = \theta_c$, $\theta_2 = 90^o$ and Equation 1 gives the critical angle for total internal reflection

$$n_1 * \sin\theta_c = n_2 * \sin 90^o = n_2 \quad (2)$$

$$\sin\theta_c = n2 * n1 \text{ (for n1 > n2)} \quad (3)$$

In optic fibre, the glass core (n1) has a greater refractive index than the cladding (n2) thereby satisfying the conditions needed for total internal reflection. Therefore, light cannot escape medium 1 and the light will keep on reflecting within the medium as shown in Figure 7 – this is how light is reflected within an optic fibre core.

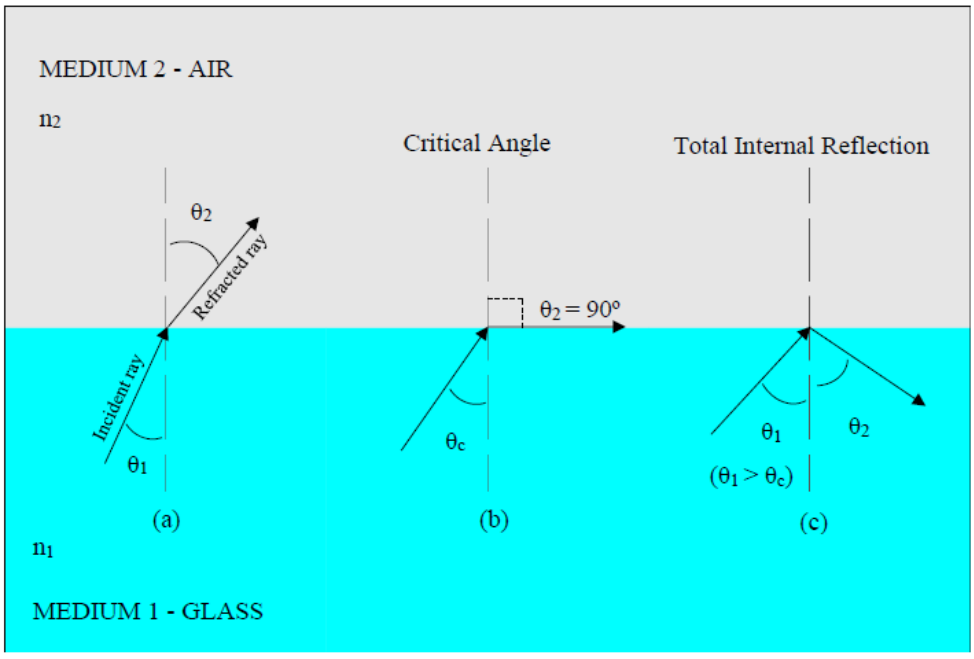

Figure 3-5: A depiction of how Total internal Reflection occurs within a medium

3.8 Fibre Bragg Grating sensors

A fibre Bragg grating (FBG), depicted in Figure 3-6 and Figure -7 consists of a single-mode optical fibre that has undergone a periodical modulation of the refractive index of the core of the optical fibre. Figure 3-11, it shows how the optic fibre core modulation takes place by exposing the fibre core and irradiating it with ultraviolet (UV) light at localised positions (Huang et al., 2018). The diffraction pattern on the optic fibre is created by transmitting the UV light beam through a special transmission diffraction grating which has the diffraction pattern precisely etched into it. This diffraction grating is termed a "phase mask" and is used to photo imprint a refractive index modulation (FBG) into the optic fibre core (Mihailov, 2012). The light which is guided down the core of the optical fibre (as depicted in Figure 3-6) will be scattered by each grating plane (the black bands depicted in Figure 3-6). If the wavelength of the light does not match that of which the grating was inscribed into the core, then the reflected light will progressively become more out of phase which will eventually cancel out (Grattan & Meggitt, 1995). If the wavelength of the grating matches that of the light, then the reflected light will add constructively from each grating plane and will eventually form a back-reflected peak (Grattan & Meggitt, 1995; Zheng et al., 2018). Therefore, the FBG reflects only a certain wavelength towards the source of the light (Huang et al., 2018) and this phenomenon is depicted in Figure 3-6 where the reflected light from the FBG forms a peak at a particular wavelength (Figure 3-9).

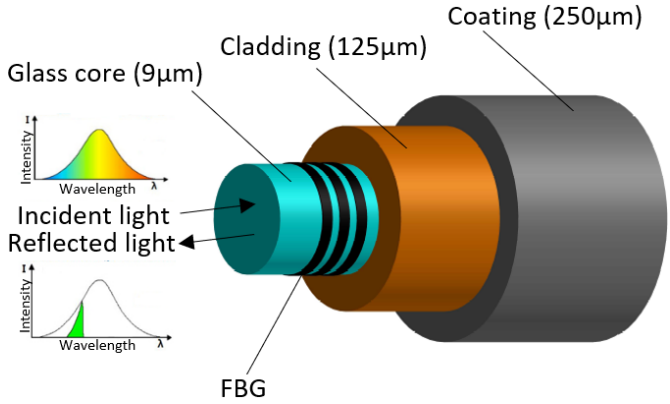

Figure 3-6: Fibre bragg grating (FBG) reflects a certain light wavelength

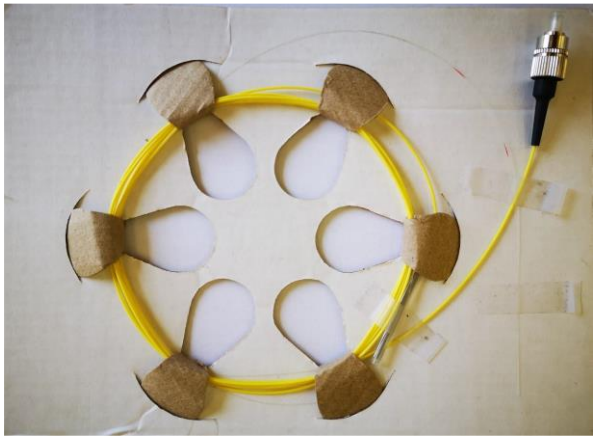

Figure 3-7: Optic fibre displaying the connector, a splice, and a bare FBG between the red markers

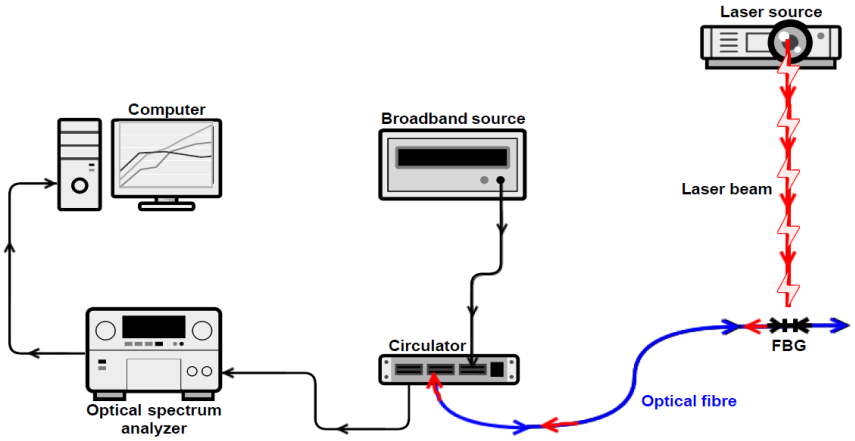

Figure 3-8: Fibre core periodically modulated through UV light and a phase

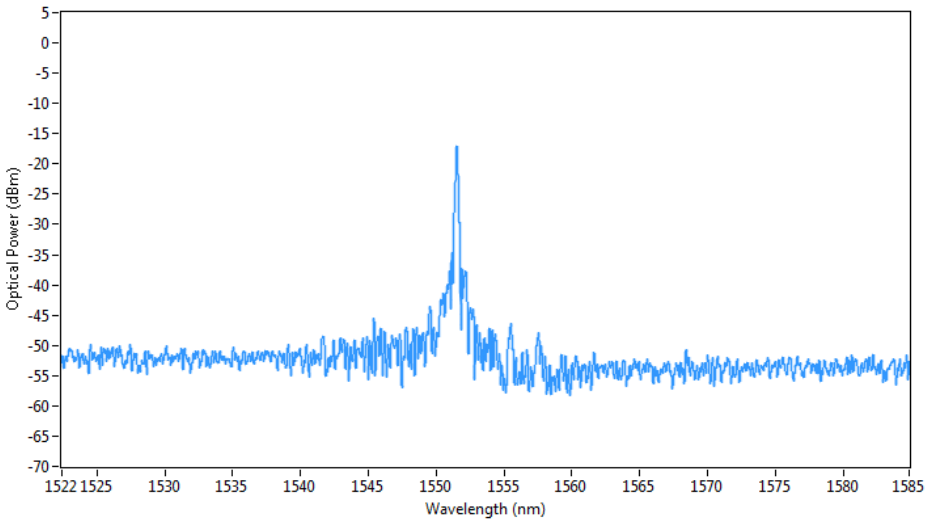

Figure 3-9: A typical example of the wavelength of the light reflected by a 1552nm FBG using an optical interrogator

The photosensitivity of optical fibers allows for the formation of phase structures within its core, called gratings (Othonos, 2000). The operational principles of fiber Bragg gratings (FBGs) is based on the presence of these gratings within the optical fiber which are created as a series of density alterations positioned periodically along the optical fiber glass core (Iten, 2011). The principle of operation is based on Bragg's law.

According to Bragg's law, a portion of light travelling through the optic fiber, with a specific wavelength, is reflected when it passes a Bragg grating. The value of this specific wavelength at which a light ray is reflected, is called Bragg wavelength. This value is dependent on the distribution of the Bragg gratings along the optic fiber (grating period) as well as the refractive index of optic fiber All the other light rays with different wavelengths pass the Bragg grating undisturbed. The light ray that is reflected provides information for potential strain changes, Figure 3-3. This is because the Bragg grating period is dependent on the strain in the specimen being monitored (Iten, 2011). The FBG wave-length change is sensitive to tensile and compression stress and temperature. The relationship between the refractive index$n_e$of the fiber's core, grating period Λ and Bragg wavelength λ_B is expressed mathematically following Eq. (4):

$$\lambda_B = 2n_e\Lambda \quad (4)$$

where n_e is the effective refractive index of the grating in the fiber core and $\Lambda$is the grating period. An FBG is sensitive to elongation and temperature, following Eq. (5):

$$\frac{\Delta\lambda_B}{\lambda_B} = (1 - p_e)\varepsilon + (\alpha_\Lambda - a_n)\Delta T \quad (5)$$

where $\Delta\lambda_B$ is the shift of the reflected wavelength $= (\lambda'_B - \lambda_B), p_e$ is the photoelastic coefficient, a_Λ is the thermal coefficient, and a_n is the thermal modulation of the core refractive index? The shift of reflected wavelength has a linear relationship with the axial strain ε and the change of temperature ΔT. Temperature sensors are usually embedded to detect temperature variations in the specimen being monitored. Temperature variations are usually not observed for short term physical model tests.

3.9 FBG fabrication methods

There are currently two major methods to manufacture FBGs – holographic and non-holographic. Firstly, the holographic interferometer method makes use of interference from UV beams to photo imprint a refractive index modulation into an optical fibre (Meltz et al., 1989). Secondly, the non-holographic method termed the "phase mask method" utilizes silica glass (a phase mask) with a specific period grating to photo imprint a refractive index modulation into the glass core of the optic fibre (Hill et al., 1993). Both methods are described in more detail below.

Holographic interferometer technique: For this setup, the laser beams operate in the UV region and are crossed, as depicted in Figure 3-10 to produce an interference pattern which is etched into the core of the optic fibre (Udd & Spillman Jr., 2011). Dark regions in the interference pattern will not affect the refractive index of the optic fibre core while lighter regions increase the refractive index of the optic fibre core.

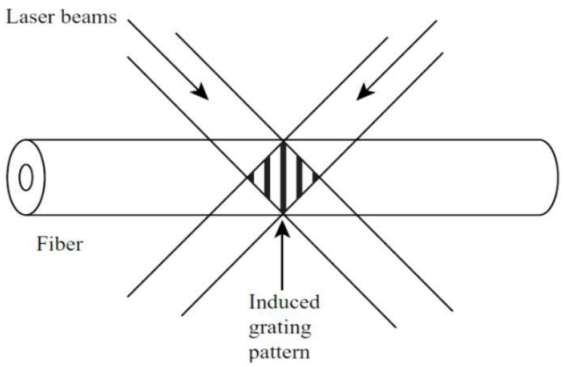

Figure 3-10: Depiction of how FBGs are manufactured using the phase mask method (Udd & Spillman, 2011)

Phase mask method: For this non-holographic method, a single UV beam passes through a quartz phase mask, depicted in Figure 3-11, which has a distinct diffraction pattern engraved into it. The diffraction pattern of the phase mask is directly photo imprinted onto the core of the optic fibre to induce a refractive index modulation (termed a "grating pattern") of the core (Udd & Spillman Jr., 2011).

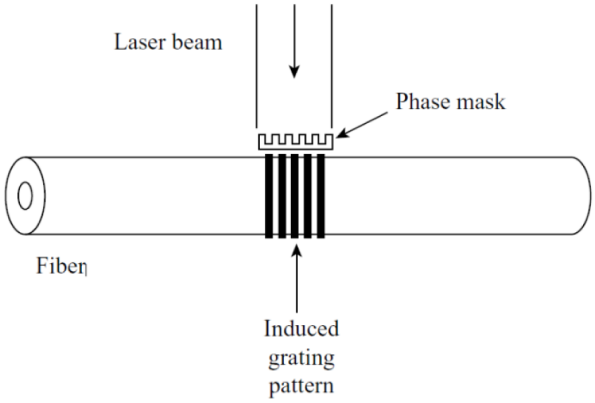

Figure 3-11: Depiction of how FBGs are manufactured using the phase mask method (taken from Udd & Spillman, 2011)

3.10 FBG Strain Calibration

The strain FBGs were calibrated by keeping temperature constant and straining a representative FBG by means of stretching the FBG on a clamp and stepper-motor system. This was done to determine the strain calibration coefficient for the FBGs that were used throughout all the tests. Therefore, the results can be found in Figure 3-12 below. By knowing that the temperature has been kept constant and the temperature change, therefore, being zero, Equation 5 can be rewritten as $\Delta\lambda B/\Lambda\beta = \beta\varepsilon$ using calibration results presented in Figure 3-12, it can be deducted that the strain calibration coefficient/strain sensitivity was found to be:
$\beta = 1856.7/1550.6 = 1.2\pi\mu/$

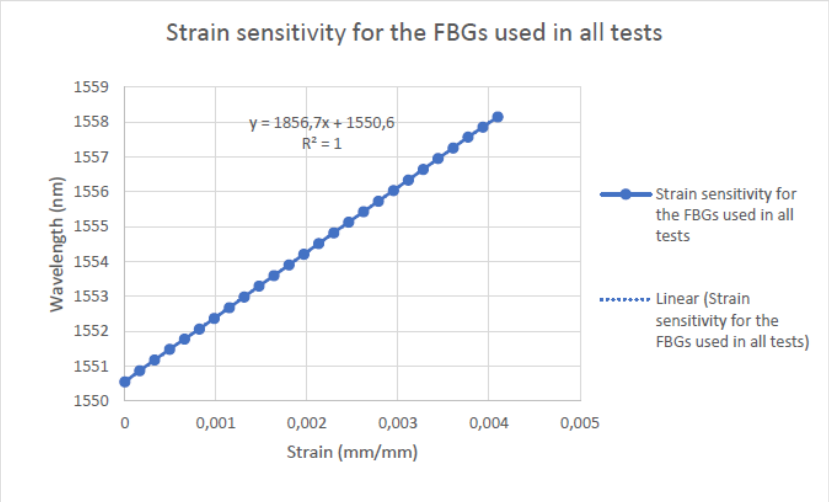

Figure 3-12: Strain calibration results for the FBGs used in the sinkhole modelling test.

The temperature FBGs were calibrated by submerging an FBG into hot water and measuring the respective wavelength as the water cooled down. The calibration graph can be found below in Figure 3-13. The temperature sensitivity was determined to be 9.54 pm/ºC.

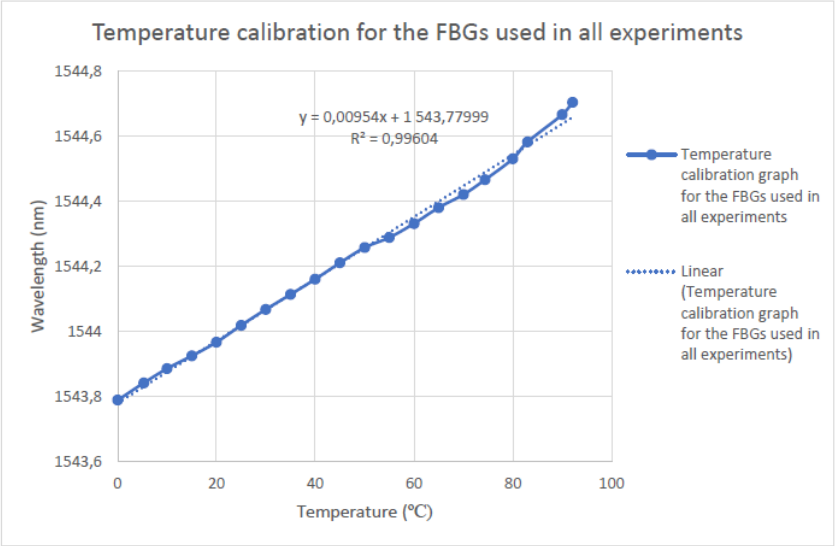

Figure 3-13: Temperature calibration results for the FBGs used in the sinkhole modelling tests

The FBGs designed and manufactured in the Photonics Laboratory at the University of Johannesburg allowed for strain and temperature measurements to be taken at various depths within the various soil profiles of the various tests. All sensors were manufactured in photosensitive optic fibre using the phase mask technique.

The FBGs were manufactured using an Nd:YAG laser using the 266 nm wavelength. All FBGs were manufactured to reflect a wavelength in the range of 1540 nm to 1555 nm and the calibrations were done by illuminating the sensors with a super-luminescent diode and measuring the response with the OSA, Figure 3-14 and Figure 3-15.

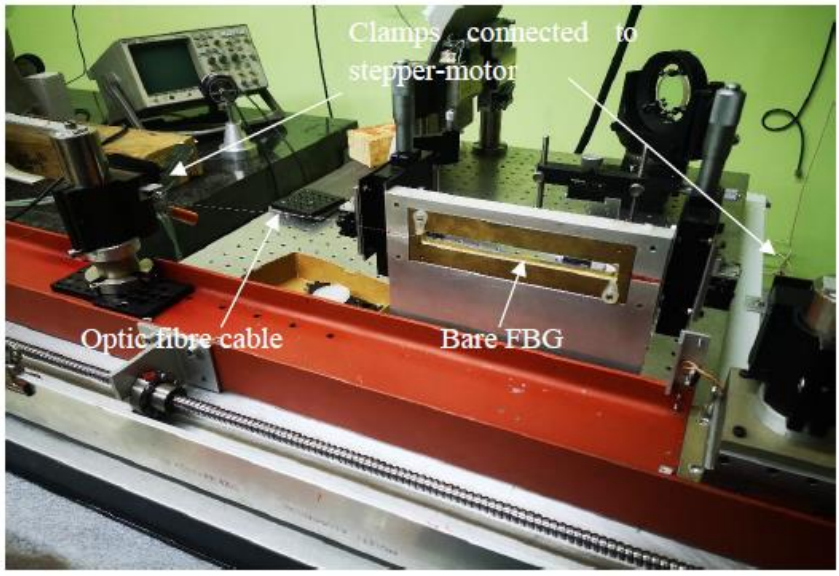

Figure 3-14: Stepper motor and clamp system where bare FBGs are calibrated for strain

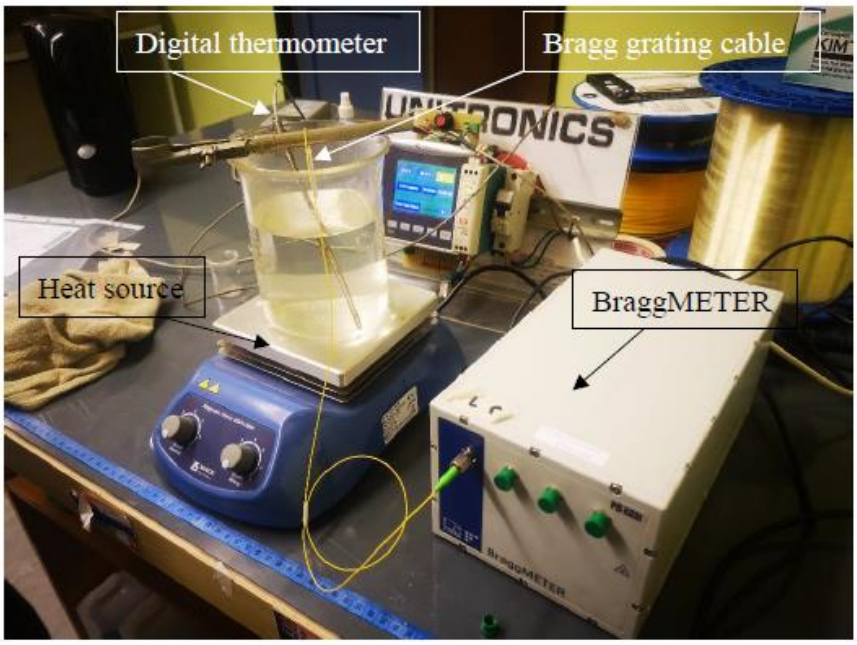

Figure 3-15: Temperature calibration of the bare FBGs used in the reduced scale-tests

3.11 Reduced scale physical models

Many physical model experiments pertaining to sinkholes build on one of the pioneering studies where the stress distribution in sand above a yielding trapdoor was investigated (Terzaghi, 1936). Other trapdoor studies that followed was done by (Costa et al., 2009) where the failure mechanisms induced in granular soil by a deep active trapdoor under normal and accelerated gravity was studied, which was followed by the large-displacement trapdoor study done by (Jacobsz, 2016) conducted on moist and dry medium and fine-grained sands with different densities. After this (Al-Naddaf et al., 2017) also conducted a trapdoor study, but the effect of a surface footing loading on the stability of soil arching under plane strain conditions was studied.

Other studies investigating sinkhole development using a geotechnical centrifuge in the overburden was done by (Craig, 1990) where the conditions for critical stability of a circular cavity that formed after removing the underlying strata support were studied. This study was followed by (Abdulla & Goodings, 1996) where a dimensionless design chart, through the course of fifty-one experiments, was developed to predict failure by investigating sinkhole development in weakly-cemented sand underlain by limestone bedrock. After that (Goodings & Abdulla, 2002) built on their 1996 study with a further forty-nine experiments. Following this (Bronkhorst & Jacobsz, 2014) conducted accelerated gravity experiments where, like Abdulla & Goodings (1996), weakly-cemented sand beams spanned gaps of various sizes and the data presented was found to be in contrast with what Abdulla & Goodings (1996) presented but agreed with predictions based on finite element analysis studies that were conducted by (Drumm et al., 2009).

Many other small-scale tests are reported in the literature from 1979 to 1988 which are well summarised by Altaee & Fellenius (1994) where various tests were performed by numerous researchers either under normal gravitational conditions or either accelerated gravitational conditions to mostly simulate the bearing capacity of footings or small-scale pile groups. Many researchers, however, questioned the effectivity of testing small-scale models under normal gravitational conditions as no reference was made to scaling relations and did not suggest how the results could be translated to the behaviour experienced by the prototype.

Therefore, today many researchers make use of small-scale models in geotechnical centrifuges to model various prototypes.

Similar behaviour is found between models and prototypes when small-scale testing is conducted under normal gravitational conditions (1-g) as well as in a geotechnical centrifuge as long as the model and prototype has initial soil states are at equal proximity to the steady-state line. Then, when stresses are normalised to the initial mean stress, the model and prototype will behave in the same manner (Altaee & Fellenius, 1994). Figure 3-14 illustrates the relation can be considered where the prototype has a mass, M, and has the dimensions L × B × H. To go to a reduced scale model, scaling laws have to be applied. These laws are called similitude laws and Altaee & Fellenius (1994) states that similitude laws are empirical laws that have been created to extrapolate results obtained from small-scale testing to prototype behaviour.

A simple sinkhole propagation simulation model was designed and developed, to verify the use of optical fiber sensing fibers for deformation measurement. The sinkhole model was constructed inside a Perspex box, with inner dimensions of 400×270×80 mm (length × height × width). The void was represented through a balloon full of water. The sinkhole collapse was induced by the deflation of a balloon, using a controlled valve, Figure 3-16. The diameter of the balloon ranged from 95 mm to 160 mm, representing a prototype of 12×8.1×2.4 m, using a scale of 1:30. The prototype is representing the scenario of a medium sinkhole 2-5 m, at medium (1-5 m) to large (5-15 m) depth categories (Buttrick et al., 2001). The model is reduced by a scale factor (N) scaling laws can be used to convert the measured properties and values of the model to a full-scale prototype equivalent. Applicable scaling laws are shown in Table 3.1.

Table 3.1: Scaling relations 1-g test (Ni et al., 2016)

Variable	Scaling factor
Length	1/n
Displacement	1/n
Density	1
Friction angle	1
Strain	1
Time	$1/n^{(1/2)}$

These investigations aim to monitor the soil deformation (sinkhole and subsidence) using a small scale prototype of an actual site in the lab, in the laboratory using the physical model under the influence of a leaking pipe, through optical fibre sensors. A good understanding of a sinkhole formation can allow providing a warning system for early detection of sinkhole formations and their upwards propagation.

The experimental component of this project included three series of tests, summarised in Table 3.2 below. The first series included five tests on dry soil, with soil cover ratios (H/B) (overburden (H), balloon diameter (B) H/B> 3 simulating deep conditions. The second series included seven tests, the water content was gradually increased, and the soil cover ratio adopted was H/B < 3 simulating shallow conditions and H/B > 3 simulating deep conditions. There was a 3rd and 4th series of tests that allowed for the simulation of a leaking pipe, that represents a buried pipe of water supply in situ (Rwelamila et al., 2018). This series covers two tests, one with the dry sand that was used for test series I and II, and the second with the residuum of dolomite, usually called Wad material. Both cases assumed shallow condition.

Table 3.2: Summary of tests

Series	Test	Id %	B(cm)	H (cm)	Comments
I	1	60	15.56	27.00	Dry sand (H/B <2)
12 sensors	2	65	15.30	27.00	Dry sand (H/B < 2)
	3	100		27.00	Dry sand with abutments
	4	40	11.50	27.00	Dry sand with abutments (H/B > 2)
	5	55	16.80	27.00	Dry sand with abutments (H/B < 2)
II	1	40	9.50	35.50	Dry sand H/D > 3 w = 0%
4 sensors	2	40	9.50	35.50	Dry sand H/D > 3 w = 8%
	3	40	9.50	35.50	Dry sand H/D > 3 w = 12%
	4	40	9.50	10.50	Dry sand H/D > 3 w = 0%
	5	40	9.50	10.50	Dry sand H/D > 3 w = 8%
	6	40	9.50	10.50	Dry sand H/D > 3 w = 12%
	7	40	9.50	10.50	Dry sand H/D > 3 w = 16%
IV					
3 sensors	1	40	12	14	Dry Sand – leaking pipe (H/B <2) w = 16%
	2	40	12	14	Dry Sand – leaking pipe (H/B <2) w = 16%
IV	1	40	12	14	Dry Sand – leaking pipe (H/B <2)
9 sensors	2	40	12	14	Dry Sand and Wad (w = 80%) (leaking pipe)

3.12 Experimental Design

In the first series of test, the layers of sand were placed and four optic fibre cables with FBGs on each optic fibre cable were placed. Twelve strain sensors (S1-S12) were multiplexed into 3 FBGs per fibre cable, 53 mm apart, to determine the maximum expected strain and strain near the boundaries of the cavity as it propagates upwards, Figure 3-17. The FBG sensors were manufactured in single mode photosensitive fibre in the Photonics Research laboratory of the University of Johannesburg using the phase mask technique and an Nd: YAG laser using the 266 nm wavelength. The FBG sensors were printed to reflect in the wavelength range between 1540 nm and 1555 nm.

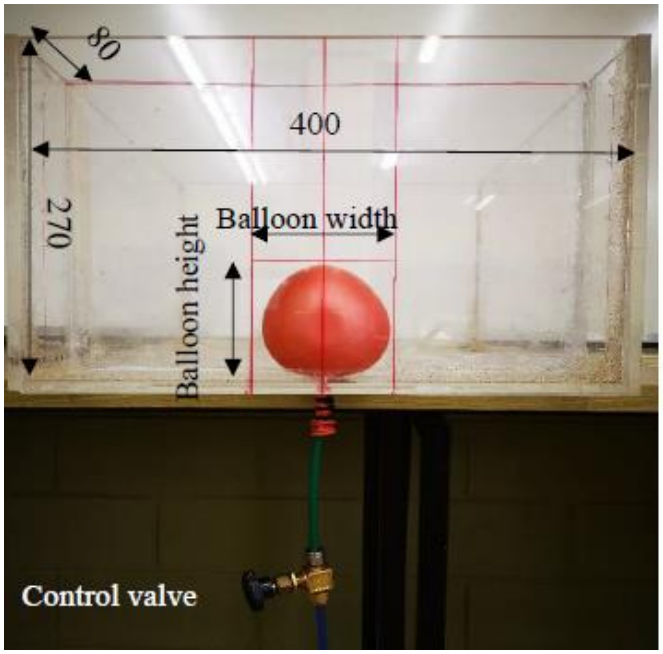

Figure 3-16: Model geometry all dimensions in mm

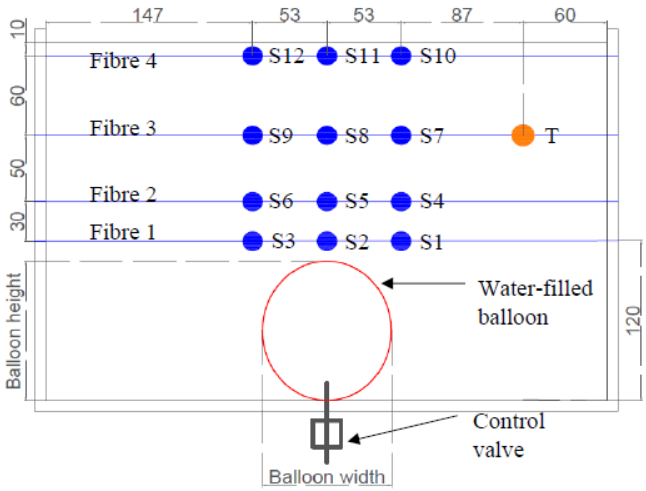

Figure 3-17: Optic fibre sensor layout in the reduced scale model showing the location of sensors (S1-S12) and the temperature sensor (T). Dimensions in mm

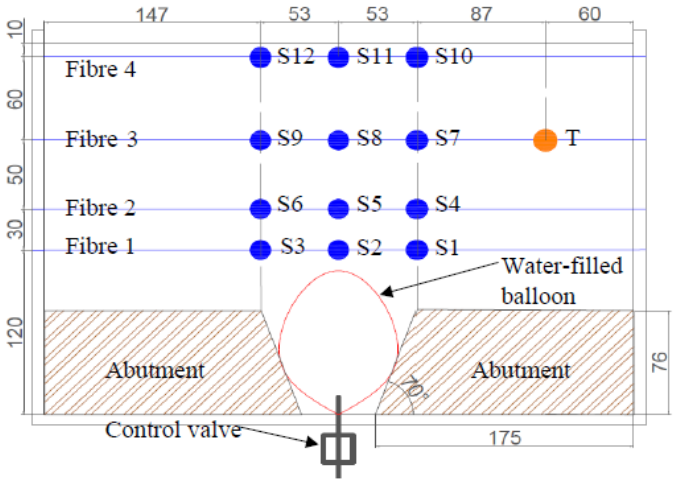

Figure 3-18: Optic fibre sensor layout in the reduced scale model for the experiments conducted with abutments. The strain sensors (S1-S12) and the temperature sensor (T) are also displayed. All dimensions in millimetre.

The sand layers in the model were placed and compacted in alternating brown (20 mm thick) and blue (10 mm thick) layers to visualise the shape of the failure throughout the testing process. As the sand layers were placed and compacted five optic fibre cables were embedded into the model. Four of the optic fibre cables measured strain and had three strain FBGs in array. After the soil was placed and compacted in layers and the sensors were embedded the optic fibre cables were connected to the HBM FS22SI Braggmeter. Thereafter, testing commenced as the control valve was opened to let the water out of the balloon at a controlled rate.

The models were built to sand relative values of 60%, 65% and 95% and densities of 1560.98 kg/m^3, 1623.41kg/m^3, 1705.61kg/m^3 respectively and were tested under normal gravity (1g). The water-inflated balloon had a diameter of 95 mm. The deflation of the balloon allowed for the upwards propagation of the sinkhole in two-dimensional plane-strain conditions. The balloon was deflated by letting water out at a flow rate of 34.17 ml/min, 47.40 ml/min and 41.43 ml/min respectively. The induced movement due to the balloon deflation was 90 mm, which allowed for the visualisation of fully developed failure surfaces within the soil mass.

In the second series of tests, the moisture content of the soil was increased from 0 to 8%, 12% and 16%. These moisture contents were chosen as they are close to the optimum water content of the soil. This was done with simply adding water to the soil until the soil's moisture content reached a satisfactory level. The soil was slightly compacted to interlock the grains and to satisfy the boundary of the model.

Based on the results of the performed tests when water content was increased from 0% to 8%, 12% and16% the voids did not develop to the surface and sinkholes were not formed for both shallow and deep conditions.

In the third and fourth series of tests, a simple simulation of a sinkhole model in a cuboid box was constructed with Perspex material, with the internal dimensions of 500x400x80 mm (length x height x width). Alike in the previous tests, a scaling of 1/30 was used for representing a prototype of 15 x 12 x 2.4 metres. The diameter of the balloon in this experiment was 100 mm. The cover depth of the soil in this experiment was 140. The cover to diameter ratio is thus 1.4 which is less than 3(H/D<2). The soil was compacted to a density of 1686.70 Kg/m^3.

Three optical cables with three gratings sensors each were placed on top of the cavity, another on the middle of the model and the last one was embedded at 10 mm depth for strains measurements. An additional optical fibre cable with two sensors was isolated to strain and placed vertically closer to the cavity in the influence zone of propagation to measure the change in temperature during the event. Figure 3-19 shows the experimental setup and Figure 3-20 and Figure 3-21 illustrate the position of each sensor within the model setup for the two series of tests.

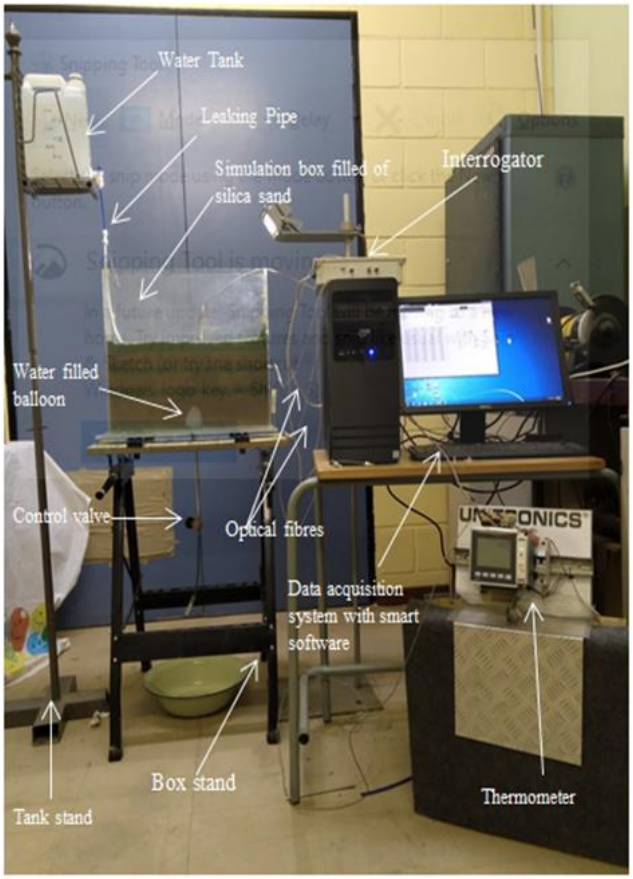

Figure 3-19: Experimental setup

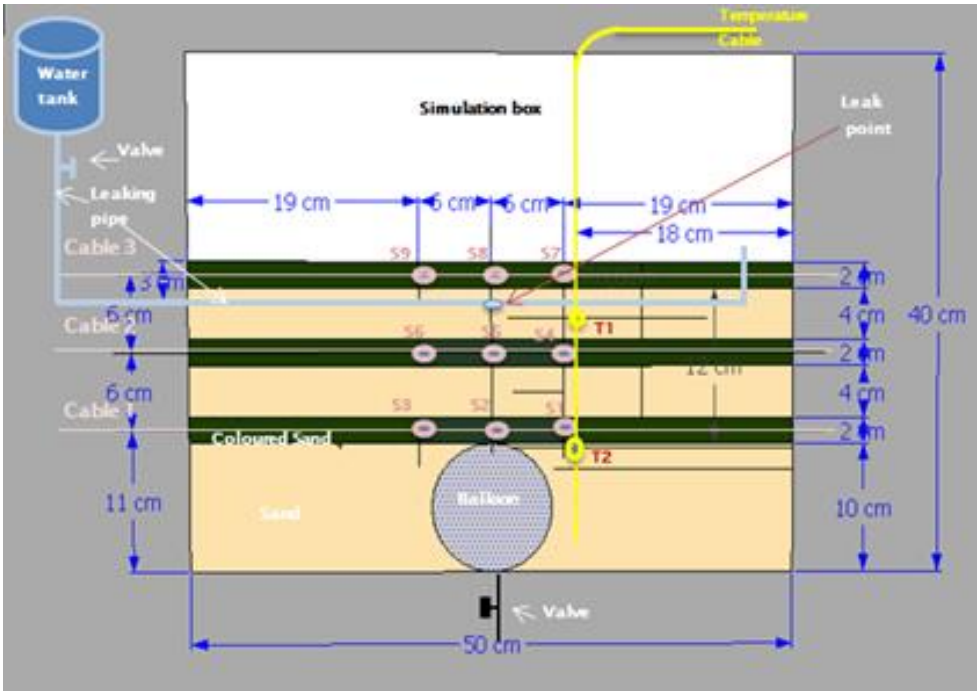

Figure 3-20: Optic fibre sensor layout in the reduced scale model for the experiments conducted. The strain sensors (S1-S9) and the temperature sensor (T1-T2) are also displayed.

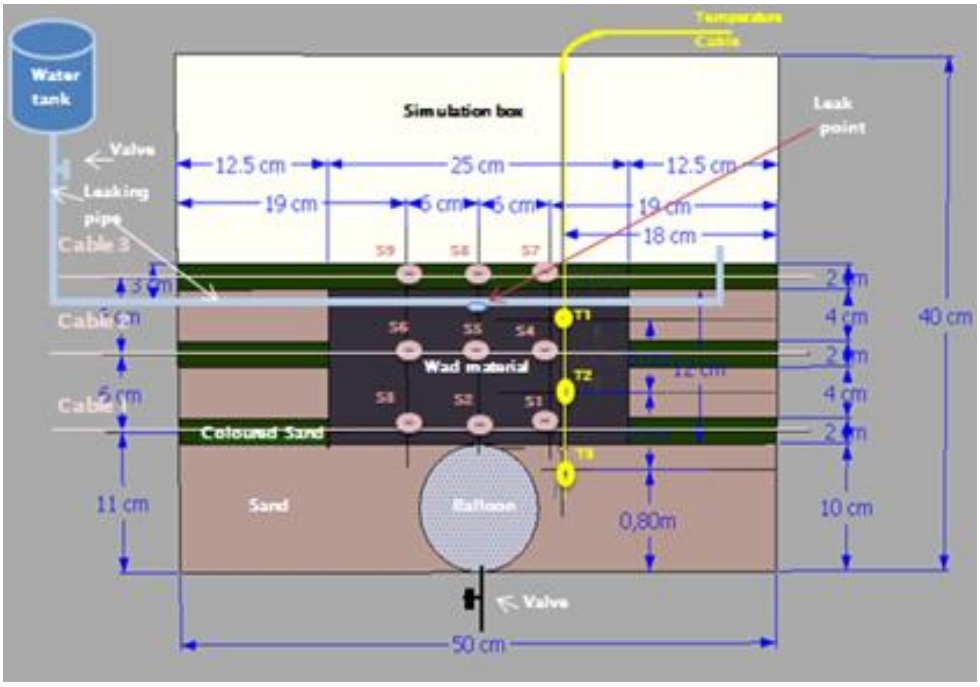

Figure 3-21: Optic fibre sensor layout in the reduced scale model for the experiments conducted with the wad. The strain sensors (S1-S9) and the temperature sensor (T1-T3) are also displayed.

3.13 Results

The tests started as soon as the balloon was inflated with 440 ml of water and the control valve was opened. Therefore, strain developed throughout the soil medium as the balloon deflated and the void progressed upwards towards the surface. The strain results for the various tests are displayed from Figures 3-23 to 3-24 and these results can be directly compared to the respective test progression photos displayed in Figures 3-25 to 3-29.

As the tests were conducted, temperature was monitored using an FBG within the soil medium. Thus, it was assumed that all strain sensors were affected throughout the soil medium by the same temperature fluctuations. Therefore, all strain results are compensated by temperature.

While the control valve was opened the sand above the void that was created by the balloon started moving into where the void used to be. Therefore, the failure mechanism can be seen and indicated that the failure surface propagated vertically upward with the apex of the shaft narrowing and never be wider than the width of the balloon. It can be seen that the zone of influence narrowed before the sinkhole developed and as soon as a sinkhole would appear at the surface, secondary failure would set in, widening the zone of influence thereby creating a funnel-shaped sinkhole. The final sinkhole widths that formed ranged in different sizes as the various tests had a range of relative densities that were compared to Archer (2014). It must, however, be noted that all sinkholes that formed had almost the same widths and depths, but it must be noted that the tests that were conducted using abutments had the greatest sinkhole depths of 43 mm and 50,53 mm respectively.

The strain, determined from the various FBGs, for the tests conducted without abutments (Test 1, Test 2, Test 2) ranged from -0.0000401 mm/mm to 0.00119 mm/mm. The strain for the tests conducted with abutments (Test 4, Test 5) ranged from -0.000421 mm/mm to 0.00212 mm/mm. Test 3 had no failure as the void did not progress upwards towards the surface as the balloon deflated. Comparing the strain data from Test 1 to Test 5 on the same scale makes it look like no strains developed in Test 3 as the balloon deflated. However, once zooming into the data, it can be seen that the strain does in fact increase, although very small, as the balloon deflates. An example of what the raw and processed data looks like is displayed in Figure 3-22 below.

		Strain											
	Volume reduction (%)	Sensor 1	Sensor 2	Sensor 3	Sensor 4	Sensor 5	Sensor 6	Sensor 7	Sensor 8	Sensor 9	Sensor 10	Sensor 11	Sensor 12
(a)	0	1,89E-06	1,51E-06	1,72E-06	3,23E-07	8,07E-07	1,02E-06	1,4E-06	1,83E-06	1,02E-06	-2,7E-07	5,38E-08	-8,6E-07
	0,17401433	1,89E-06	1,61E-06	2,26E-06	1,62E-07	7,54E-07	1,4E-06	1,56E-06	1,56E-06	1,18E-06	9,71E-07	-1,6E-07	-4,8E-07
	0,348028659	1,62E-06	1,67E-06	2,1E-06	1,08E-07	8,61E-07	1,02E-06	1,13E-06	1,24E-06	1,07E-06	1,62E-07	1,08E-07	-8,1E-07
	0,522042989	1,83E-06	1,67E-06	1,88E-06	0	9,69E-07	1,24E-06	1,73E-06	2,21E-06	1,13E-06	5,93E-07	1,08E-07	-5,4E-07
	0,696057318	1,83E-06	1,72E-06	2,04E-06	-1,1E-07	8,61E-07	1,07E-06	1,62E-06	1,67E-06	8,06E-07	5,93E-07	3,23E-07	-6,4E-07
	0,870071648	2,1E-06	1,29E-06	2,64E-06	9,17E-07	1,35E-06	1,29E-06	2,16E-06	1,78E-06	9,67E-07	1,51E-06	7E-07	-8,1E-07
	1,044085978	1,89E-06	1,99E-06	2,15E-06	9,17E-07	1,02E-06	1,24E-06	1,83E-06	2,21E-06	1,24E-06	8,09E-07	9,15E-07	-1,2E-06
	1,218100307	2,64E-06	1,61E-06	2,26E-06	5,39E-07	1,35E-06	7,52E-07	1,94E-06	1,94E-06	3,22E-07	1,35E-06	9,69E-07	-1,5E-06
	1,392114637	2,16E-06	1,88E-06	1,99E-06	4,31E-07	1,35E-06	1,24E-06	1,62E-06	1,51E-06	1,13E-06	7,55E-07	4,84E-07	-8,1E-07
	1,566128967	1,73E-06	1,13E-06	1,67E-06	-5,4E-08	8,07E-07	8,06E-07	1,19E-06	1,51E-06	1,13E-06	3,24E-07	2,15E-07	-1,1E-06
(b)	0	2E-06	2,05E-06	2,69E-06	4,31E-07	1,4E-06	9,67E-07	2,16E-06	2,1E-06	1,07E-06	0	-2,7E-07	-4,8E-07
	0,17401433	2,64E-06	-8,6E-07	3,23E-06	-5,4E-07	-1,6E-07	1,23E-06	1,73E-06	3,23E-07	1,88E-06	2,15E-07	-5,9E-07	-1,2E-06
	0,348028659	-1,2E-05	3,77E-07	9,57E-06	-6,5E-06	-2,7E-06	4,3E-06	-2,5E-06	-4,4E-06	5,27E-06	-2,5E-06	-6E-06	-1,3E-06
	0,522042989	-2,4E-05	-7E-07	2,06E-05	-8,3E-06	2,48E-06	4,19E-06	-3,1E-06	-8,2E-06	1,05E-05	-8E-06	-1,1E-05	2,9E-06
	0,696057318	-2,7E-05	-3,3E-06	2,78E-05	-6,3E-06	5,71E-06	8,91E-06	-3,9E-06	-1,2E-05	1,96E-05	-1,1E-05	-1,5E-05	6,12E-06
	0,870071648	-2,8E-05	-4,4E-06	3,2E-05	-3,9E-06	7,27E-06	1,34E-05	-5,8E-06	-1,4E-05	2,61E-05	-1,4E-05	-1,8E-05	8E-06
	1,044085978	-3,1E-05	-7E-06	3,5E-05	-4,5E-06	7,75E-06	1,72E-05	-8E-06	-1,7E-05	3,12E-05	-1,7E-05	-2,2E-05	9,83E-06
	1,218100307	-3,3E-05	-8,9E-06	3,81E-05	-4,1E-06	7,7E-06	2,04E-05	-1E-05	-2E-05	3,47E-05	-1,8E-05	-2,5E-05	1,06E-05
	1,392114637	-3,2E-05	-8,8E-06	4,07E-05	-2,4E-06	7,48E-06	2,23E-05	-1,2E-05	-2,2E-05	3,79E-05	-2,1E-05	-2,7E-05	1,24E-05
	1,566128967	-3,1E-05	-7,2E-06	4,39E-05	-1,8E-06	7,37E-06	2,41E-05	-1,3E-05	-2,4E-05	4,08E-05	-2,2E-05	-3E-05	1,33E-05

Figure 3-22: Raw data received (a) and processed (b) example from Test 2

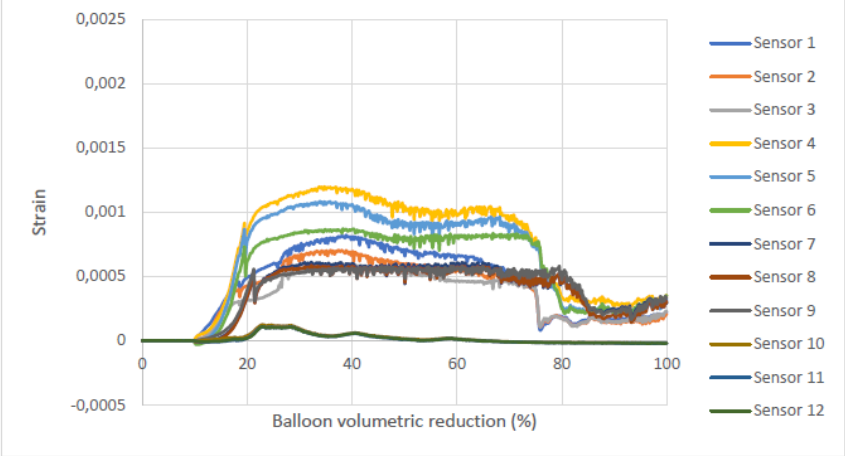

Figure 3-23: Strain development for the sensors in Test 1

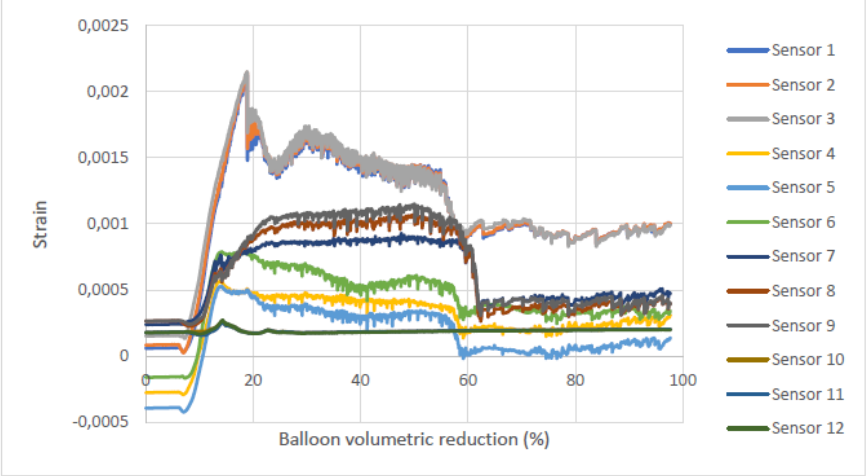

3-24: Strain development for the sensors in Test 4

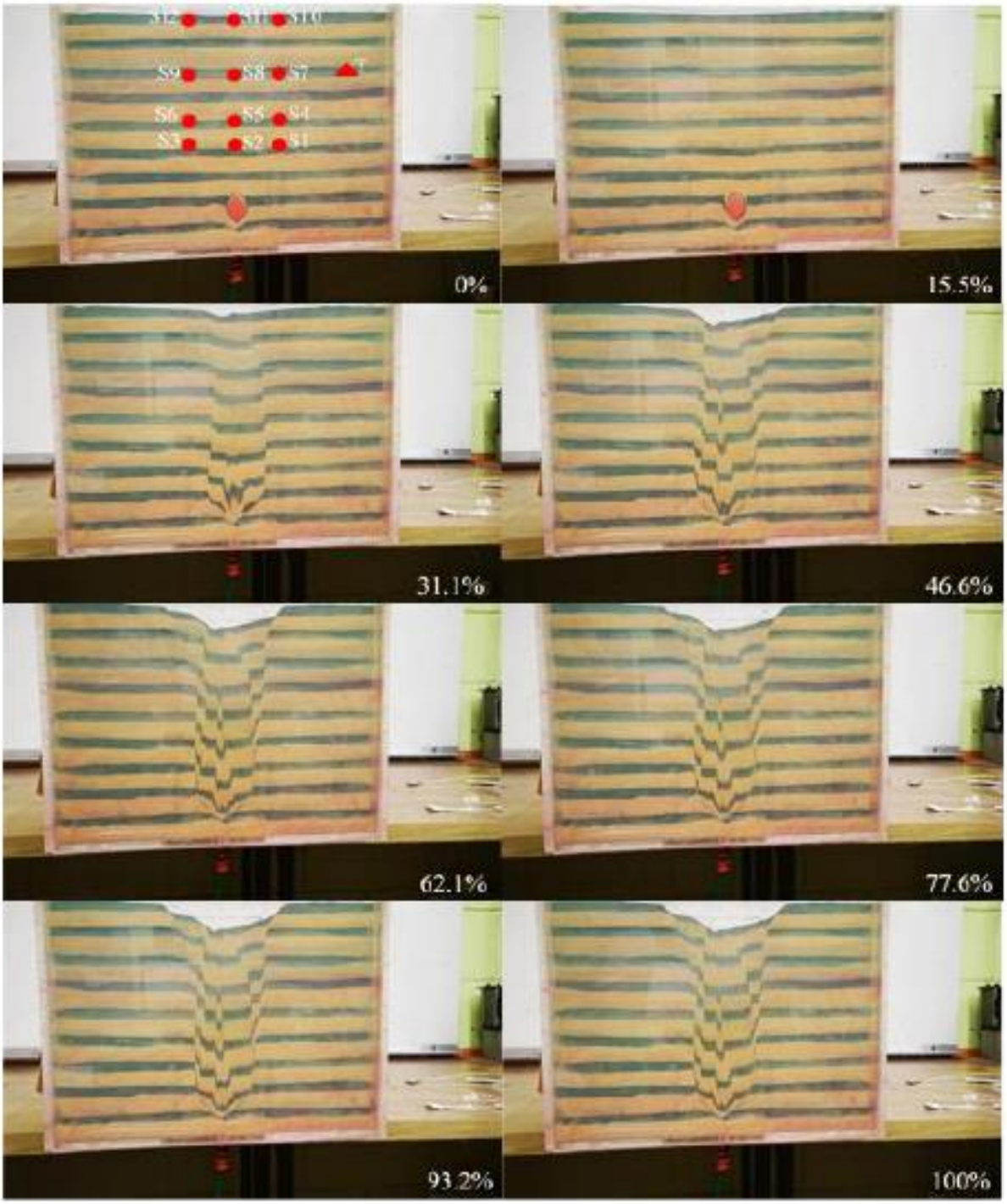

Figure 3-25: Setup of the reduced scale model showing the layout of the optic fibre strain sensors (S1-S2), the temperature sensor (T), and the development of the sinkhole as the volume of the balloon reduces in volume in Test 1

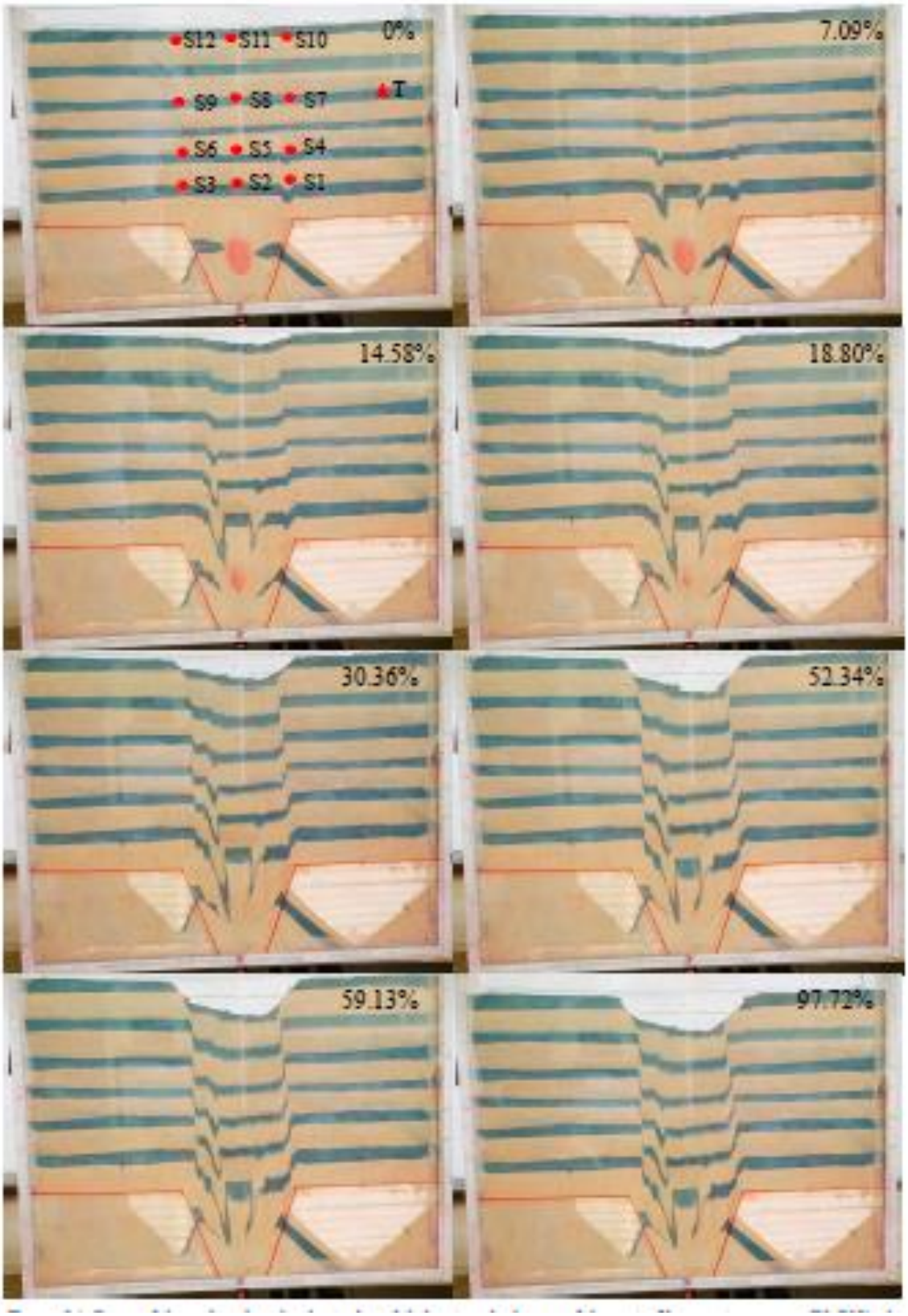

Figure 3-26: Setup of the reduced scale physical model showing the layout of the sensors the temperature sensor and the development of the sinkhole as the volume of the balloon reduces, in Test 4

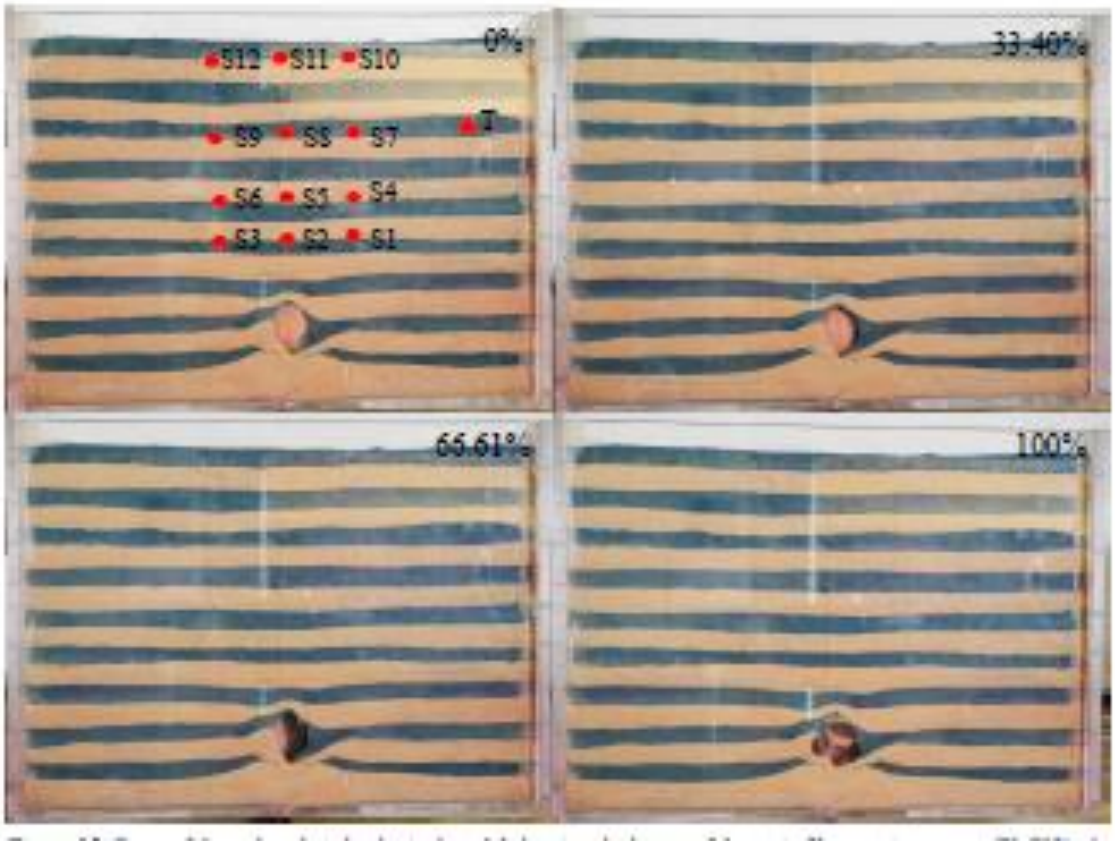

Figure 3-27: Setup of the reduced scale model showing the layout of the optic fibre sensors and the development of the sinkhole failure while volume of the balloon reduces, in Test 3

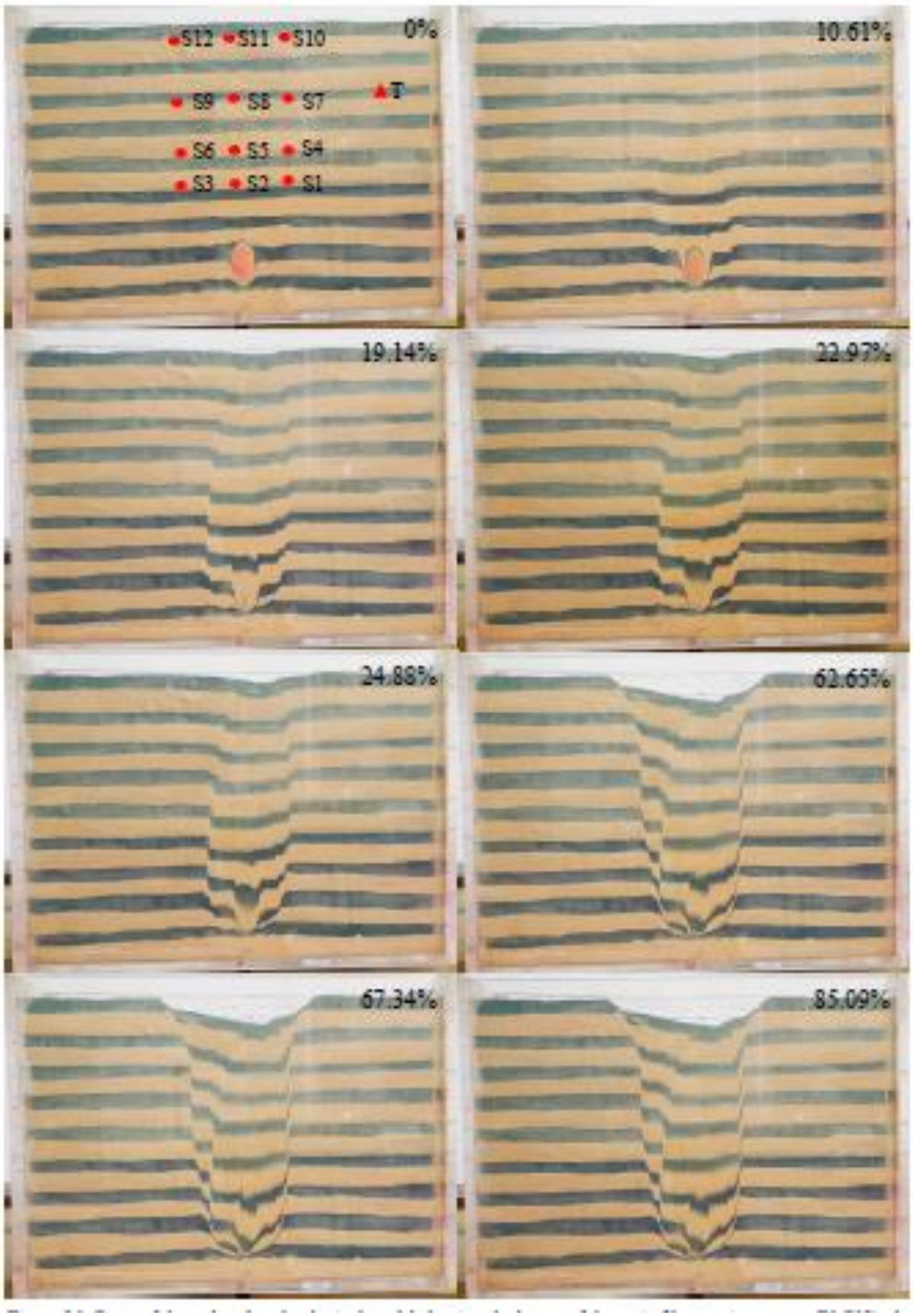

Figure 3-28: Setup of the reduced scale model showing the layout of the optic fibre sensors and the development of the sinkhole failure while volume of the balloon reduces, in Test 2

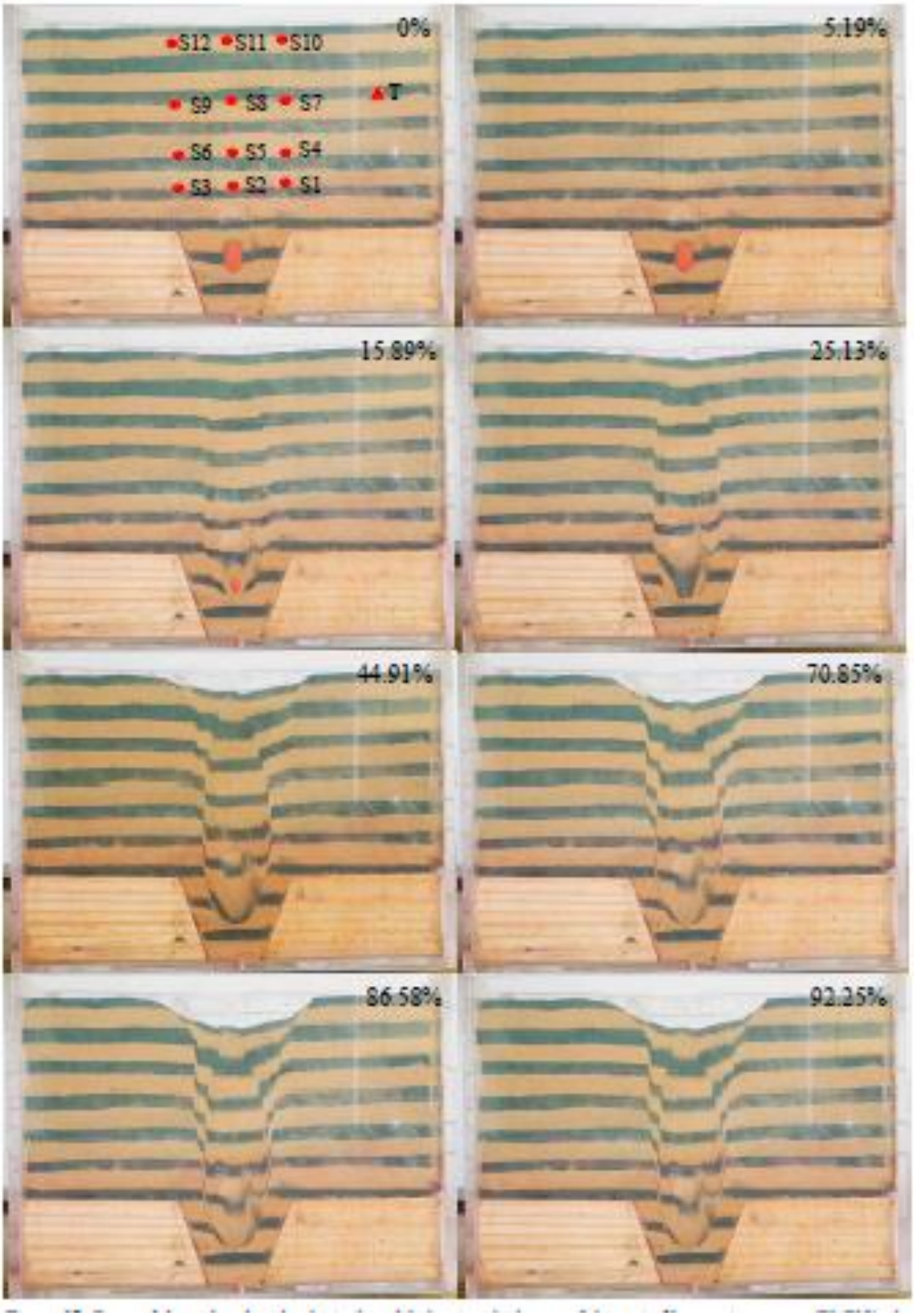

Figure 3-29: Setup of the reduced scale model showing the layout of the optic fibre sensors and the development of the sinkhole failure while volume of the balloon reduces, in Test 5

Figure 3-30 and Figure 3-31 illustrate the process of the induced failures experiments within the silica sand medium, and wad and silica sand.

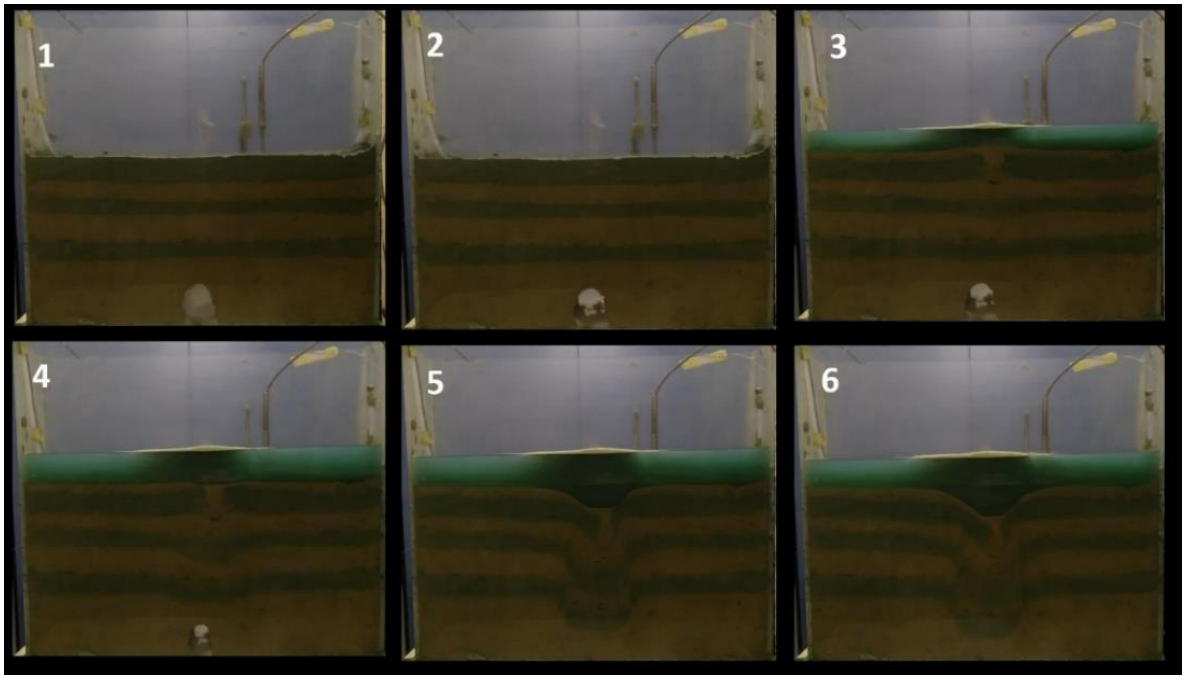

Figure 3-30: Development of the sinkhole failure in silica sand, induced by a leaking pipe, while the balloon deflates

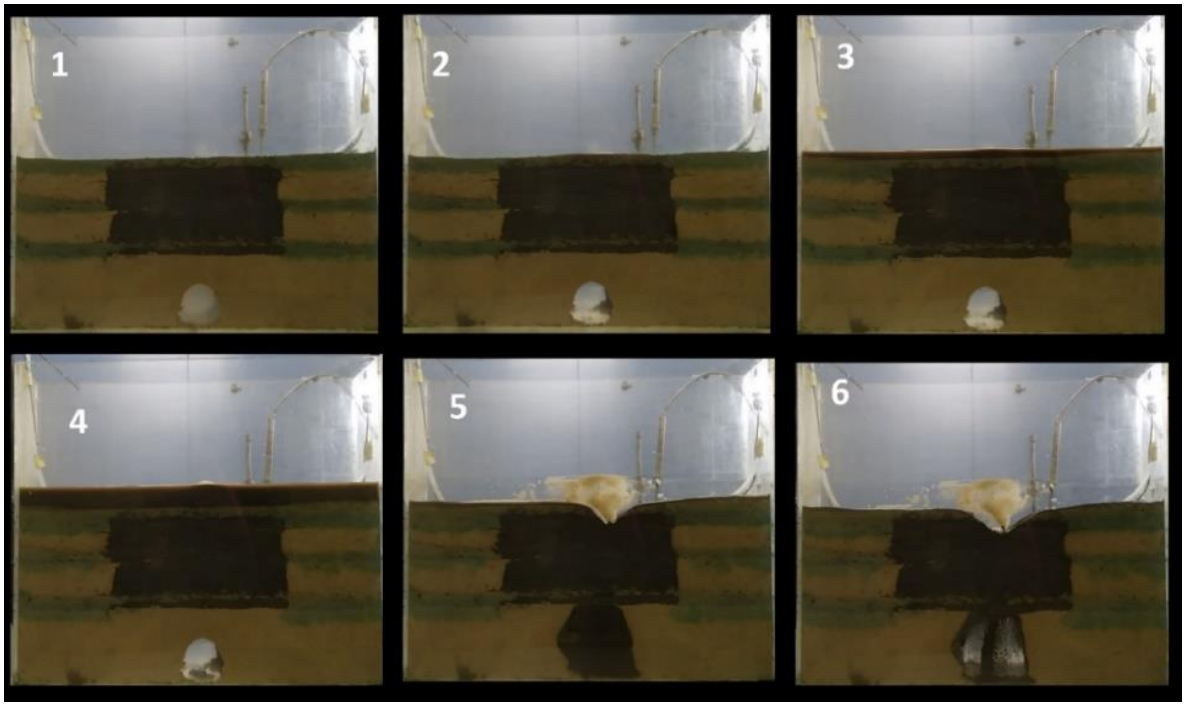

Figure 3-31: Development of the sinkhole failure in wad material, induced by the leaking pipe, while the balloon deflates

The strain, determined from the various FBGs, for the tests conducted with effect of the leaking pipe (series IV and V) ranged from is presented in Figure 3-32 and Figure 3-33 respectively.

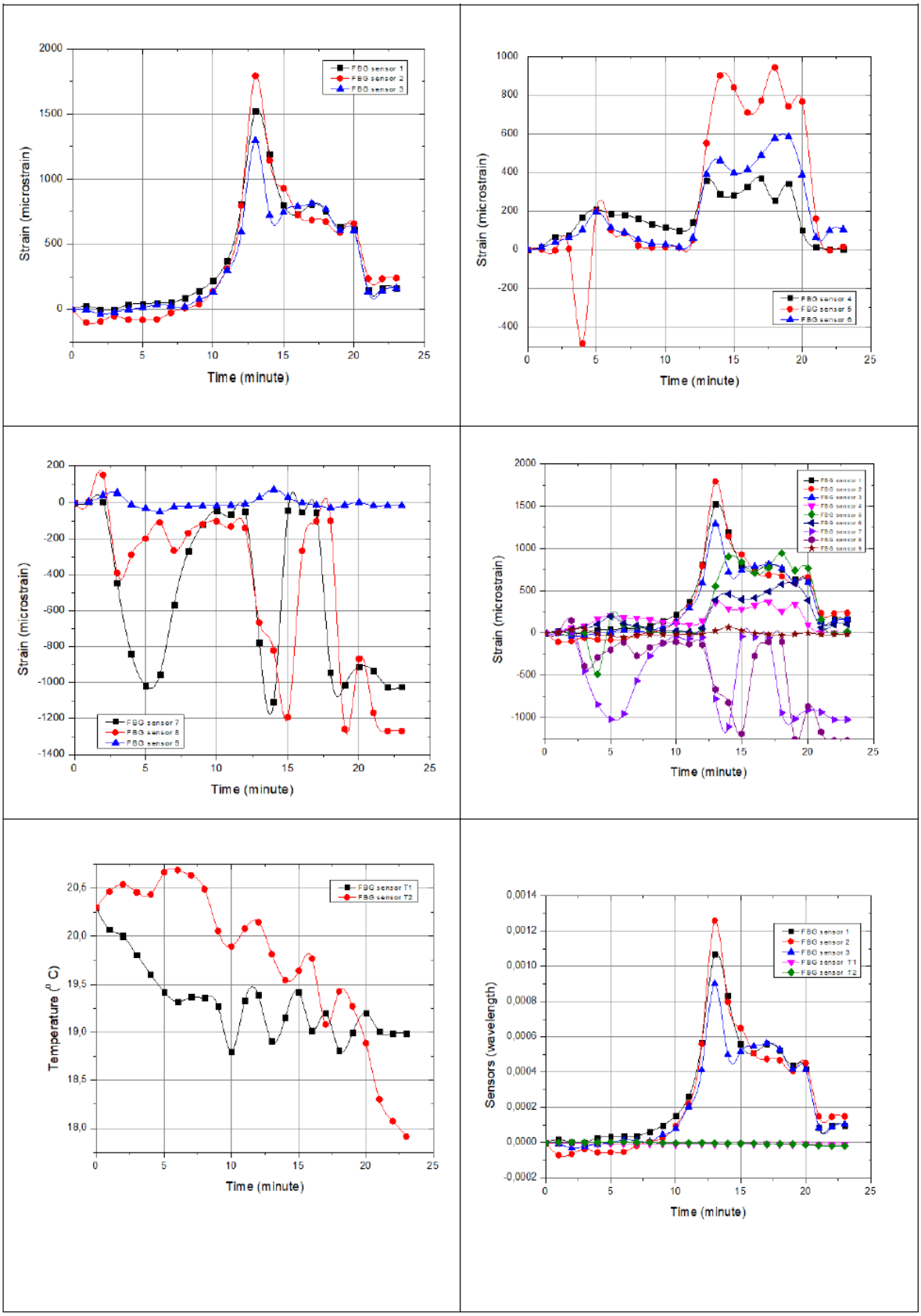

Figure 3-32: Strain development for the sensors in test series IV

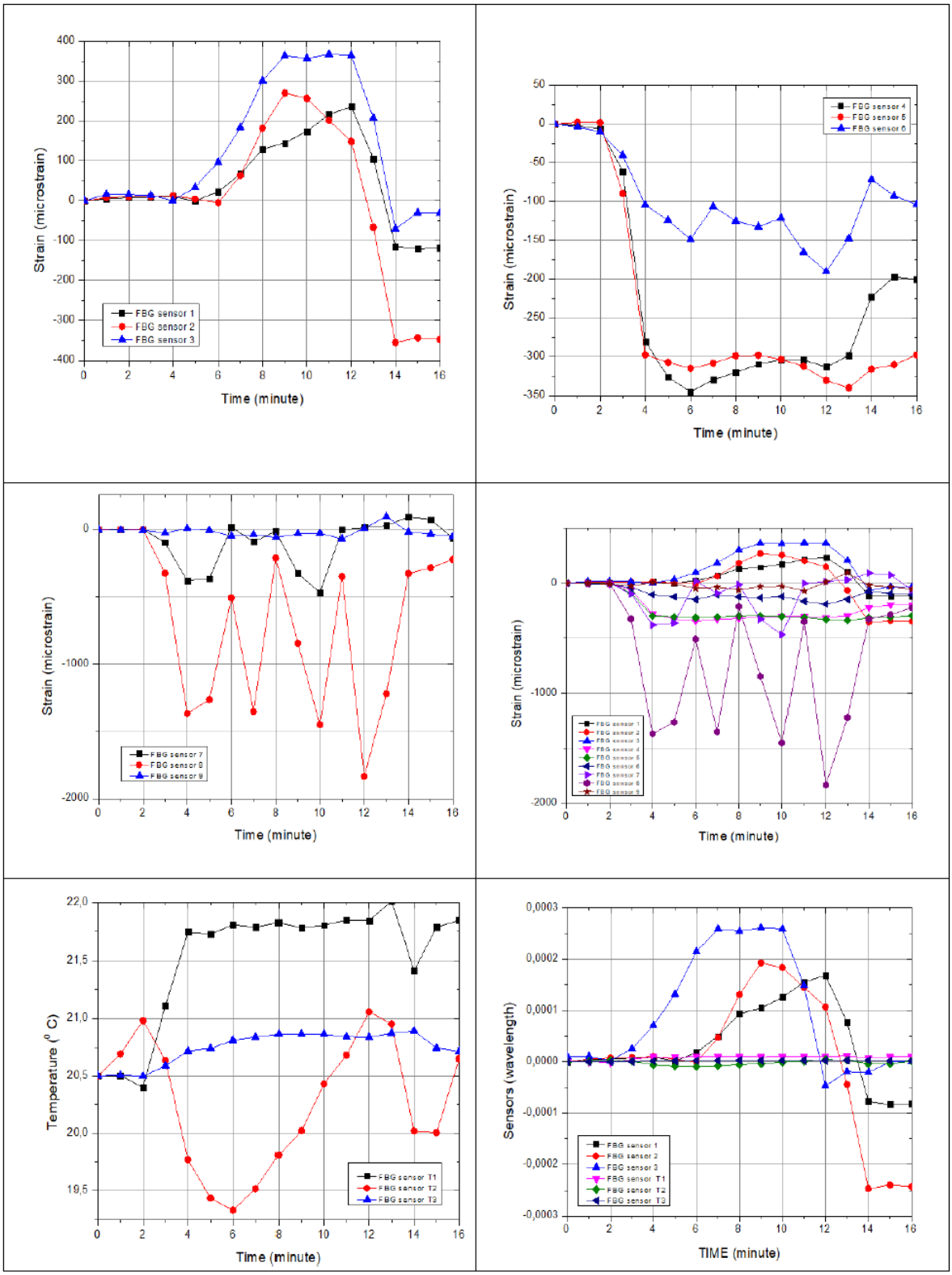

Figure 3-33: Strain development for the sensors in test series V

3.14 Discussion and conclusions

The five conditions that must be met for a sinkhole to form, were considered during the design process for the experiments that were conducted. Thus, dolomite pinnacles or the sides

of a steep-sided subsurface canyon was simulated in Test 4 and Test 5 using wooden abutments. Furthermore, a void was created by means of a water-inflated balloon which in turn created a condition of arching within the soil medium when the balloon would be deflated at controlled rates. Thus, as the void progressed vertically upwards and the water-inflated balloon deflated vertically downwards the original location of the void would serve as the receptacle for overarching sand to move into.

The experiments were performed using a reduced scale model that was manufactured from Perspex and was designed to have the dimensions of 400 × 270 × 80 mm to perform all tests in and a water-inflated balloon was used to simulate a void. A scaling factor of 30 was used. Furthermore, the mechanism of sinkhole formation was studied using the FBGs to measure strains that developed throughout the soil profiles throughout all experiments. The results showed that the induced sinkholes had diameters ranging from 115-168 mm and depths ranging from 33-50 mm regardless of the flow rates of the various tests.

For dry conditions, it was found that sinkhole formation occurs through the void moving upwards as the sand filled the void as the void progressed upwards to the surface in almost a vertical chimney fashion (primary failure) with the apex of the chimney tapering down until the chimney nearly reaches the surface – this behaviour can be seen from Figures 3-27 to 3-28. The same phenomenon has been reported by (Costa et al., 2009) as well as (Jacobsz, 2016). Secondary failure occurred after the chimney reached the surface finally causing a funnel-shaped sinkhole. The experiments performed using abutments to represent pinnacles (Test 4 and Test 5) initially limited the width just as the sinkhole formed but eventually resulted in sinkholes limited to the width of the top of the opening between the abutments. Therefore, sinkholes that formed without abutments (Test 1, Test 2) were smaller than sinkholes with abutments (Test 4, Test 5). However, the experiments that were conducted with abutments (Test 4 and Test 5) developed smaller chimneys compared to the tests that were conducted without abutments.

In the case of $H/D > 3$ (soil cover (H) to cavity diameter ratio (D), the sinkhole mechanism has a form of a vertical chimney that propagates upwards in symmetrical shear bands of failure until the failure is transformed to asymmetrical erratic shear bands. This, however, is only relevant if no moisture is present within the soil. Thus, soil cover to cavity diameter ratio has a great effect on the failure of a sinkhole as well as the amount of strain the soil around the cavity experiences. If $H/D < 3$ the sinkhole has a failure mechanism in the form of a vertical chimney that propagate upwards in symmetrical shear bands till the surface. Strain experienced in $H/D > 3$ models are also higher than strain experienced in $H/D < 3$ models. Thus, soil cover to cavity diameter ratio has a great effect on the failure of a sinkhole as well as the amount of strain the soil around the cavity experiences. This is happening due to higher loading and stress levels forming well developed failure surfaces. At all times the stain in the soil is the highest just above the cavity which is where all sinkholes originate from if they form.

Increased moisture in soil provides additional strength to the arch of a cavity. Water content increase on the fibre-soil interfacial behaviour resulted in small strain readings compared to other literature.

Temperature-compensated strains were measured throughout the whole process and the strains were measured throughout the entire experimentation process in various layers of the sand profile. Therewith, the maximum strains that developed in the experiments that were conducted without abutments were on average smaller (0,001197) than the maximum strains in the experiments that were conducted with abutments (0,002151) but these strains were achieved much earlier than actual visual failure for all experiments that were conducted.

The analysis of the experimental results that were recorded by the FBGs sensors were used to identify a subsidence pattern above the balloon resulting from the induced collapse.

Each sensor array contained three gratings that were written along a single fiber by using UV laser. The sensing length of each FBG was 6 mm. The spacing between FBGs in one fiber was specified for the collection of strain at certain positions. The results showed that the maximum strain was measured by sensor S4 approximately 7.5 $*10^{-3}$ με at 40% balloon volume. reduction. S1 in fiber 1 close to the left side of the balloon measured 8 * 10^{-4}με. S7, S8, S9 measured $6*10^{-4}$ με between 40% and 80% volume reduction. Interestingly S10, S11, S12, did not measure high strains as it would theoretically been expected based on settlement experienced. The results from test 2 indicated that the maximum strain was measured by sensor S3 approximately 6 $*10^{-4}$ με at 30% balloon volume. S6 measured 7*10-4 and S9 $1*10^{-3}$. The recorded strain relates to the secondary failures. The sensors located at the center and the array laid at the highest level within the model measured very low strain which does not verify what would be expected from the empirical observation of surficial settlements induced by excavations of tunnels (Peck 1969).

The soil density influenced the magnitude of the surficial settlement, which was almost 2.5% of the balloon diameter. Surficial settlement was larger in less compacted sands and did not develop at all in very well compacted sands. The max strains that were recorded by FBGs sensors indicated that the highest stains were recorded at the secondary failure surfaces that were developed starting from the sides of the balloon.

The results of the conducted test where failures were induced due to leaking pipe, suggest that the formation and the upwards propagation processes pass through four following phases: Phase 1: Underground cavity formation, The underground cavity was characterised by the time of balloon deflection. The sand (Wad) was dense and compacted on top of the balloon, the soil arched, stable and intact. Phase 2: Weathering process: This period was characterised by the leaking time just after the cavity be formed, while water infiltration occurred. Phase 3: Collapsing process. It was observed that the failure mechanism was sagging collapse. However, in the sand model, the failure mechanism is a sagging plus suffosion. Phase 4 Equilibrium process. During this process there is seeking of balance and stability

Other observations based on the sensor recordings is that in the sand larger deformations were developed in the lower part above the cavity compared to the deformation recorded in the wad where (compression) was recorded. During the leaking period, the water infiltrates in the sand layer while the wad material absorbs water and expands. The wad absorbed much more water before collapse than the silica sand.

The collapsing process in the sand is a slower and continuous than in wad where it is fast and sudden and unexpected. The upwards propagation in the sand affected a large area than the wad which is narrower area was affected. According to the generic sinkhole classification, the wad collapses in suffusion collapse and the sand sagging before collapsing.

The sensors buried at the surface developed almost negative strains in both the silica sand and wad cases. This could be probably attributed to the fact that, the optical fibre cables have been stretched during their setting and the sensors have been subjected to a pre-stressing tension. Moreover, the compaction fact the soil mass pulls the optical fibre cables. The water from the leaking pipe decreases the cohesion between the silica solid grains. The capillarity causes the adhesion and interaction between fibre and soil to decrease and therefore the sensors record negative strain values. The accuracy of the sensors also decreases.

The sand developed large deformations in the lower part located above the cavity compared to the wad while the wad developed negative strain (compression) in the upper part than the sand. During the leaking period, the sand the water infiltrates the sand while the wad material absorbs water and expands. The wad consumed much water before collapse than the silica sand. The collapsing process in the sand is a slower and more continuous than in wad where it is fast and sudden. The temperature results in the sand show a decrease with the

ingress of leaking water in the entire process. However, for wad material, the graph shows that the temperature increases slightly along the process.

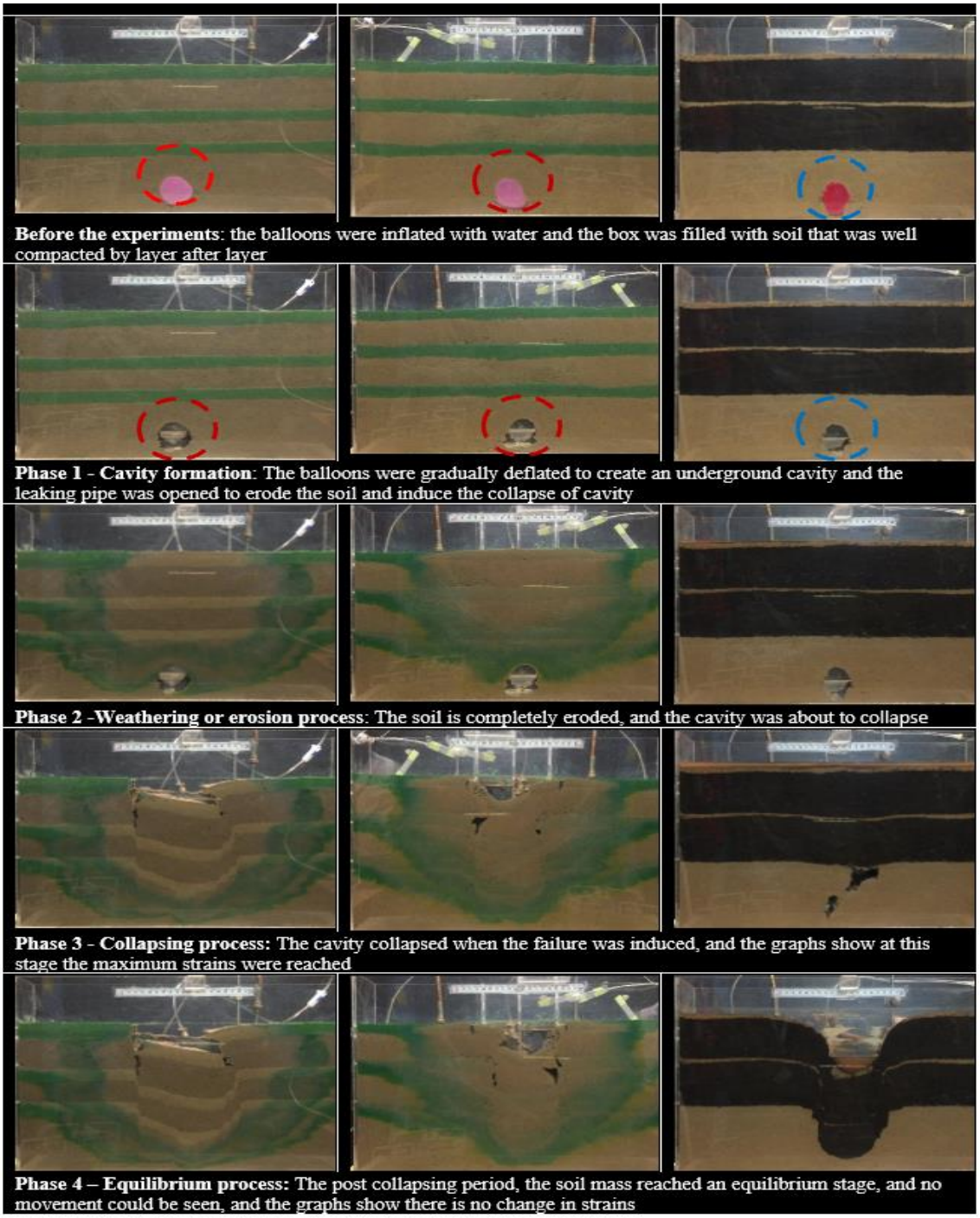

Figure 3-34: Development of the sinkhole failure induced by a leaking pipe

Figure 3-34 displays the recorded images from the experiment at the critical period in tests conducted in series II, where a lower and regulated flow rate of the leaking pipe was considered. The series II tests were conducted to improve and confirm the results obtained in test series I. The images illustrate the development of the sinkhole from the cavity formation, weathering and erosion process of the soil mass, the collapse of the cavity and its upwards propagation in each test.

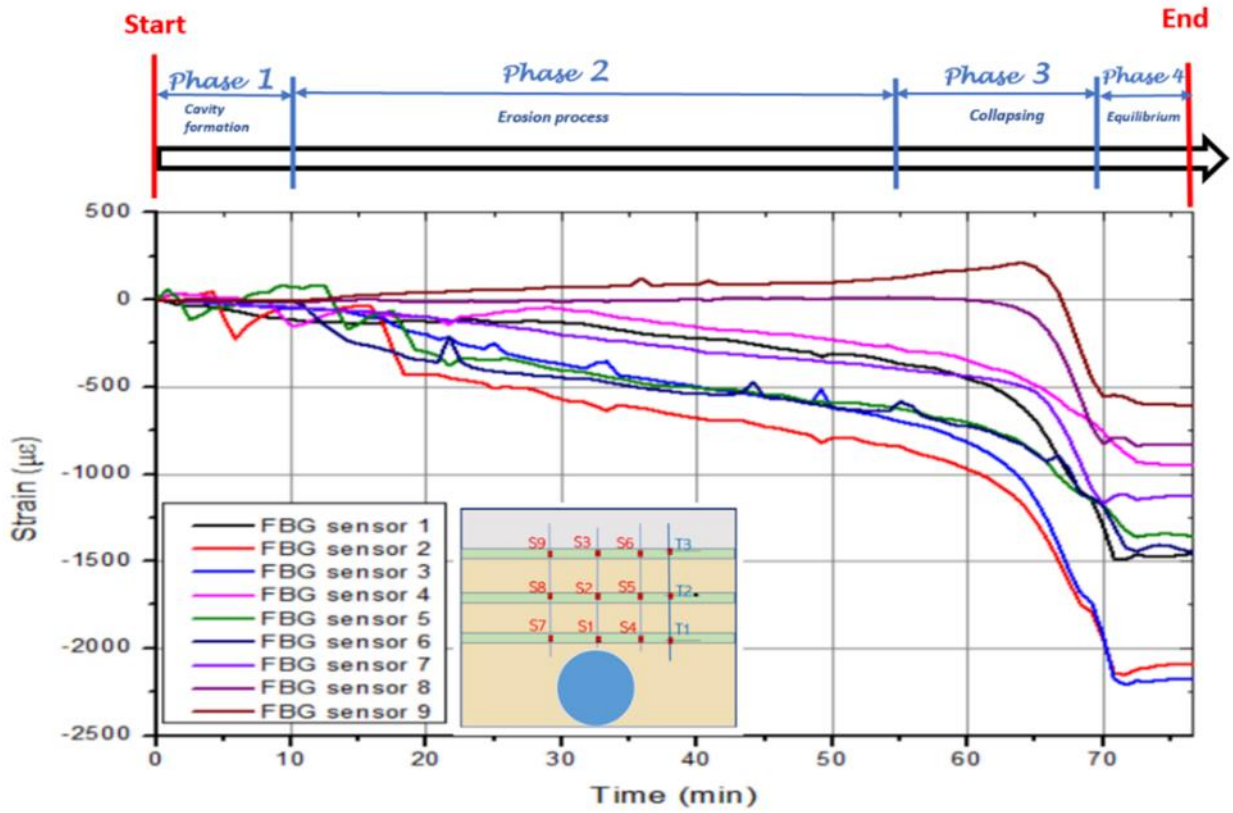

Figure 3-35: Experimental results of Test 4 SS V II (Vertical sensing in the sinkhole model with the silica sand)

Figure 3-35 displays the strains detected by all FBG sensors in the experiment with the silica sand, and the optical fibre sensors cables were placed vertically in the soil mass when the flow rate of the leaking pipe was lower and well regulated. The graph shows the boundaries of the four identified phases according to the duration of the experiment. The state of strain is compressive, strain level is lower, except for sensors S2 and S3, where the levels are higher due to their locations in the central axis of the model. The FBG sensor 9 a heave before to collapse at the left side on top surface that the soil could experience a heave before collapsing at the top surface's left side.

3.15 Can the sensing technology based on FGB sensors be used as an early warning system for alarming sinkhole occurrences?

Considering a series of frames extracted from the experiment in Test 4 SSV II, the FBG sensors were vertically embedded in the model. Based on the visual inspection and the strain signatures recorded, an analysis between the strain signature and the development of sinkhole failure is shown in the images.

The strain has increased significantly due to the ingress of leaking water and induced high compressive stresses in the time interval between the 60th and the 70th minute. It was the critical period of the failure. The images show that before this critical degradation, the sensors have already developed a failure trend, showing the strain increase without any visible signs at the soil surface, even on the box's front panel.

The analysis shows that:

• From the 60th to the 65th minute, there is no visible change in soil deformation within the sinkhole model, but the strain increased significantly during this period.

• From the 65th to the 69th minute and 30 seconds: precursor signs are now visible. A small settlement can be observed at the surface; however, the strain detected by the FBG sensors reaches a maximum magnitude.
• From the 60th minute and 30 sec to the 70th minute and 30 sec: in an interval of one minute only, it can be seen in the images that the failure was sudden and catastrophic. The soil deformation is visible in 60 seconds. However, the strain signature of FBG sensors shows that the equilibrium phase is about to start while the cavity propagates upward to the surface for the sinkhole to be observed.
• From the 70th min 30 sec to the 75th min: the failure continues its physical development, and the strain's curve shows almost a straight line meaning that the concentrated stress in the ground soil was released after the failure. An equilibrium state could be observed after the subsoil fails into the cavity.
• From the 75th to the 77th minute: it can be seen in the images that there was no significant increase in failure, and the magnitude of the strain was constant. So, the equilibrium state continued, the reservoir was filled with failure material, the subsidence movement stopped, and the FBG sensors could no longer record a significant change in strain.

Using FBG sensors as an early warning system for sinkhole occurrences shows promise according to the experimental work results as that the sensors could detect characteristic strain signatures before the initiation of the failure.

3.16 Use of the current research for decision making

This study demonstrated the feasibility of FBG sensors in the geotechnical field for ground movement monitoring. The main objective of this study is to understand the mechanism of the failure process of sinkhole events by monitoring strain changes in reduced scale sinkhole models using the fibre Bragg grating sensors. The mechanism of sinkhole formation was investigated through several 1-g gravity tests in a controlled laboratory environment to supplement current knowledge of real-life strains experienced in dolomitic terrains. Furthermore, this study promoted the integrated science of geotechnical engineering and photonics.

The tests were conducted in two types of rectangular boxes that served as small-scale representations of the field prototypes' outcomes. Perspex material was used to build these boxes. A total of five tests were carried out in both series. Two tests were carried out using wad material mixed with silica sand, and three tests with Cullinan silica sand only. The FBGs were positioned vertically in the model in one of the three tests.

The experimental results suggest that the upward propagation of the sinkhole processes could be divided into phases: Phase 1 – underground cavity formation, characterised by the balloon deflation time, producing a stable arch to support the soil. Phase 2, the weathering process, was characterised by the leaking time (infiltration of water) after the cavity was formed. Phase 3 collapsing process, during which time the failure was induced. Phase 4 The equilibrium period, where the soil mass falls over the sensors and reaches equilibrium.

The vertical sensing of the sinkhole revealed that the upwards propagation of the cavity induced compressive strain in the soil mass above the cavity. The collapse process in the sinkhole models could occur gradually as cover subsidence sinkholes or suddenly and without surface signs, such as cover collapse sinkholes.

The findings indicate that the different models' induced sinkholes had diameters ranging from 13 to 17.20 cm and depths ranging from 3.5 to 11.5 cm. These diameters match a field prototype in the 3.9 to 5.16 m range. The depths range from 1.05 to 3.45 m in the field prototype. The shape of sinkhole mechanism was funnel-shaped in these series of experiments. The

highest strain amplitude, 3.5 x 103 με, was measured in test 3 SSH II by FBG sensor 2. During vertical sensing, in test 4 SSH II, FGB sensors 2 and 3 measured a maximum strain of 2.207x103 με, located at the middle and upper part of the model. Consequently, the FBG sensor above the cavity of each model developed the highest strain.

The findings also suggest that optical fibre sensing can provide a viable option for developing an early warning system. The fibre Bragg grating sensors are sensitive to ground movement and can identify collapse failure before it becomes visible. These sensors have proven to be very suitable for measuring strain in soil profiles, which could act as an early warning indicator for sinkhole failure. Efficient integration of an IoT-enabled FBG sensing system could detect precursor movement of soil mass due to leaking pipes to provide automated decisions.

This practical application of OFS technology would potentially generate a fresh understanding of how such an approach can be incorporated into continuing practice for future monitoring efforts in regions with similar geohazard-prone areas. Surface water management will also help prevent ground geohazards such as sinkholes and subsidence in Karst terrains.

3.17 Subsidence monitoring proactive strategic planning

Tests of the experimental study show that strains of optical fibers embedded in the experimental setup would change in response to changes of the soil loading during leaking pipe. Strains measured by FBGs sensors correspond well with positions of severe soil damage and soil voids induced by leaking pipe. Strain signature of optical fibers at different levels can be used to track upward propagation of soil disturbance. The strain signatures can also be used to determine the location soil void and serve as an early warning of a sinkhole collapse. FBGs offered -reduced the uncertainty in prediction of location and dimension of a potential sinkhole collapse. This technology could potentially become a useful tool to monitor and predict sinkhole collapse and subsidence, when attached to pipes, or when installed along linear infrastructure such as road and railways or pipes.

3.18 References

Abdulla, W. A. & Goodings, D. J., 1996. Modeling of sinkholes in weakly cemented sand. Journal of Geotechnical engineering, 122(12), pp. 998-1005.

Abelson, M. et al., 2018. Nanoseismicity forecasts sinkhole collapse in the Dead Sea coast years in advance. The Geological Society of America, 46(1), pp. 83-86.

Al-Naddaf, M. et al., 2017. Investigation of stability of soil arching under surface loading using trapdoor model tests. Seoul.

Altaee, A. & Fellenius, B. H. (2011). “Physical modeling in sand”. Canadian Geotechnical Journal. 31. pp. 420-431.

Avutia, D. & Kalumba, D. (2014). “Analytical Study of Dolomite Sinkholes in Centurion, South Africa”. Geotechnical Special Publication. pp. 633-641.

Barrias, A., Casas, J. R. & Villalba, S., 2016. A Review of Distributed Optical Fiber Sensors for Civil Engineering Applications. Physical Sensors, 16(5), p. 748.

Brink, A.B.A. (1979). “Engineering Geology of South Africa-Volume 1”. Building Publications Pretoria. pp. 1-214.

Bronkhorst, W. P. & Jacobsz, S. W., 2014. The behaviour of weakly cemented sand beams spanning over openings. Perth, Australia, Taylor & Francis Group, pp. 1107-1112.

Buchoud, E. et al., 2016. Quantification of Submillimetre Displacements by Distributed Optical Fiber Sensors. IEEE, 65(2), pp. 413-422.

Buchoud, E. et al., 2016. Quantification of Submillimetre Displacements by Distributed Optical Fiber Sensors. IEEE TRANSACTIONS ON INSTRUMENTATION AND MEASUREMENT, 65(2), pp. 413-422.

Buttrick, D. B. et al., 2011. A performance based approach to dolomite risk management. Environmental Earth Sciences, Volume 64, pp. 1127-1138.

Constantinou, S. & van Rooy, J. L., 2018. Sinkhole and Subsidence size across dolomitic land in Gauteng. SAICE, 60(2), pp. 2-8.

Costa, Y.D, Zornberg, J.G., Bueno, B.S. & Costa C.L. (2007). "Failure mechanisms in sand over a deep active trapdoor". Journal of geotechnical and geoenvironmental engineering. 135(11). pp. 1741-1753.

Donaldson, G. W., 1963. Sinkholes and Subsidence caused by subsurface erosion. Salisbury, Proceedings of the Third Regional Conference for Africa on Soil Mechanics and Foundation Engineering.

Drumm, E. C., Aktürk, O., Akgün, H. & Tutluoğlu, L., 2009. Stability Charts for the Collapse of Residual Soil in Karst. Journal of Geotechnical and Geoenvironmental Engineering, 135(7), pp. 925-931.

Goodings, D. J. & Abdulla, W. A., 2002. Stability charts for predicting sinkholes in weakly cemented sand over karst limestone. Engineering Geology, 65(2-3), pp. 179-184.

Gutiérrez, F., Cooper A.H. & Johnson K.S. (2008) Identification, prediction and mitigation of sinkhole hazards in evaporite karst areas. Environmental Geology. 53 (5), pp. 1007-1022. Grattan, K. T. & Meggitt, B. T., 1995. Optical fibre sensor technology. 1st ed. London: Chapman & Hall.

Hecht, E. (2002). "Optics: 4th Edition", International Edition, Book, Adelphi University, Addison.

Heon-Joon, P. & Dong-Soo, K. (2013). "Centrifuge modeling for evaluation of seismic behaviour of stone masonry structure". Soil Dynamics and Earthquake Engineering. pp. 187-195.

Higuchi, K. et al., 2007. Application of new landslide monitoring technique using optical fiber sensor at Takisaka landslide, Japan, Japan: Public Works Research Institute.

Iten, M. (2011). "Novel Applications of Distributed Fiber Optic Sensing in Geotechnical Engineering". Doctoral Thesis. Pp. 1-33. Zurich: ETH Zurich. Doi: DISS. ETH No 19632

Intrieri, E. et al., 2015. Sinkhole monitoring and early warning: An experimental and successful GB-InSAR application. Geomorphology, 241(1), pp. 304-314.

Jacobsz, S. W., 2016. Trapdoor experiments studying cavity propagation. Sun City, South Africa.

Jennings, J. E., Brink, A. B., Louw, A. & Gowan, G. D., 1965. Sinkholes and subsidences in the Transvaal Dolomite of South Africa. Proc 6th International Conference of Soil Mechanics and Foundation Engineering, pp. 51-54.

Jewett, Jr., J. W. & Serway, R. A., 2010. Physics for Scientists and Engineers with Modern Physics. 8th ed. Canada: Cengage Learning Products.

Kapogianni, E., Sakellariou, M. & Laue, J., 2016a. Experimental Investigation of Reinforced Soil Slopes in a Geotechnical Centrifuge, with the Use of Optical Fibre Sensors. Geotechnical and Geological Engineering, 35(2), pp. 585-605.

Kapogianni, E., Sakellariou, M., Laue, J. & Springman, S., 2016. Investigation of the Mechanical Behaviour of the Interface between Soil and Reinforcement, via Experimental and Numerical Modelling. Portugal, Elsevier.

Linker, R. & Klar, A., 2017. Detection of Sinkhole Formation by Strain Profile Measurements Using BOTDR: Simulation Study. Journal of Engineering Mechanics, 143(3).

Lin, Y. B. et al., 2005. Online monitoring of highway bridge construction using fiber Bragg grating sensors. Smart Materials and Structures, Volume 14, pp. 1075-1082.
Lu, X. et al., 2017. Experimental Investigations on Load Transfer of PHC Piles in Highway Foundation Using FBG Sensing Technology. International Journal of Geomechanics, 17(6).
Madabhushi, G., 2014. Centrifuge Modelling for Civil Engineers. 1st ed. CRC Press.
Margiotta, S., Negri, S., Parise, M. & Quarta, T. A., 2016. Karst geosites at risk of collapse: the sinkholes at Nociglia (Apulia, SE Italy). Environ Earth Sci, 75(8), pp. 1-10.
Meltz, G., Morey, W. W. & Glenn, W. H., 1989. Formation of Bragg gratings in optical fibers by a transverse holographic method. Optical letter, 14(15), pp. 823-825.
Messerklinger, S., 2014. Formation mechanism of large subsidence sinkholes in the Lar valley in Iran. Quarterly Journal of Engineering Geology and Hydrogeology, 47(1), pp. 237-250.
Mihailov, S. J., 2012. Fiber Bragg Grating Sensors for Harsh Environments. Sensors, Volume 12, pp. 1898-1918.
Lanticq, V., Bourgeois, E., Magnien, P., Dieleman, L., Vinceslas, G., Sang, A. & Delepine-Lesoille, S. (2009). "Soil-embedded optical fiber sensing cable interrogated by Brillouin optical time-domain reflectometry (B-OTDR) and optical frequency-domain reflectometry (OFDR) for embedded cavity detection and sinkhole warning system". Measurement Science and Technology 20 (3).
Lei, M., Jiang, X. & Yu, L. (2002). "New advances in karst collapse research in China". Environmental Geology. 42. pp. 462-468.
Oosthuizen, A. C., 2013. The hazard of sinkhole formation in the Centurion CBD and surrounding areas: Pretoria, Gauteng, University of Pretoria: Unpublished M.Sc. Thesis.
Oosthuizen, A. C. & Van Rooy, L., 2015. Hazard of sinkhole formation in the Centurion CBD using the Simplified Method of Scenario Supersition. The South African Institution of Civil Engineering, 57(2), pp. 69-75.
Oosthuizen, A. & Richardson, S., 2011. Sinkholes and subsidence in South Africa, Council for Geoscience.
Ozkahriman, F. & Wartman, J., 2007. Investigation of 1-g similitude laws by "modeling-of-models" exercise. Denver, Colorado, United States, ASCE.
Picarelli, L. et al., 2015. Performance of slope behavior indicators in unsaturated pyroclastic soils. Journal of Mountain Science, 12(6), pp. 1434-1447.
Rao, Y. J., 1998. Fiber Bragg grating sensors: principles and applications. In: K. G. a. B. Meggit, ed. Optical Fiber Sensor Technology. 2 ed. London: Chapman and Hall, pp. 355-379.
Richardson, S., 2013. Sinkhole and subsidence record in the Chuniespoort group dolomite, Gauteng, South Africa, Pretoria: Unpublished MSc Thesis, University of Pretoria.
Schofield, A. N., 1980. Cambridge Geotechnical Centrifuge Operations. Géotechnique, 30(3), pp. 227-268.
Schöning, W. L., 1990. Verspreiding van sinkgate en versakkings in die dolomietgebiede suid van Pretoria. Unpublished M.Sc. thesis: University of Pretoria.
Schöning, W. L., 1996. Distribution of sinkholes and dolines in the area south of Pretoria. Seminar on the engineering geological evaluation of sites on dolomite areas: University of Pretoria.
Sharma, P., Arora, R., Pardeshi, S. & Singh, M. (2013). "Fiber Optic Communications: An Overview. International Journal of Emerging Technology and Advanced Engineering". (3). pp. 474-479.
Shinoda, Y. et al., 2006. Fundamental experiment of Multiple-point Measurement for Strain by Fiber Bragg Gratings using Optical Frequency Sweeping. Busan, ICASE.
Soga, K. & Schooling, J., 2016. Infrastructure sensing. Interface Focus, 6(4), p. 20160023.

South African National Standard (SANS), 2012. SANS 1936-1:2012, SABS.
Taylor, R. N., 1995. Geotechnical Centrifuge Technology. 1st ed. New York, USA: Taylor & Francis.
Teisseyre, R., Takeo, M. & Majewski, E., 2006. Earthquake Source Asymmetry, Structural Media and Rotation Effects. Springer Science & Business Media.
Terzaghi, K., 1936. Stress distribution in dry and saturated sand above a yielding trap-door. Harvard University, Cambridge.
Udd, E., 1995. Fiber Optic Smart Structures. 1st ed. United States of America: Wiley & Sons.
Udd, E. & Spillman Jr., W., 2011. Fiber Optic Sensors: An Introduction for Engineers and Scientists. 2nd ed. New Jersey: John Wiley & Sons, Inc.
Vorster, T. E. et al., 2006. The use of fibre optic sensors to monitor pipeline response to tunnelling. Atlanta, Georgia, United States, ASCE.
Wagener, F., 1982. Engineering construction on dolomite. Durban: PhD Thesis, University of Natal.
Wagener, F., 1985. Dolomites. The Civil Engineer in South Africa, 27(7), pp. 395-406.
Waltham, A. C. & Fookes, P. G., 2003. Engineering classification of karst ground conditions. Quarterly Journal of Engineering Geology and Hydrogeology, Volume 36, pp. 101-118.
Wang, B., Li, K. & Wei, G., 2008. Test on application of distributed fiber optic sensing technique into soil slope monitoring. Journal of the International Consortium on Landslides, 6(1), pp. 61-68.
Wartman, J., 2006. Geotechnical physical modeling for Education: Learning theory approach. Professional issues in Engineering Education and Practice, 132(4), pp. 288-296.
Willsch, R., Ecke, W. & Bartelt, H., 2002. Optical fiber grating sensor networks and their application in electric power facilities, aerospace and geotechnical engineering. Portland, USA, IEEE.
Yin, J., Zhu, H. & Jin, W., 2007. Development and Application of Two Types of Optical Fiber Sensors for Monitoring Soil Nails During Pull-Out Testing, Hong Kong: The Hong Kong Polytechnic University.
Waltham, T., Bell, F. & Culshaw, M. (2005). “Sinkhole and Subsidence”. Krast and Cavernous Rocks in Engineering and Construction. Praxis Publishing. Germany: Springer, pp. 41-44.
Wang, Y. & Li, X. S. (1998). “Linear Representation of Steady-State line for sand”. Journal of Geotechnical and Geoenvironmental Engineering 124(12).
Wood, D.M. (2005). “Physical Modelling”. Proceedings of the 16th International Conference on Soil Mechanics and Geotechnical Engineering. Open Access. pp. 3639-3643.
Zhang, D., Xu, Q., Bezuijen, A., Zheng, G. & Wang, H. (2017). “Internal deformation monitoring for centrifuge slope model with embedded FBG arrays”. Landslides. 14. pp. 407, Available from: https://doi.org/10.1007/s10346-016-0742-2.
Zheng, Y., Huang, D. & Shi, L., 2018. A new deflection solution and application of a fiber Bragg grating-based inclinometer for monitoring internal displacements in slopes. Measurement Science and Technology, 29(5).
Zhu, H. H., Shi, B. & Zhang, J., 2014. Distributed Fiber Optic Monitoring and Stability Analysis of a Model Slope under Surcharge Loading. Journal of Mountain Science, 11(4).
Zhu, H. et al., 2014. Laboratory studies on slope stability monitoring using distribute fiber-optic sensing technologies. Landslide Science for a Safer Environment, Volume 2, pp. 625-629.
Zhu, H.-H.et al., 2014. Fiber Bragg grating-based performance monitoring of a slope model subjected to seepage. Smart Materials and Structures, 23(September), pp. 1-12.

CHAPTER 4: GUIDELINE FOR THE DEVELOPMENT OF WEB REPRESENTATION AND DATA VISUALIZATION PLATFORM.

The current chapter describes a proposal of a WEG-GIS server application and a Smart phone Application for effective sinkhole hazard and risk assessment.

WEG-GIS server application

4.1 Introduction

In this section of the document a brief introduction to the possible approach and the associated guidelines to make available to the citizens the information related to the potential occurrence of sinkholes in urban areas in a dynamic way is provided. The proposed approach is based on the WebGIS technology.

A WebGIS is technology that is used to display and analyze spatial data on the Internet. It combines the advantages of both the Internet and GIS allowing public authorities or private companies to provide access to spatial information to their users without owning expensive GIS software. It is a type of distributed information system, comprising at least a server and a client, where the server is a GIS server and the client is a web browser, desktop application or mobile application. The server has a URL so that clients can find it on the web, while the client relies on HTTP specifications to send requests to the server. The server performs the requested GIS operations and sends responses to the client via HTTP. The format of the response sent to the client can be in many formats, such as HTML, binary image, XML (Extensible Markup Language), or JSON (JavaScript Object Notation).

There are 5 essential elements in every web GIS app, including the following:

- a web application;
- digital basemaps;
- operational layers;
- tasks and tools;
- one or more geodatabase.

Web-GIS allow to add and remove geographic layers of data, but also to collect, process, analyze, interpret, visualize and communicate them, achieving client-server interaction.

Typically, WebGIS refer to the Open Geospatial Consortium (OGC) standards. The OGC is an international not for profit organization committed to making quality open standards for the global geospatial community. These standards are made through a consensus process and are freely available for anyone to use to improve sharing of the world's geospatial data. More details about the OGC standards can be found at the following address https://www.ogc.org/

WebGIS represents the state of the art for what concerns the distribution and visualization of geographical information related to natural hazards. The technology is typically used for planning, response and mitigation of the impact of disaster scenarios at the local, regional or national levels. The advantage of the WebGIS lies in the ability to assimilate different layers of geographic data and correlate them with each other.

WebGIS systems provide the appropriate platform for recording and management of data related to natural disasters and consequently the impact of disaster events on urban environment as well as the environment and infrastructure. For these reasons, WebGIS are used

worldwide for earthquakes (Savvaidis et al., 2005), floods, landslides (Aye et al., 2016) and other geohazards.

The introduction of WebGIS systems as a support to the assessment and management of the risk associated with the occurrence of sinkholes in urban areas brings several benefits to various stakeholders local authorities. In particular, the most relevant benefits associated with the use of WebGIS can be summarized as follows:

- Facilitate the communication to the population for the risk conditions related to the occurrence of sinkholes. Communication is the main responsibility of the local authorities from a civil protection perspective.
- Increased awareness of the risk conditions thanks to the improved communication.
- Creation of a digital dashboard for the combination of all the geographical layers and monitoring data developed in the years able to facilitate the cross-correlation of the available information to get a better understanding of the risk conditions.

4.2 Structure and Architecture

In this section the description of the structure and architecture of the proposed WebGIS system is described. A single interoperating system to be installed on a machine equipped with the LINUX/UBUNTU operating system is recommended in order to have an effective Web-GIS based on open-source software. Several servers must be installed on the machine in order to provide all the necessary services for the information system. The installed server programs are responsible for providing services to clients of various kinds. In the following paragraphs the server programs installed on the machine with their main characteristics are described.

The general sketch representing the Web-GIS platform architecture is represented below.

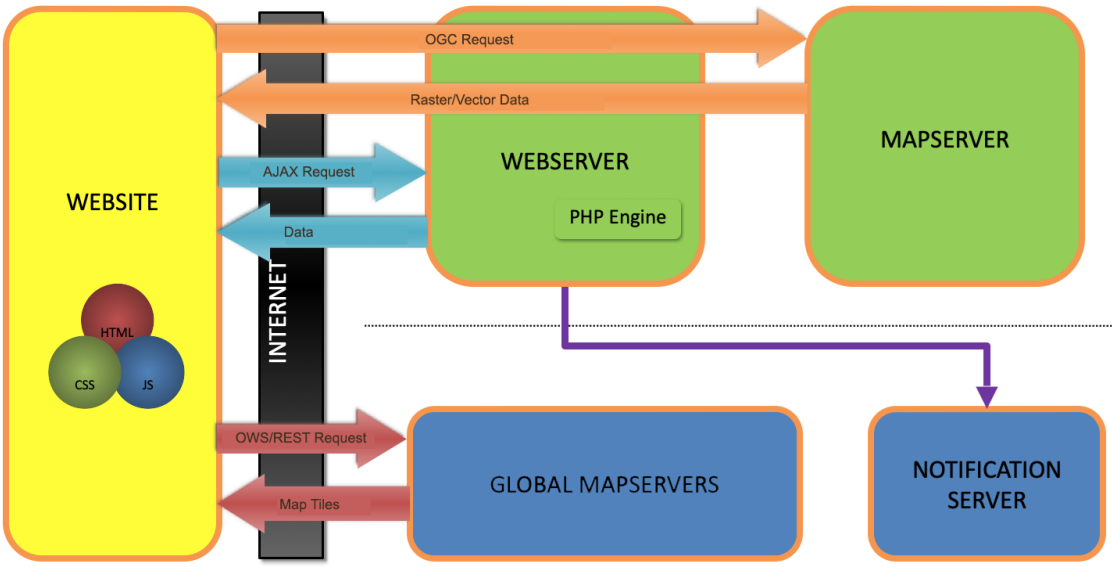

Figure 4-1: Sketch representing the Web-GIS platform architecture

a. Apache HTTP Server

An Apache HTTP Server is a free Web Server developed by the Apache Software Foundation. It is the most popular modular Web Server platform, capable of operating on a wide variety of operating systems. It takes care of managing requests for transferring a client's web pages, typically a web browser. The communication between server and client takes place via the HTTP protocol, which uses the standard TCP 80 port in the system configuration.

In the proposed system architecture, Apache HTTP Server takes care of all the Web calls to a specific IP address, to which it responds, and takes care of serving the WebGIS application to the client, as well as of redirecting client calls to the remaining servers, through developed proxies.

A PHP language interpreter must be also installed to support the back end of the Web Server. The task of a Web server is to receive HTTP requests and provide the client (the browser) with the content of the requested files. However, in the case of files with the .php extension, before granting the request, the Web Server parses and executes the PHP code contained in the file. This allows to manage all back-end operations on the server before exchanging information with the client.

All the operations that need back end control (e.g. security checks, masking, etc.) are recommended to be developed using PHP scripts.

b. Apache Tomcat Server

Apache Tomcat Server is a web server source developed by the Apache Software Foundation and is written entirely in Java, so it can be run on any architecture on which a Java Virtual Machine (JVM) is installed. Its use is necessary because it is a servlet container. In the context of Web programming, servlets are objects written in Java language that operate within a web server or an application server allowing the creation of a web application. In the system architecture this is fundamental for the functioning of Geoserver.

In fact, the standard Apache Tomcat distribution also includes traditional web server functionality, a role that in the system architecture is covered by the Apache HTTP Server previously described, so it is a redundant web server. In any case, any communication between server and client via the http protocol would, in the system configuration, take place on the standard TCP 8080 port. Apache Tomcat Server answers and manages calls to a specific IP address.

c. PostegreSQL Server

PostgreSQL is a complete object-oriented Database Management System (DBMS) released with free license. In PostgreSQL, all objects (with the exception of roles and tablespaces) are located in a schema. It acts as a namespace, allowing objects with the same name to coexist in the same database. All data relating to the project have been put in the "grasberg" schema.

PostgreSQL has been also integrated with its PostGIS extension to manage geospatial data. PostGIS is a spatial extension for PostgreSQL database distributed under the GPL license. It provides the data types specified in the Open Geospatial Consortium standards. It is a geoDataBase and provides the data management system on which a GIS (Geographic Information System) is based.

In the system architecture, PostgreSQL service responds on TCP/IP port 5432 of the host on a specific IP address. Every geographical data is managed by PostgreSQL/PostGIS and distributed by Geoserver.

d. GeoServer

The online distribution of the data contained in the database is performed through the free software Geoserver. GeoServer is an open source Map Server written in Java that allows to share, process and modify geospatial data. Designed for interoperability, it publishes data from any major spatial data source using open standards. Just as Apache HTTP Server guarantees a free and open web server for publishing HTML data, GeoServer aims to do the same for geospatial data. Given the architecture designed, Geoserver must be installed as a JAVA servlet inside Apache Tomcat Server.

GeoServer is the reference implementation of the Open Geospatial Consortium (OGC) standards. List, not exhaustive, of the numerous OGC standards supported by Geoserver:

- Web Map Service (WMS)
- Web Map Tile Service (WMTS)
- Web Feature Service (WFS)
- Web Coverage Service (WCS)
- Style Layer Descriptor (SLD)
- Geography Markup Language (GML)
- KML Encoding Standard (KML)

Within Geoserver, data are hierarchized through workspaces, stores and layers. Like a namespace, a workspace is a container that organizes other elements. In order to be able to use identical layer names, each layer is also identified by the workspace to which it belongs. All data of the system are distributed with a dedicated workspace.

e. Other servers

To operate the system, external servers are also used for dedicated functions.

- **Notification Server**: the system may use Firebase Cloud Messaging (FCM) to send notification messages that are received and displayed in the dedicated app. FCM is a cross-platform messaging solution that lets you reliably send messages to remote applications.
- **Global Map Servers**: to provide background images in map interfaces, the system can use several global Web Mapping services. Backgrounds distributed by the following services are currently available:
- Bing Maps is a web mapping service provided as a part of Microsoft's Bing suite of search engines and powered by the Bing Maps for Enterprise framework.
- OpenStreetMap (OSM) is a collaborative project to create a free editable map of the world. Registered users can freely add additional information to the map.
- **Acquisition Server:** monitoring data can be uploaded in the system through an FTP connection. Every X minutes the EWS algorithm (see specific documentation) processes monitoring data and populates appropriate tables of the DBMS. The system uses these tables to show the alert status in the interfaces.

f. Layers of information

Once the WebGIS is available it to be populated with geographic layers and monitoring data. The type of data to be visualized over the WebGIS are raster (e.g. geotiff, grid, tin, etc.) or vectorial files, including polygons, linear features and point features.

All these data can be selected by the user and visualized over the WebGIS by using as background images the images available in the map interface. From Figure 4-2.2 to Figure 4-6 different examples of a WebGIS developed by Geoapp for a project related to sinkholes in an urban area are shown.

Polygon features

1. Lithology
2. Blanket layer thickness
3. Aquifer Unit
4. Compartments

Linear features

1. Dolerite Dykes
2. Faults

Point features

1. Sinkhole inventory (date, figure, ….,), (id, x,y, elevation) – historical subsidence, or sinkhole events)
2. Borehole data (core, precursor core data, advancement rate), (id, x, y, elevation, depth, lithological unit, groundwater level data).
3. Wells (piezometric level, chemical or isotope composition) – items (id, x, y, elevation, depth, lithological unit, groundwater level data).

Monitoring data

Satellite InSAR data
Fiber Brag grating measurements
Leveling data
Geophysical data – gravimetric data
Microseismic data

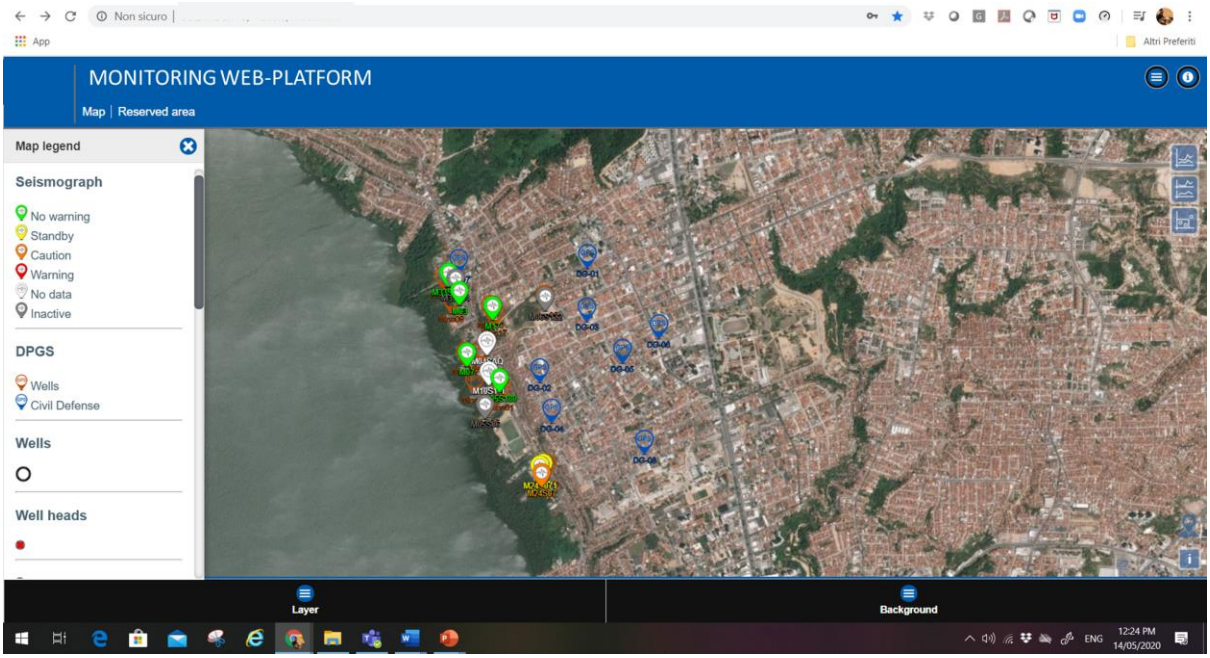

Figure 4-2: Example of WebGIS of an area prone to sinkholes showing the different available layers including monitoring data (on the left Map legend)

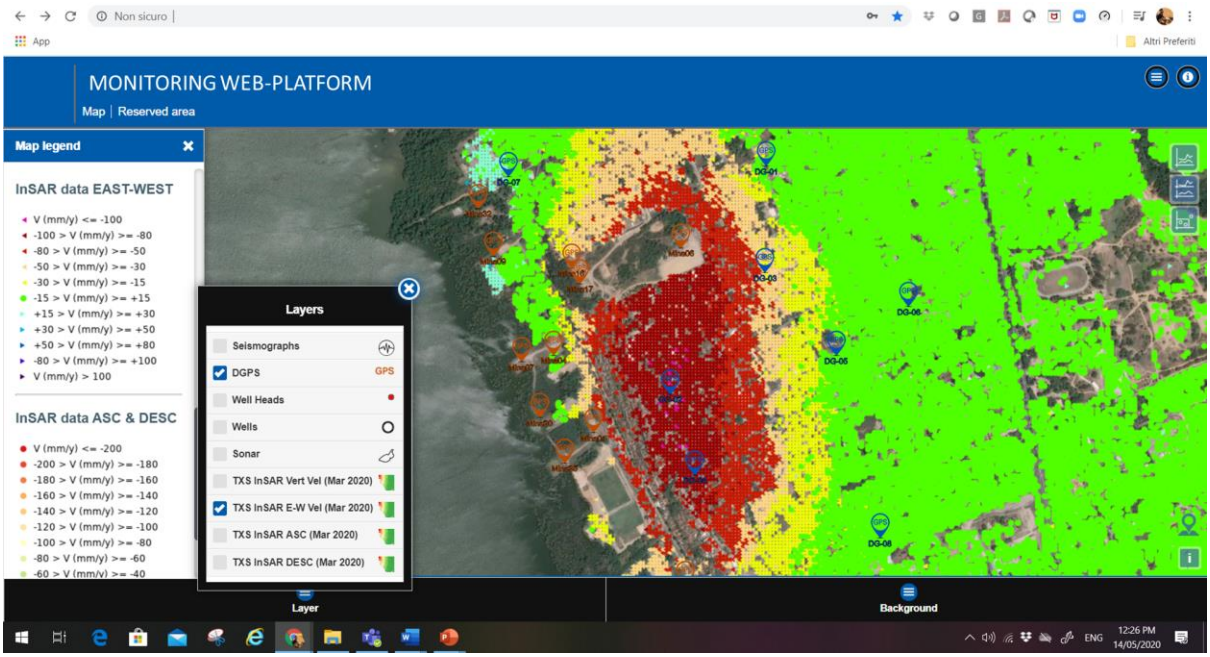

Figure 4-3: Example of WebGIS of an area prone to sinkholes showing the different available layers including GPS and InSAR data

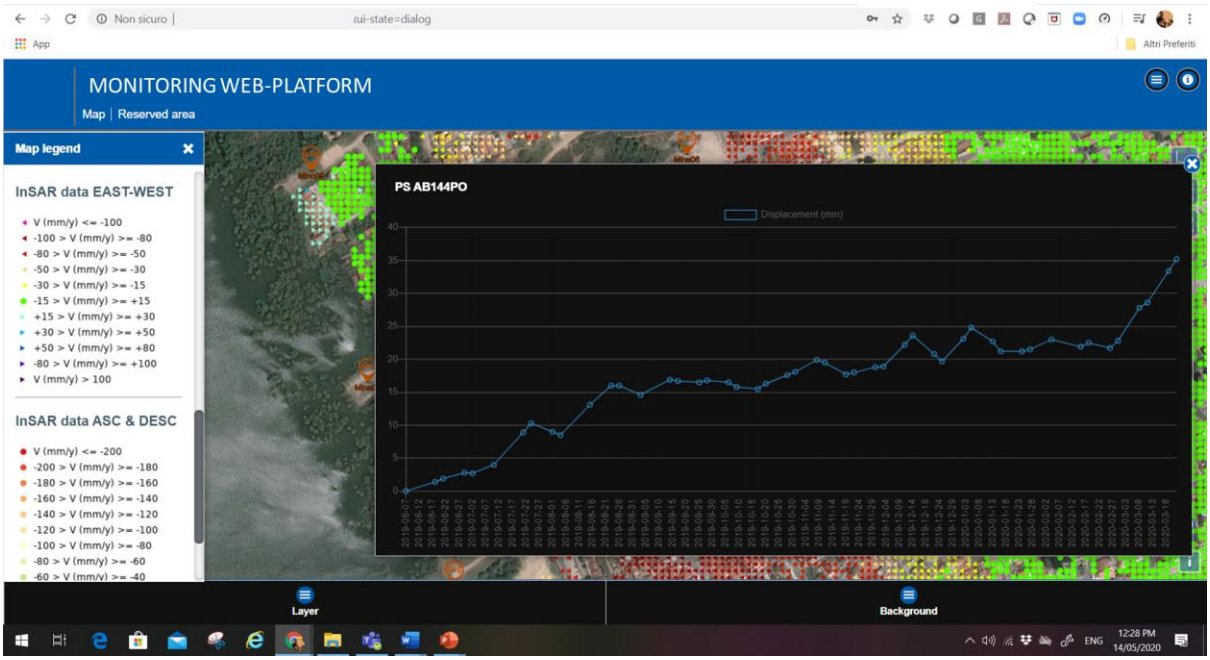

Figure 4-4: Example of WebGIS of an area prone to sinkholes showing time series of displacement from InSAR

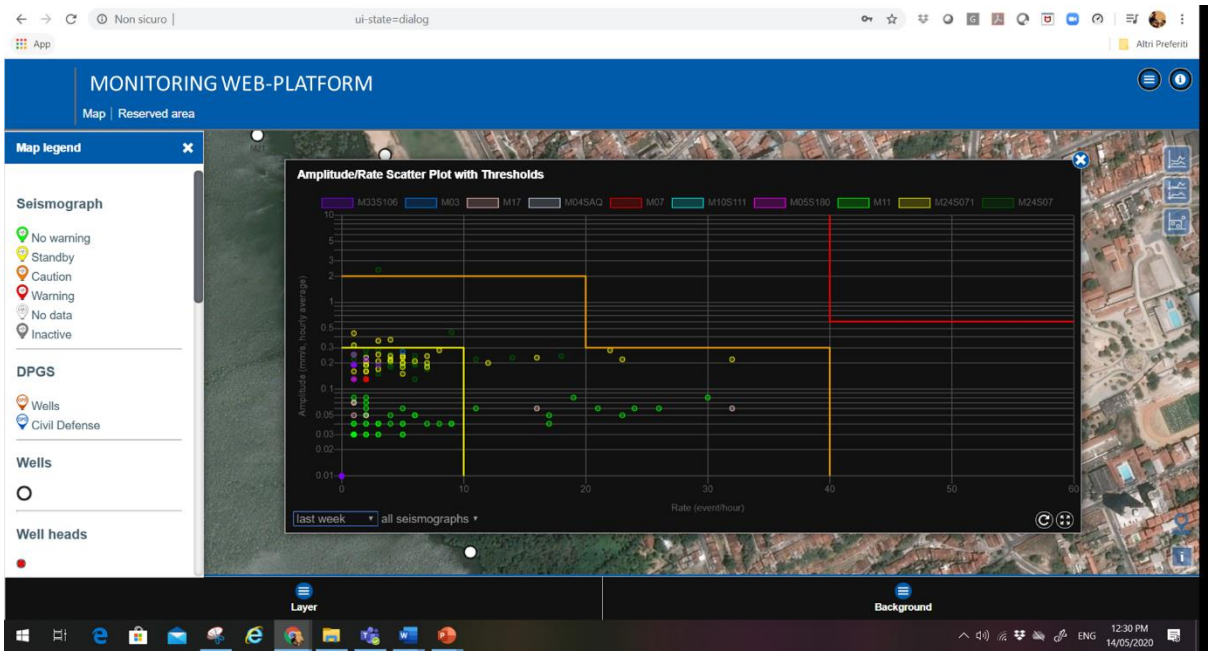

Figure 4-5: Example of WebGIS of an area prone to sinkholes showing a scatterplot based on micro-seismic data used for the Early Warning System

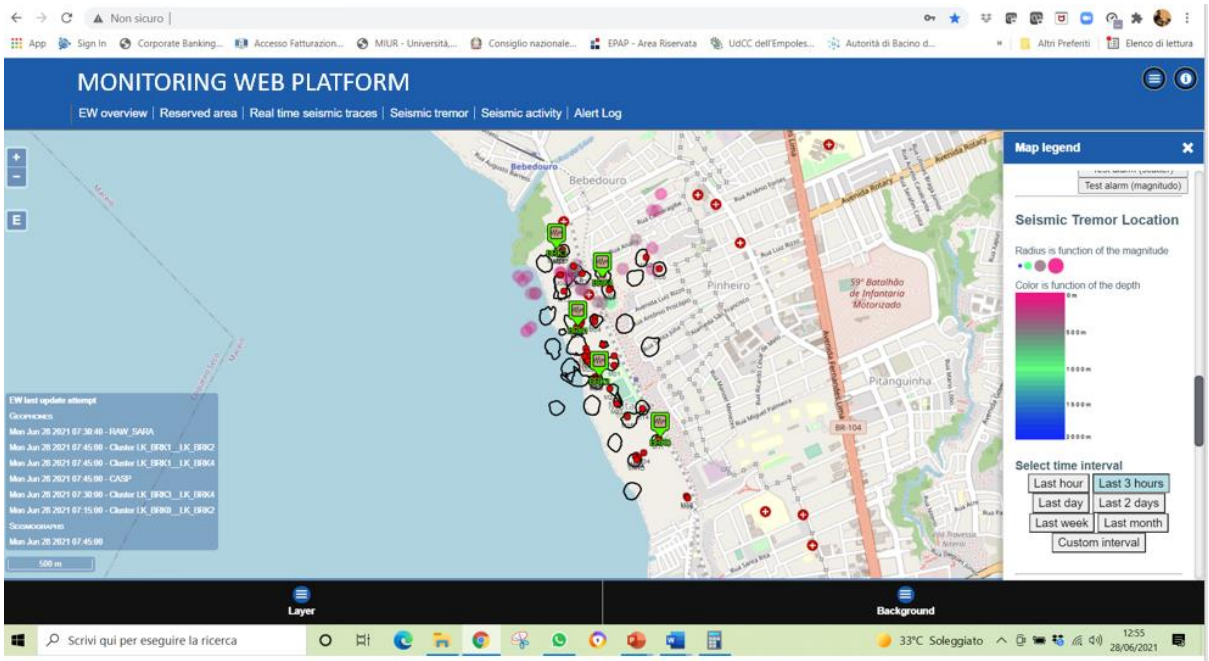

Figure 4-6: Example of WebGIS of an area prone to sinkholes showing the location of caverns responsible for the sinkholes, the location of wells, the microseismic network and the micro-seismic events detected by the network

4.3 Smart phone-based presentation system

The app provides a more practical and faster tool to access and view system data. This section of the report briefly describes the system architecture and the main functionalities of the “App" aimed at visualizing the data available of the web platform also on mobile devices

and in addition to make possible to notify alerts and communications related to risk of sinkholes via app push notifications.

The app in fact is aimed at notifying people working or living in urban area the risk conditions associated with the potential occurrence of sinkholes or informing about areas where sinkholes occurred in the recent past.

The main functionalities of the app are as follow:

- visualize all the geographical layers related to sinkhole hazard and risk assessment available on the web platform over mobile devices.
- visualize the monitoring data collected by the different monitoring systems related to sinkholes.
- automatically notify the alerts in case of high risk for sinkholes.
- notify any message of interest to the user related to sinkholes risk management.
- communicate the actions and the expected behaviors for each alert level of the potential occurrence of sinkholes.

Below a sketch of the conceptual model representing the different elements composing the system architecture is represented.

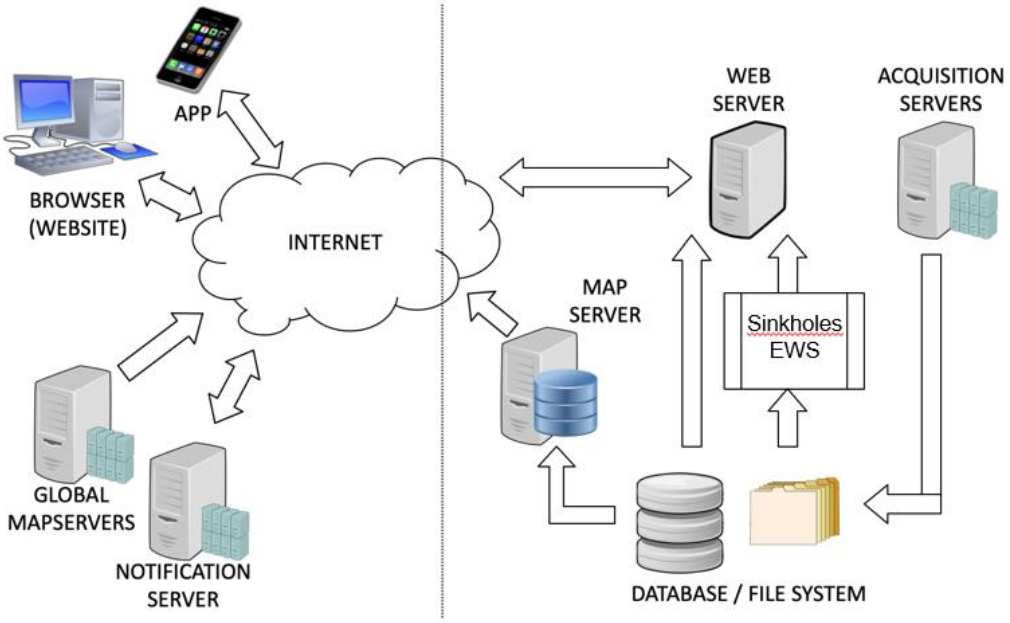

Figure 4-7: Conceptual model of the system architecture

The app is based on n.5 main sections:

- Homepage
- Setup page
- Maps page
- Notifications page
- What to do page

At the opening the app, the Homepage shows a list of buttons. Each button is a shortcut to the same sections of the app. In particular, the buttons of the upper part are shortcut to the map section with specific pre-set configurations.

The button at the top right shows a panel containing global system information. The other button, on top left, open the navigation panel.

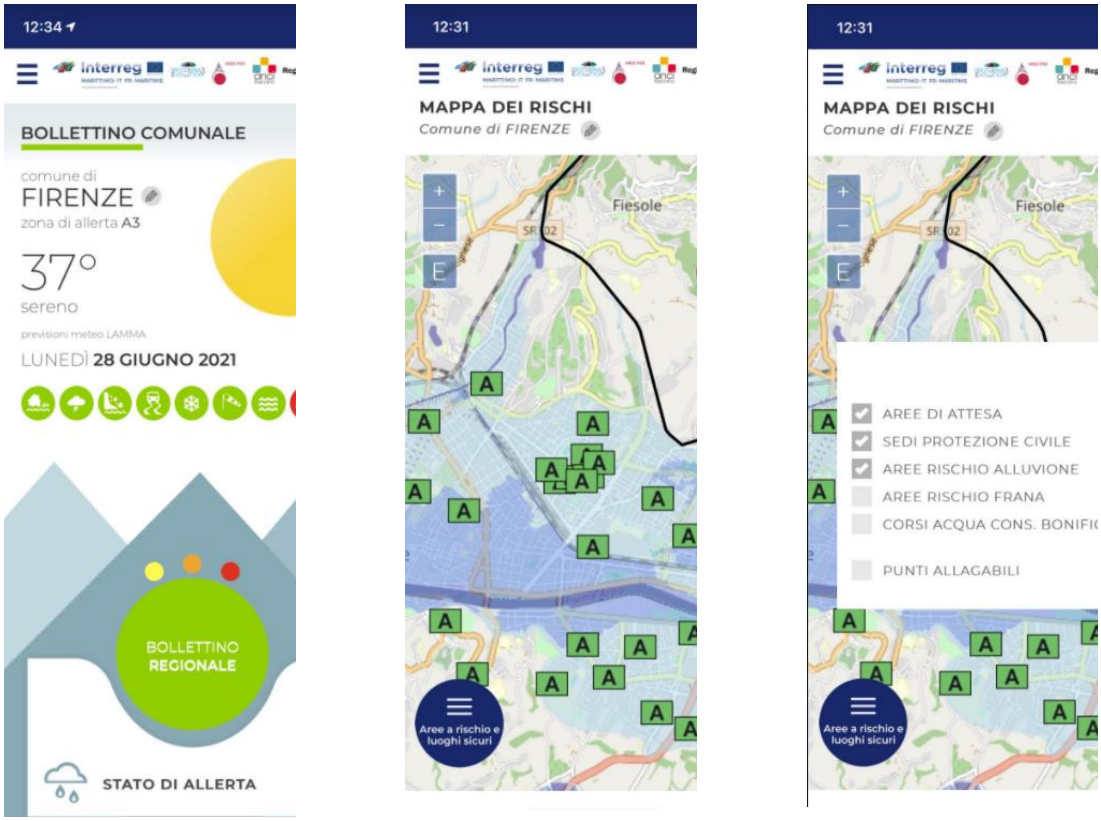

Figure 4-8: Examples of screenshots from an app based on the same architecture of what is proposed in the document

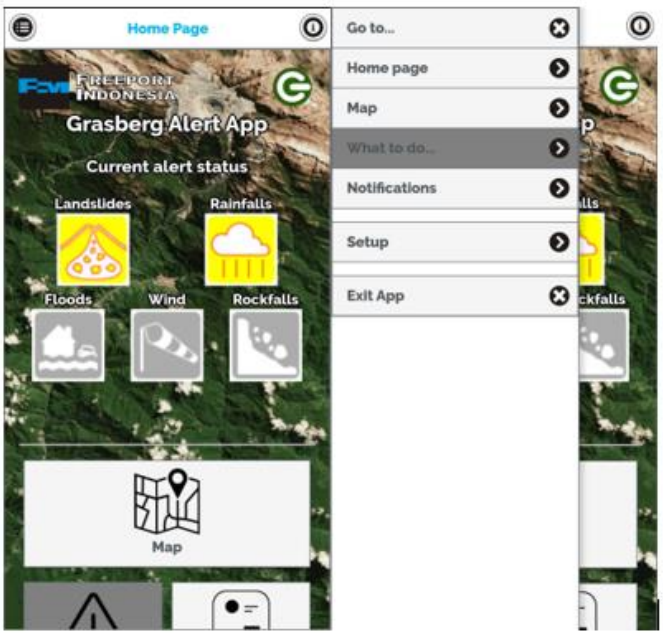

Figure 4-9: Examples of screenshots of the homepage from an app based on the same architecture of what is proposed in the document.

The Setup section allows to select which type of notification to receive and shows the technical information about the app itself.

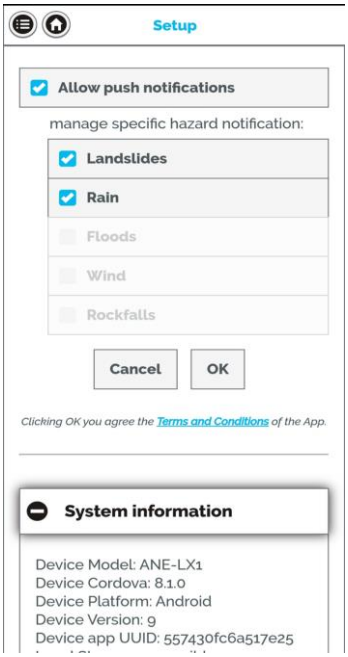

Figure 4-10: Examples of screenshots of the Set-up page from an app based on the same architecture of what is proposed in the document

The Map section is similar to the Map Area of the web platform (see it for more details), but developed for optimal use on mobile devices. The button on the upper right corner open the panel with all information about the layer that can be displayed (legend and so on).

In the same way as per the web platform, the buttons in the footer allow to activate or deactivate the various layers and choose which background to use.

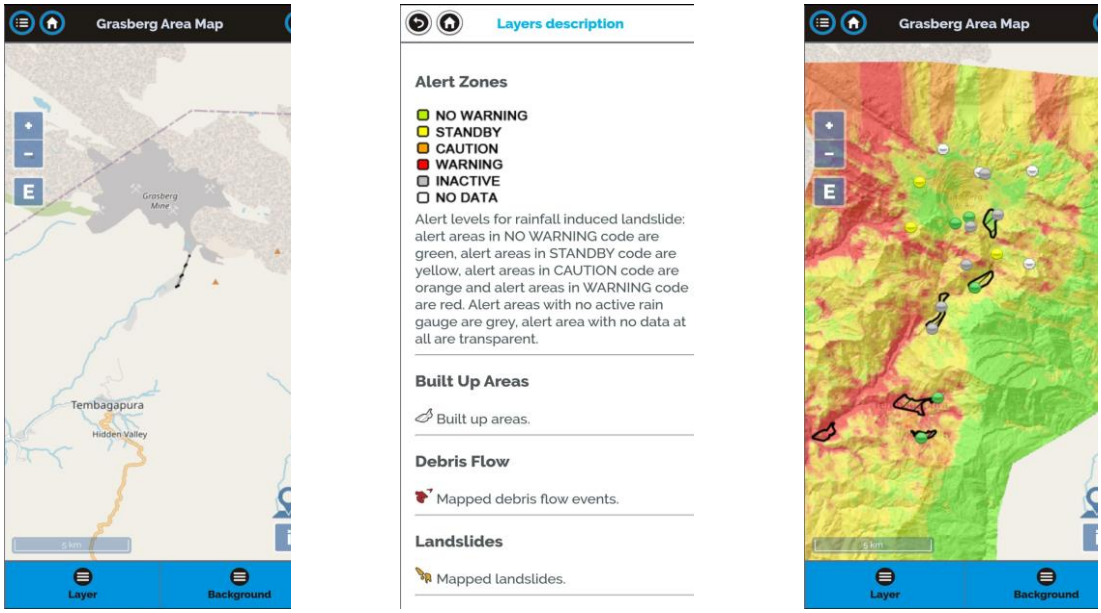

Figure 4-11: examples of screenshots of the Maps page from an app based on the same architecture of what is proposed in the document

The Notifications section is aimed at showing all the notifications currently active in the system (alert notifications and notifications sent via website). For each notification the title, the text, the day of sending and the sender are shown. At the bottom the user can filter the type of notifications. By clicking on the notification, all the relevant information are shown in a popup. It is possible to share them on social networks.

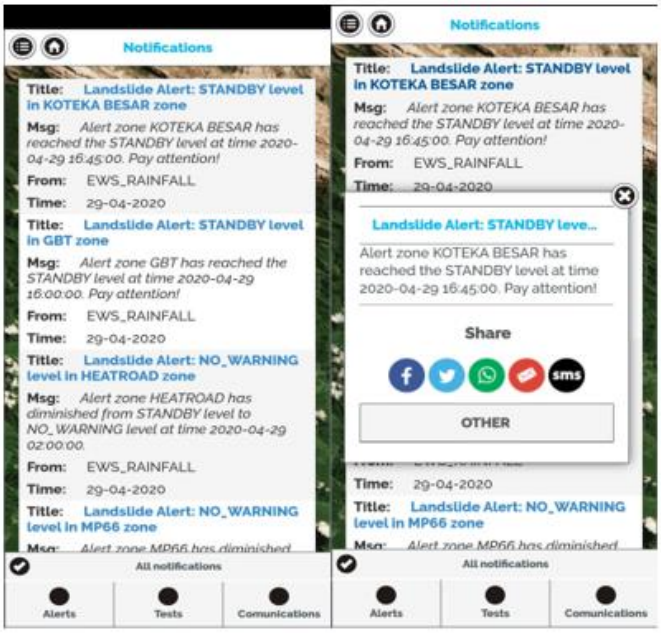

Figure 4-12: example of screenshots of message notifications from an app based on the same architecture of what is proposed in the document

4.4 References

Aye, Z. C., Jaboyedoff, M., Derron, M. H., van Westen, C. J., Hussin, H. Y., Ciurean, R. L., Frigerio, S., and Pasuto, A.: An interactive web-GIS tool for risk analysis: a case study in the Fella River basin, Italy, Nat. Hazards Earth Syst. Sci., 16, 85-101, https://doi.org/10.5194/nhess-16-85-2016, 2016.

Savvaidis P., Sotiriadis A., Valadaki A., Doukas I.D., Tziavos I.N., Kiratzi A., Savvaidis A., Koutoupes S. (2005): Use of Web-based GIS for the evaluation of earthquake damage to the built environment. Presented at the "DPPGIS 2005" Inter. Conference, Pardubice, Czech Republic